

Summer 2014

Ignition mechanism in nanocomposites thermites

Rayon Williams

New Jersey Institute of Technology

Follow this and additional works at: <https://digitalcommons.njit.edu/dissertations>



Part of the [Chemical Engineering Commons](#)

Recommended Citation

Williams, Rayon, "Ignition mechanism in nanocomposites thermites" (2014). *Dissertations*. 179.
<https://digitalcommons.njit.edu/dissertations/179>

This Dissertation is brought to you for free and open access by the Theses and Dissertations at Digital Commons @ NJIT. It has been accepted for inclusion in Dissertations by an authorized administrator of Digital Commons @ NJIT. For more information, please contact digitalcommons@njit.edu.

Copyright Warning & Restrictions

The copyright law of the United States (Title 17, United States Code) governs the making of photocopies or other reproductions of copyrighted material.

Under certain conditions specified in the law, libraries and archives are authorized to furnish a photocopy or other reproduction. One of these specified conditions is that the photocopy or reproduction is not to be “used for any purpose other than private study, scholarship, or research.” If a user makes a request for, or later uses, a photocopy or reproduction for purposes in excess of “fair use” that user may be liable for copyright infringement,

This institution reserves the right to refuse to accept a copying order if, in its judgment, fulfillment of the order would involve violation of copyright law.

Please Note: The author retains the copyright while the New Jersey Institute of Technology reserves the right to distribute this thesis or dissertation

Printing note: If you do not wish to print this page, then select “Pages from: first page # to: last page #” on the print dialog screen

The Van Houten library has removed some of the personal information and all signatures from the approval page and biographical sketches of theses and dissertations in order to protect the identity of NJIT graduates and faculty.

ABSTRACT

IGNITION MECHANISM IN NANOCOMPOSITES THERMITES

**by
Rayon Williams**

Nanocomposite thermites (n-thermites) have been actively investigated for a wide range of potential applications including propellants, explosives, and pyrotechnics. There have been several recent efforts aimed at understanding ignition mechanisms of nanocomposite reactive materials. Although significant progress has been made, ignition mechanisms remain elusive. At the same time, a robust ignition model is required to incorporate these materials in practical energetic formulations. A challenge of this effort is to describe the mechanisms of ignition of n-thermites prepared by Arrested Reactive Milling (ARM) with different stimuli, including heat, spark and impact and also develop a multi-step kinetic model describing different processes affecting ignition. The role of thermally initiated heterogeneous exothermic reactions is evaluated and the effect of decomposition of oxidizer and respective oxygen gas release on ignition is described.

N-thermite powders are prepared by ARM and evaluated using thermal analysis, electron microscopy and other analytical techniques. Experimental studies of ignition of n-thermites stimulated by heating, electric spark and impact are conducted with the goal of developing a reaction model capable of describing different experimental data sets. State of the art thermo-analytical equipment and advanced isoconversion methods are used to describe stability and redox reaction mechanisms in the prepared samples. Multiple reaction steps are identified and described quantitatively.

Thin layers of the prepared powders coated onto an electrically heated Ni-Cr filament are ignited at heating rates between 200-17000 K/s in a miniature vacuum chamber. Ignition is monitored based on both photodiode and pressure transducer signals recorded simultaneously. For spark-induced ignition, powder layers of different thickness are placed in a grounded brass holder. A needle-like electrode is placed above the powder and sparks with different energies are produced. Real time measurements of current and optical signatures produced by the ignited sample at different wavelengths are taken. The results are processed to determine the spark energy, minimum ignition energy, ignition delay, and other parameters. Shock ignition of nanocomposite $8\text{Al}\cdot\text{MoO}_3$ thermite particles are independently carried out at the University of Illinois Urbana Champaign. An individual particle is targeted by a miniature, laser-driven flyer plate accelerated to a speed in the range of 0.5-2 km/s. Ignition delays observed in both shock and spark ignition experiments for the same material are close to each other and vary in the range of 120 – 200 ns.

A reaction mechanism including multiple oxidation steps starting with the Cabrera-Mott (CM) reaction followed by direct oxidative growth of and phase changes in different alumina polymorphs is validated for a stoichiometric $2\text{Al}\cdot 3\text{CuO}$ nanocomposite powder prepared by ARM. The reaction kinetics describing these reaction steps are shown to remain credible for the ARM-prepared reactive composites with different scales of mixing, interface morphologies, and component ratios, as long as the components remained Al and CuO. This work presents a further validation and development of this multistep model to describe reaction in another ARM-prepared thermite system, $8\text{Al}\cdot\text{MoO}_3$.

**IGNITION MECHANISM IN NANOCOMPOSITES
THERMITES**

**by
Rayon Williams**

**A Dissertation
Submitted to the Faculty of
New Jersey Institute of Technology
in Partial Fulfillment of the Requirements for the Degree of
Doctor of Philosophy in Chemical Engineering**

**Otto H. York Department of
Chemical, Biological and Pharmaceutical Engineering**

August 2014

Copyright © 2014 by Rayon Williams

ALL RIGHTS RESERVED

APPROVAL PAGE

**IGNITION MECHANISM IN NANOCOMPOSITES
THERMITES**

Rayon Williams

Dr. Edward Dreizin, Thesis Advisor Date
Professor of Chemical, Biological and Pharmaceutical Engineering, NJIT

Dr. Norman Loney, Committee Member Date
Professor and Chair of Chemical, Biological and Pharmaceutical Engineering,
NJIT

Dr. Jason Jouet, Committee Member Date
Branch Manager/Program Manager at Naval Surface Warfare Center,
Indian Head Division, MD

Dr. Xianqin Wang, Committee Member Date
Professor of Chemical, Biological and Pharmaceutical Engineering, NJIT

Dr. Robert B. Barat, Committee Member Date
Professor of Chemical, Biological and Pharmaceutical Engineering, NJIT

BIOGRAPHICAL SKETCH

Author: Rayon Williams
Degree: Doctor of Philosophy
Date: August 2014

Undergraduate and Graduate Education:

- Doctor of Philosophy in Chemical Engineering, New Jersey Institute of Technology, Newark, NJ, 2014
- Master of Science in Chemical Engineering, New Jersey Institute of Technology, Newark, NJ, 2011
- Bachelor of Science in Chemical Engineering, University of Technology, Jamaica, 2006

Major: Chemical Engineering

Presentations and Publications:

Journal Publications:

Williams, R.A., Schoenitz, M., Ermoline, A., Dreizin, E.L., "Low-temperature Exothermic Reactions in Fully-dense Al/MoO₃ Nanocomposite Powders" *Thermochimica Acta*, submitted, 2014

Shaw, W.L., Dlott, D.D., Williams, R.A., Dreizin E.L., "Ignition of Nanocomposite Thermites by Electric Spark and Shock Wave" *Propellants, Explosives, Pyrotechnics*, vol. 39, pp. 444-453, 2014

Shaw, W.L., Williams, R.A., Dreizin E.L., Dlott, D.D., "Using Laser-driven Flyer Plates to Study the Shock Initiation of Nanoenergetic Materials" *Journal of Physics: Conference Series*, vol. 500, 2014

Williams, R.A., Patel, J.V., Dreizin, E.L., "Ignition of Fully-Dense Nanocomposite Thermite Powder by an Electric Spark" *Journal of Power and Propulsion*, vol. 30, pp. 765-774, 2014

Williams, R.A., Schoenitz, M., Dreizin, E.L., “Validation of the Thermal Oxidation Model for Al.CuO Nanocomposite Powder” *Combustion Science and Technology*, vol. 186, pp. 47-67, 2014

Williams, R.A., Patel, J.V., Schoenitz, M., Ermoline, A., Dreizin, E.L., “Correlation of Optical Emission and Pressure Generated upon Ignition of Fully-Dense Nanocomposite Thermite Powders” *Combustion and Flames*, vol. 160, pp 734-741, 2013

Williams, R.A., Schoenitz, M., Ermoline, A., Dreizin, E.L., “On Gas Release by Thermally-Initiated Fully-Dense 2Al₃CuO Nanocomposite Powder” *International Journal of Energetic Materials and Chemical Propulsion*, vol. 11, pp. 275-292, 2012

Williams, R.A., Beloni, E., Dreizin, E.L., “Ignition of Metal Powder Layers of Different Thickness by Electrostatic Discharge” *Journal of Power and Propulsion*, vol. 28, pp.132-139, 2012

Presentations:

Williams, R.A., Schoenitz, M., Ermoline, A., Dreizin, E.L., “Low-temperature Exothermic Reactions in Fully-dense Al/MoO₃ Nanocomposite Powders”, *Gordon Research Conference on Energetic Materials*, Newry, ME, June 2014

Williams, R.A., Dreizin, E.L., “Ignition Mechanism in Nanocomposite Thermites”, *NSBE Annual Conference Technical Research Exhibit*, Nashville, TN, March 2014

Williams, R.A., Dreizin, E.L., “Ignition of Fully-Dense Nanocomposite Thermite Powders by an Electric Spark”, *AIChE Annual Meeting*, San Francisco, CA, November 2013

Williams, R.A., Dreizin, E.L., “Multistep Reaction Model for Ignition of Nanocomposite Thermites with Different Compositions”, *SHS 2013 International Symposium on Self-Propagating High Temperature Synthesis*, October 2013

Williams, R.A., Schoenitz, M., Dreizin, E.L., “Validation of the Thermal Oxidation Model for Al.CuO Nanocomposite Powder”, *AIChE Annual Meeting*, Pittsburg, PA, October 2012

Williams, R.A., Ermoline, A., Dreizin, E.L., “Ignition of Fully-Dense Nanocomposite Thermite Powders”, *Gordon Research Conference on Energetic Materials*, West Dover, VT, June 2012

Williams, R.A., Schoenitz, M., Ermoline, A., Dreizin, E.L., “On Gas Release by Thermally-Initiated Fully-Dense $2\text{Al}\cdot3\text{CuO}$ Nanocomposite Powder”, *AIAA Region 1-NE Student Conference*, Syracuse, NY, April 2012

Williams, R.A., Ermoline, A., Dreizin, E.L., “Experimental Study of Ignition Mechanisms of Nanocomposite Thermites”, *AICHE Annual Meeting*, Minneapolis, MN, October 2011

I dedicate my PhD thesis to my beautiful wife (Sabrina) and daughter (Rayanna), for all their love and support. Special thanks to my parents, family and good friends for their belief and constant encouragement throughout this journey. Also to my dear family members no longer with us, Dada (Herman Crooks), Aunty (Marilyn Williams) and Boy Blue (Ronald Crooks).

ACKNOWLEDGMENT

I would first like to acknowledge my advisor, Dr. Edward Dreizin because without his guidance and support, this work would not have been possible. I appreciate all the time and valuable input he has provided to me throughout the years. My knowledge and confidence has grown tremendously through his influence as an advisor. His mentorship and trust in me has allowed me to excel academically and grow as an individual. I really appreciate not only being given opportunity to conduct research, but teach undergraduate courses, as well as mentoring several students. He has helped me to be a more rounded person and has given me great exposure through several conferences I was able to attend. Dr. Dreizin is a fantastic researcher and the skill set he has imparted to me will have a lasting influence on my career. It was a pleasure working with him, and I could not have asked for a better advisor.

I also would like to express my gratitude to Dr. Mirko Schoenitz and Dr. Alexandre Ermoline for all their assistance. I appreciate all the individual consultation and guidance they provided to me on countless occasions. I have learnt a great deal from them both, and I feel privileged to have worked with them.

Dr. Norman Loney deserves a special note of thanks for his advice on pursuing my PhD, and his suggestion of working with Dr. Dreizin. I would also like to thank the other members of my thesis committee, Dr. Jason Jouet, Dr. Robert B. Barat and Dr. Xianqin Wang, for their thoughtful criticism and their much appreciate feedback.

I must acknowledge my fellow students and research staff members in Dr. Dreizin group for all their support and assistance. Many thanks to Yasmine Aly, Priya Santhanam, Shashank Vummidi, Hongqi Nie, Amy Corcoran, Ani Abraham, Ian Monk, and my

former colleagues Vern Hoffmann, Demitrios Stamatis, Carlo Badiola, Ervin Beloni, Shasha Zhang, for all their help and advice. Special thanks to students I mentored, Jaymin Patel, James Levin, Xinhang Liu, Nazmul Hussain and Jayamani Vignesh, for helping me conduct experiments, collect and interpret data.

I am grateful to our collaborators, Dr. Dana Dlott and Williams Shaw from University of Illinois Urbana Champaign, for collaborating with us on the shock ignition project.

Finally, I would take this opportunity to express my acknowledgement to our sponsors, Army Research Office (ARO) and Defense Threat Reduction Agency (DTRA), for the financial support.

TABLE OF CONTENTS

Chapter	Page
1 INTRODUCTION.....	1
1.1 Background	1
1.2 Objectives	3
2 PREPARATION CORRELATION OF OPTICAL EMISSION AND PRESSURE GENERATED UPON IGNITION OF FULLY-DENSE NANOCOMPOSITE THERMITE POWDERS.....	5
2.1 Introduction	5
2.2 Experimental	6
2.3 Materials.....	10
2.4 Results.....	12
2.4.1 Pressure and Optical Emission Trace.....	12
2.4.2 Effect of Heating Rate on Ignition Temperature.....	15
2.4.3 Effect of Heating Rate on Pressure Measurements.....	16
2.4.4 Time Delay between the Pressure and Emission Pulses.....	18
2.4 Discussion.....	19
2.4 Conclusions	28
3 ON GAS RELEASE BY THERMALLY-INITIATED FULLY-DENSE $2\text{Al}_3\text{CuO}$ NANOCOMPOSITE POWDER.....	30
3.1 Introduction	30
3.2 Experimental.....	33
3.2.1 Materials.....	33
3.2.2 Filament Ignition.....	35

TABLE OF CONTENTS
(Continued)

Chapter	Page
3.2.3 Thermal Analysis.....	40
3.3 Computation.....	40
3.4 Results.....	42
3.4.1 Thermal Analysis and Ignition.....	42
3.4.2 Partial Reduction of CuO and Ignition.....	49
3.5 Discussion.....	52
3.6 Conclusions.....	54
4 VALIDATION OF THE THERMAL OXIDATION MODEL FOR Al-CuO NANOCOMPOSITE POWDER.....	56
4.1 Introduction	56
4.2 Experimental Techniques.....	59
4.2.1 Materials Synthesis.....	59
4.2.2 Materials Characterization.....	60
4.2.3 Reaction Model Summary and Validation Approach.....	60
4.3 Experimental.....	65
4.3.1 Particle Sizes and Morphology.....	65
4.3.2 Phase Identification.....	70
4.3.3 Composition Analysis.....	71
4.3.4 Thermal Analysis.....	77
4.4 Model Validation.....	79
4.5 Conclusions.....	87

TABLE OF CONTENTS
(Continued)

Chapter	Page
5 LOW-TEMPERATURE EXOTHERMIC REACTIONS IN FULLY-DENSE Al/MoO ₃ NANOCOMPOSITE POWDERS.....	88
5.1 Introduction	88
5.2 Experimental.....	89
5.2.1 Materials.....	89
5.2.2 Thermal Analysis	93
5.3 Experimental Results.....	94
5.3.1 Microcalorimetry	94
5.3.2 Differential Scanning Calorimetry and Thermogravimetric Analysis.....	95
5.3.3 Corrected DSC and TAM III Measurements.....	99
5.4 Reaction Model.....	101
5.5 Model Parameters.....	105
5.6 Discussion.....	113
5.7 Conclusions.....	117
6 IGNITION OF FULLY-DENSE NANOCOMPOSITE THERMITE POWDERS BY AN ELECTRIC SPARK.....	119
6.1 Introduction	119
6.2 Experimental.....	123
6.2.1 Materials.....	123
6.2.2 ESD Apparatus and Diagnostics.....	127
6.2.3 Heated Filament Experiment.....	131

TABLE OF CONTENTS
(Continued)

Chapter	Page
6.3 Results.....	132
6.3.1 Minimum Ignition Energy.....	132
6.3.2 Modes of Ignition.....	133
6.3.3 Experiments at Reduced Pressure and in Argon	135
6.3.4 Ignition Delays for 2Al·3CuO in Air.....	138
6.3.5 Ignition Delays for 8Al·MoO ₃ in Air.....	140
6.3.6 Blending Nanocomposite Thermites with Metal Powders.....	141
6.3.7 Heated Filament Ignition Experiments.....	143
6.4 Discussion.....	145
6.4.1 Minimum Ignition Energy.....	145
6.4.2 Modes of Ignition.....	146
6.4.3 Practical Implications.....	149
6.5 Conclusions.....	151
7 IGNITION OF NANOCOMPOSITE THERMITES BY ELECTRIC SPARK AND SHOCK WAVE	154
7.1 Introduction	154
7.2 Materials	156
7.3 Experimental.....	158
7.3.1 Spark Ignition.....	158

TABLE OF CONTENTS
(Continued)

Chapter	Page
7.3.2 Shock Ignition.....	160
7.4 Results.....	165
7.4.1 ESD Ignition of 8Al•MoO ₃ Monolayers.....	165
7.4.2 Shock Ignition of Individual 8Al•MoO ₃ Particles.....	169
7.5 Discussion	173
7.5.1 Heating Times and Burn Rates.....	173
7.5.2 Ignition Delays and Emission Rise Times.....	175
7.5.3 Ignition Temperatures.....	176
7.6 Conclusions	178
8 CONCLUSIONS.....	179
APPENDIX A Al-Bi ₂ O ₃ NANOCOMPOSITES THERMITES PREPARED USING DIFFERENT MILLING TIMES.....	183
APPENDIX B CHARACTERIZATION OF AGED 8Al-MoO ₃ NANOCOMPOSITES THERMITES.....	186
APPENDIX C ADDITIONAL DATA FOR DETERMINATION OF 8Al-MoO ₃ KINETIC MODEL PARAMETERS.....	188
APPENDIX D IGNITION OF THIN LAYERS OF NANOCOMPOSITE THERMITE POWDERS BY AN ELECTRIC SPARK.....	192
REFERENCES	196

LIST OF TABLES

Table	Page
2.1 Starting Materials Used for Preparation of Nanocomposite Thermites.....	11
2.2 Milling Conditions Used for Preparation of Nanocomposite Thermites.....	11
4.1 Normalized Compositions of the Areas shown in Figure 4.7 in Atomic %, Determined by Standard-free EDX Analysis.....	73
4.2 Sample Compositions and Numbers of Inclusion per Unit Mass Based on Model	83
5.1 Values of Kinetic Constants or Their Ranges Obtained from Processing TAM III and DSC Measurements	106
5.2 Estimated and Assumed Effective Initial Thickness of the Al ₂ O ₃ Layer for the Samples Used in Isothermal Calorimetry Experiments	108
6.1 MIE Based on ESD for the Nanocomposite Thermites.....	133
A.1 Normalized Compositions of Random Areas in Figure B.1 in Atomic %, Determined by Standard-free EDX Analysis.....	187
C.1 Values of Kinetic Constants or their Ranges Obtained from Processing TAM III and DSC Measurements for an Inclusion Size of 20 nm.....	188
C.2 Values of Kinetic Constants or their Ranges Obtained from Processing TAM III and DSC Measurements for an Inclusion Size of 100 nm.....	188

LIST OF FIGURES

Figure	Page
2.1 (a) Schematic layout of the heated filament ignition apparatus and (b) A close-up image of the Ni-Cr filament coated with $2\text{Al}\cdot 3\text{CuO}$ powder.....	9
2.2 High speed camera images of ignited $2\text{Al}\cdot 3\text{CuO}$ coating on a heated Nickel-Chromium filament.....	9
2.3 SEM images showing the powder morphologies for materials studied in this work.....	12
2.4 Photodiode signal and pressure traces recorded at a low pre-set heating rate for different materials.....	14
2.5 Photodiode signal and pressure traces recorded at a high pre-set heating rate for different materials.....	15
2.6 Ignition temperature as a function of the heating rate.....	16
2.7 Maximum pressure as a function of heating rate.....	18
2.8 Average rate of pressure rise as a function of heating rate.....	18
2.9 Time delay between onsets of the photodiode and pressure pulses as a function of the heating rate.....	19
3.1 Configurations of CuO core, Al matrix, and Al_2O_3 shells for different reaction progress.....	31
3.2 SEM images showing the powder morphologies of the powders used in this work. Left and right images show $2\text{Al}\cdot 3\text{CuO}$ and $2\text{Cu}\cdot 3\text{CuO}$, respectively.....	34
3.3 Particle size distributions of the nanocomposite $2\text{Al}\cdot 3\text{CuO}$ powder used in this work.....	35
3.4 Schematic layout of the heated filament ignition apparatus.....	36
3.5 (a) SEM image of the nickel-chromium wire coated with nanocomposite $2\text{Al}\cdot 3\text{CuO}$ powders, (b) High speed camera image of freshly coated wire and (c) High speed camera image of the ignited coating.....	38

LIST OF FIGURES
(Continued)

Figure	Page
3.6 Photodiode and pressure signal for an ignited $2\text{Al}\cdot 3\text{CuO}$ sample.....	39
3.7 Effect of heating rates on the shift between onsets of pressure and emission pulses.....	42
3.8 Experimental and computed DSC curves for the nanocomposite $2\text{Al}\cdot 3\text{CuO}$ powder.....	45
3.9 Computed heat flow curves under thermal analysis conditions (no heat transfer effects), and under filament ignition conditions (accounting for heat transfer to and from the powder coating).....	46
3.10 Summary of experimental DSC features, filament ignition temperatures, and corresponding computational results (200-nm CuO inclusions).....	48
3.11 Effect of heating rate on the experimental ignition temperature and reference points predicted in calculations. Constant oxygen consumption curves and the trend showing occurrence of a sharp heat flow spike caused by the polymorphic phase change in alumina are calculated for 200-nm CuO inclusions.....	51
4.1 Schematic diagram of the composite material described in the reaction model....	62
4.2 Backscattered electron SEM images of cross-sectioned and embedded in epoxy nanocomposite powders with the nominal composition of $2\text{Al}\cdot 3\text{CuO}$ prepared using different milling times: 1(A, B): 30min; 2(A, B): 40min; 3(A, B): 60min; 4(A, B): 80min.....	67
4.3 SEM images showing (a) cross-sectioned sample and (b) thresholded image with white areas indicating CuO inclusions used for the inclusion size analysis...	68
4.4 Size distributions of copper oxide inclusions determined from SEM images of nanocomposite powders with the nominal composition of $2\text{Al}\cdot 3\text{CuO}$ prepared using different milling times.....	69
4.5 Particle size distributions of nanocomposite powders with the nominal composition of $2\text{Al}\cdot 3\text{CuO}$ prepared using different milling times.....	70

LIST OF FIGURES
(Continued)

Figure	Page
4.6 XRD patterns of nanocomposite powders with the nominal composition of 2Al•3CuO prepared using different milling times.....	71
4.7 An example SEM image identifying areas for EDX composition analysis used for calibration of composition with brightness (This sample was prepared using 30-min milling time).....	73
4.8 Calibration of composition with brightness for nanocomposite powders with the nominal composition of 2Al•3CuO prepared using different milling times.....	74
4.9 SEM images showing (a) cross-sectioned sample and (b) thresholded image with light areas indicating whole particles used in average composition analysis.	76
4.10 Average composition for different size fractions of nanocomposite powders with the nominal composition of 2Al•3CuO prepared using different milling times....	76
4.11 Experimental DSC curves for nanocomposite powders with the nominal composition of 2Al•3CuO prepared using different milling times.....	78
4.12 Experimental TAM curves for nanocomposite powders with the nominal composition of 2Al•3CuO prepared using different milling times.....	79
4.13 Experimental and model DSC curves for nanocomposite powders with the nominal composition of 2Al•3CuO prepared using different milling times.....	83
4.14 SEM/EDX analysis supported and model-implied composition changes for nanocomposite powders with the nominal composition of 2Al•3CuO prepared using different milling times.....	84
4.15 Experimental and calculated TAM III curves for the nanocomposite 2Al•3CuO powders prepared with different milling times.....	86
5.1 Backscattered electron SEM images of cross-sectioned 8Al•MoO ₃ nanocomposite powder at low (left) and high (right) magnifications.....	91
5.2 XRD pattern of the prepared 8Al•MoO ₃ nanocomposite powder.....	92
5.3 Isothermal TAM III measurements for nanocomposite 8Al•MoO ₃ powders.....	94

LIST OF FIGURES
(Continued)

Figure	Page
5.4 Scanning TAM III measurements for nanocomposite 8Al·MoO ₃ powders.....	95
5.5 DSC curves for nanocomposite 8Al·MoO ₃ powders.....	96
5.6 Low-temperature DSC, TG and derivative mass loss, dm/dt, traces for nanocomposite 8Al·MoO ₃ powders.....	98
5.7 Correlation of derivative mass loss and DTA peaks with species in the evolved gas.....	99
5.8 Corrected and measured DSC heat flow data accounting for dehydration. a. Correction details. b. Summary for different normalized heating rates.....	100
5.9 Corrected and measured microcalorimetry heat flow data accounting for dehydration.....	101
5.10 Schematic diagram for the core-shell and planar geometries considered in the reaction model.....	103
5.11 Predicted effective thickness of the Al ₂ O ₃ layer as a function of the storage time of the 8Al·MoO ₃ samples at room temperature.....	107
5.12 Heat flows and respective alumina thickness as a function of time for isothermal calorimetry experiments. Solid lines represent measurements; dashed lines are predicted using the identified reaction kinetics.....	109
5.13 Experimental and calculated heat flows from TAM III experiments (left) and DSC (right).....	110
5.14 Inferred from experiments and calculated thicknesses of the Al ₂ O ₃ layer for TAM III experiments (left) and DSC (right).	111
5.15 Experimental and calculated DSC curves for 8Al·MoO ₃ at heating rates of 2, 5, and 10 K/min. For temperatures below 400 K, E ₁ =28 kJ/mol. For temperatures above 400 K, E ₁ =54 kJ/mol.....	113
5.16 Calculated rates of heat production by 22-μm diameter nanocomposite 8Al·MoO ₃ particles placed on a surface heated at different rates.....	117

LIST OF FIGURES
(Continued)

Figure	Page
6.1 Typical SEM images showing the particle shapes and surface morphologies for the prepared nanocomposite powders and powder blends.....	126
6.2 Particle size distributions for the prepared nanocomposite powders.....	127
6.3 Schematic of the experimental set-up.....	131
6.4 Optical emission and spark current traces with the corresponding image showing individual burning particles for a powder monolayer ignited by a 5 kV ESD.....	135
6.5 PMTs and current traces showing ignition delays for cloud ignition of the thermite powders caused by a 5 kV ESD.....	135
6.6 Images of ignited 2Al·3CuO powders milled for 60 min carried out as a monolayer in different environments: I) air, II) vacuum and III) argon.....	137
6.7 Consecutive images of the high speed video showing ignition of a 192- μm thick layer of nanocomposite powder of 2Al·3CuO milled for 30 min in air (images A-C) and vacuum (images D-E).....	138
6.8 Ignition delay as a function of Joule energy in air for 2Al·3CuO samples prepared as coatings with thicknesses of 192 and 500 μm	139
6.9 Ignition delay as a function of Joule energy in air for 8Al·MoO ₃ samples prepared as coatings with thicknesses of 252 and 500 μm . Milling times are 30 and 60 min for the data shown respectively in the left and right side panels.....	140
6.10 Ignition delays in air determined using emission traces recorded at 589 nm as a function of Joule energy for thermite powders prepared by 30-min milling and blended with Al and Ti powders. All powder samples are prepared as 500- μm thick layers.....	142
6.11 Shift between onsets of pressure and emission pulses in vacuum based on heated filament experiment at different heating rates for 2Al·3CuO milled for 60 min and 8Al·MoO ₃ milled for 30 min.....	144
6.12 Comparison of time shift between onsets of pressure and emission pulses for as prepared 2Al·3CuO and 8Al·MoO ₃ nanocomposite powders milled for 60 min and corresponding blends (75:25%wt.) with Al at different heating rates.....	145

LIST OF FIGURES
(Continued)

Figure	Page
7.1 SEM images showing the particle shapes and surface morphology for the prepared 8Al•MoO ₃ nanocomposite powder.....	157
7.2 Particle size distribution for the prepared 8Al•MoO ₃ nanocomposite powder.....	158
7.3 Schematic of the experimental set-up for ESD ignition.....	160
7.4 (a) Schematic of the laser-driven flyer plate system. (b) Image of a thermite target, consisting of many individual particles scattered on an optical window. A thin 0.75 μm layer of cement was used to fix the particles. (c) Microscope image of a 20 μm 8Al•MoO ₃ thermite particle through a 50 μm aperture. (d) Reacted thermite in the center of a crater created by impact with a 700 μm diameter Al flyer plate.....	163
7.5 An ESD spark current trace and a PMT voltage corresponding to the emission of the burning sample recorded in an ignition test with a monolayer of nanocomposite 8Al•MoO ₃ powder. The spark voltage is 8 kV.....	166
7.6 a) A photograph of the burning particle streaks recorded in an ESD ignition test with the spark voltage of 8 kV. b) An SEM image taken with backscattered electrons showing partially burned particles captured on a Cu foil placed 2 mm away from the spark-ignited powder.	166
7.7 Optical emission and spark current traces showing onset differences for 8Al•MoO ₃ powder monolayer ignited at different ESD energies.....	168
7.8 Ignition delay, 90% fast rise time and integrated emission as a function of Joule energy for 8Al•MoO ₃ powder monolayer ignited by spark.....	169
7.9 Characteristic shock induced emission trace and flyer speed as a function of time for a 10-20 μm 8Al•MoO ₃ particle. The impact velocity is 1.34 km/s.....	170
7.10 Emission traces for 8Al•MoO ₃ particles ignited by impacts at different speeds....	171
7.11 Properties of the second emission burst as a function of flyer impact speed. (a) Delay is the time between impact at t = 0 and the 10% point of the second burst rise. (b) Rise time is the time for 10%-90% rise of the emission burst. (c) Integral is proportional to the time-integrated emission burst intensity.....	172

LIST OF FIGURES
(Continued)

Figure	Page
7.12 Estimated temperature to which the volumetric mean particle size is heated by the spark current during the delay time for 8Al•MoO ₃ powder monolayer.....	177
A.1 Photodiode signal and pressure traces recorded at a low pre-set heating rate for 2.35Al-Bi ₂ O ₃ prepared at different milling times.....	183
A.2 Photodiode signal and pressure traces recorded at a high pre-set heating rate for 2.35Al-Bi ₂ O ₃ prepared at different milling times.....	184
A.3 Ignition temperature of 2.35Al-Bi ₂ O ₃ n-thermite powders milled for different times as a function of the heating rate.....	184
A.4 Maximum pressure of 2.35Al-Bi ₂ O ₃ n-thermite powders milled for different times as a function of the heating rate.....	185
A.5 Isothermal TAM III measurements for nanocomposite 2.35Al-Bi ₂ O ₃ n-thermite powders milled for different times.....	185
B.1 SEM image of aged 8Al-MoO ₃ used for EDX composition analysis based on randomly selected areas.....	186
B.2 XRD patterns of aged 8Al-MoO ₃ nanocomposite powder.....	186
B.3 Corrected and measured DSC heat flow data of aged 8Al-MoO ₃ powder accounting for dehydration at different heating rates.....	187
C.1 Root mean squared error of fit as a function of aluminum oxide initial thickness for different inclusion sizes.....	189
C.2 Parametric plots obtained by fitting DSC and TAM experimental curves for different inclusion sizes.....	190
C.3 Relative difference averaged over the highlighted region of Figure C.2 for different 8Al-MoO ₃ inclusion sizes.....	191

LIST OF FIGURES
(Continued)

Figure	Page
D.1 Typical optical emission traces with the corresponding temperature estimates for burning particles of 2.35Al·Bi ₂ O ₃ monolayers ignited by 8 kV and 12kV ESD.....	193
D.2 Typical optical emission traces with the corresponding temperature estimates for burning particles of 2Al·3CuO monolayers ignited by 8 kV and 12kV ESD...	193
D.3 Typical optical emission traces with the corresponding temperature estimates for burning particles of 2Al·Fe ₂ O ₃ monolayers ignited by 8 kV and 12kV ESD...	194
D.4 Typical optical emission traces with the corresponding temperature estimates for burning particles of 2Al·MoO ₃ monolayers ignited by 8 kV and 12kV ESD...	194
D.5 Summary of ignition delays and burn time for all materials at different emission wavelengths and applied voltages.....	195
D.6 Summary of maximum temperature for all materials at different applied voltages based on intensity ratio of 700nm/800nm wavelengths.....	195

CHAPTER 1

INTRODUCTION

1.1 Background

The “Thermit” process was discovered in 1893 and patented in 1895 by German chemist Hans Goldschmidt. Thermites consist of a metal powder, usually aluminum, mixed with a metal oxide, typically Fe_2O_3 or CuO . When ignited, thermites undergo a highly exothermic redox reaction. A tremendous amount of heat is released and one of the products is a molten metal, Fe or Cu, which is exploited in thermite welding [1, 2], used mostly for large components, such as train rails. Specialty heaters utilizing a controlled thermite combustion to heat water or steam pipe coils for domestic heating systems have been developed [3]. The use of thermites for hydrogen production by accelerating water split reaction has been recently explored given the world’s paradigm shift towards green and sustainable forms of energy [4].

Because of the significant heat release, thermites have potential applications in propellants, explosives, and pyrotechnics. However, because they are difficult to ignite and because they burn slowly, uses of traditional thermites in advanced energetics are limited severely. An effort to mitigate these limitations led to the development of nanocomposite thermites (n-thermites). In such materials, components are mixed with each other on the scale of 100 nm or less, resulting in their rapid initiation and fast burn.

Improved ignition and combustion rates combined with high energy densities place n-thermites in a new class of energetic materials [5-7]. Recently, n-thermites have been developed and explored for a wide range of potential applications, where they can replace conventional metal-free energetics [8-12].

In n-thermites, the nano-scale mixing results in a highly developed interface area between reactive components. The initiation characteristics of these materials are strongly influenced by these reactive interfaces and self-sustaining exothermic reactions begin at much lower temperatures compared to conventional thermite powders [5]. Mechanisms of such reactions are poorly understood. Very high burn rates for nano-thermites have been observed, with flame speeds of the order of km/s, three orders of magnitude faster than observed for traditional thermites [13-15], which can, most likely, be attributed to their accelerated ignition.

N-thermites are prepared by several techniques, including mixing of nano-powders [16-18], sol-gel processing [19-21], self-assembly [22-24], vapor layer deposition [25, 26], and arrested reactive milling (ARM) [27-30]. N-thermite powders prepared by ARM have the unique advantage of combining the high energy density of conventional thermites with high reaction rates associated with nano-scale mixing of reactive components, while offering relative simplicity of their handling and processing, typical for conventional micron-sized powders. Each particle is fully dense and made of solid phases mixed on the nano-scale. Previous results suggest that in the

ARM-prepared n-thermites, the components are separated by passivating layers with the thickness of ~ 0.5 nm, much thinner than the natural oxide layers formed on surface of air-passivated aluminum nanopowders [31]. The unique interface morphology is thought to cause the exothermic redox reactions in such materials to begin at lower temperatures compared to other types of nanocomposite thermites [5].

1.2 Objectives

The general objective of this research is to describe the mechanisms of ignition of n-thermites prepared by ARM with different stimuli, including heat and spark. Specific objectives are to establish the role of thermally initiated heterogeneous exothermic reactions and investigate the effect of decomposition of oxidizer and respective oxygen gas release on ignition. It is also desired to develop a multi-step kinetic model describing different processes affecting ignition. The model should be valid for n-thermites ignited using different stimuli, covering a wide range of possible heating rates.

This work includes preparation of n-thermite samples by ARM and characterization of the prepared samples using thermal analysis, electron microscopy and other analytical techniques. Experimental studies of ignition of n-thermites stimulated by heating, shock compression and electric spark were conducted with the goal of developing a reaction model capable of describing different experimental data sets.

ARM uses mechanical milling to prepare n-thermites. In this work, both shaker and planetary mills are used and milling conditions are selected carefully using previous work and the model describing energy dissipation from milling tools to the powder being milled [32-39]. The compositions selected for studies use Al as a fuel and Fe_2O_3 , MoO_3 , CuO , and Bi_2O_3 as oxidizers. State of the art thermo-analytical equipment and advanced isoconversion methods are used to describe stability and redox reaction mechanisms in the prepared samples [31-33, 39-42]. Multiple reaction steps are identified and described quantitatively in Reference [33] for a specific Al-CuO system. In this work, the model initially developed in Reference [33] will be validated and modified as necessary to describe initiation of n-thermites with different compositions, including different Al/CuO ratios as well as replacing CuO with different oxidizers. In addition, the energy transfer from the spark and from the heated filament to the powder will be described in detail; the same chemical model is expected to be capable of describing ignition with these different ignition stimuli. Limitations of the previously developed model will be addressed; in particular the role of oxidizer decomposition and resulting release of gaseous oxygen will be elucidated.

CHAPTER 2
CORRELATION OF OPTICAL EMISSION AND PRESSURE GENERATED
UPON IGNITION OF FULLY-DENSE NANOCOMPOSITE
THERMITE POWDERS

2.1 Introduction

Recently, research on new reactive nanocomposite materials has been active [5, 43]. In particular, fully dense nanocomposite powders are of interest as combining high reaction rates associated with developed reactive interfaces and relative simplicity of handling and mixing such materials, typical for conventional micron-sized powders. Such powders can be made by top-down techniques, such as mechanical milling [27] or cold rolling [44], as well as by modification of bottom-up methods, such as cutting vacuum-deposited nanofoils [26, 45, 46]. Each particle in a nanocomposite powder is made of solid phases mixed on the scale of ca. 100 nm or less. The large interface area between components capable of a highly exothermic chemical reaction assures a high reaction rate, attractive for many applications.

Nanocomposite thermites are composed of metal fuels, usually, aluminum, and metal oxides that are relatively easily reduced. Most previous applications of thermites involved micron-scale or even coarser powder mixtures, e.g., for railroad welding [1, 2]. Respectively, reaction mechanisms developed and used described reactions detected at high temperatures, typically above the aluminum melting point [47]. However, reactions

begin at much lower temperatures in nanocomposite thermites [5]. Existing mathematical models for these reactions are either simplistic or use extrapolation of poorly validated or inappropriate rate expressions. It is essential to develop a model that reflects true physico-chemical processes occurring in nano-materials.

It has been proposed that ignition in nano-thermites is affected by decomposition of the oxidizer resulting in release of gaseous oxygen [48]. Alternatively, it has been discussed that ignition in such materials is controlled by evolution and change in transport properties of the growing Al_2O_3 layer [32]. In this work, the correlation of gas release and ignition is examined for several nanocomposite thermite powders.

Nanocomposite thermite powders were prepared using Arrested Reactive Milling or ARM [27]. ARM creates a powdered material where nano-scale oxide is embedded in a metal matrix [5]. Material comprises fully dense micron-sized composite particles. Several nanocomposite thermites were prepared by ARM and described in detail elsewhere [29, 36, 49-53].

2.2 Experimental

A sketch of the experimental setup is shown in Figure 2.1a. A straightened, 5-cm long, 0.5 mm diameter Ni-Cr wire was placed in a miniature vacuum chamber having an estimated volume of 31 cm^3 . The volume was determined by filling the sealed chamber with water and emptying it into a graduated cylinder. A thin layer of thermite powder was

coated on the wire (see Figure 2.1b). The coating mass was 2.2 ± 0.3 mg, as was found by weighing uncoated and then coated wires prior to loading them into the vacuum chamber. The chamber was evacuated to 2.5-5.0 kPa. The wire was heated electrically, and the powder coating ignited. The current and voltage on the wire were measured in real time and used to calculate its temperature history. The heating was assumed to occur adiabatically and the Ni-Cr wire properties were assumed to remain constant. This approach was previously validated for the present setup by direct measurements of the wire temperature using an infrared pyrometer [54, 55]. Just before the wire was heated, the chamber pressure was consistently set to 5.8 kPa using the static gauge pressure reading.

Ignition was monitored in real time, tracking both optical emission and pressure in the chamber. Ignition is illustrated by the sequence of high-speed video frames shown in Figure 2.2. The video was recorded at 500 frames per second. In the first frame shown, the filament is not sufficiently bright, so its location and the location of the powder coating are schematically shown by white contour lines and grid, respectively. In the subsequent frame, ignition is observed to occur at the edge of the wire coating. The ignition consistently occurred at the coating's edge, where the wire temperature is less affected by the heat capacity of the coating and thus is slightly higher than under the coating's center. The next frame shows that the flame propagated through the entire coating length. Finally, a frame taken more than 300 ms after the coating combusted is

shown, to illustrate when the filament itself became sufficiently bright to be visible in the video. Note that the filament is intact after the powder coating had combusted.

Different heating rates (from 200 to 17,000 K/s) were achieved using a rheostat and several car batteries connected in series. Both static and dynamic pressure transducers were connected to a data acquisition unit. The static pressure transducer (Omegadyne model PX209-30V45G5V, response time 2 ms) gave absolute pressure before and after the experiment. The dynamic transducer (PCB piezoelectric pressure sensor with a model 106B51 microphone, response time $<12 \mu\text{s}$) was used to record rapid changes in pressure while the ignition occurred. It is based on piezoelectric effect and is unable to read the absolute pressure value; however, it is well suited to record rapid changes in the chamber pressure. A photodiode signal was used to characterize optical emission from the igniting material. The photodiode response time is 2ns, however, the response time of the data acquisition board was set to $10 \mu\text{s}$, matching the time resolution of the dynamic pressure transducer.

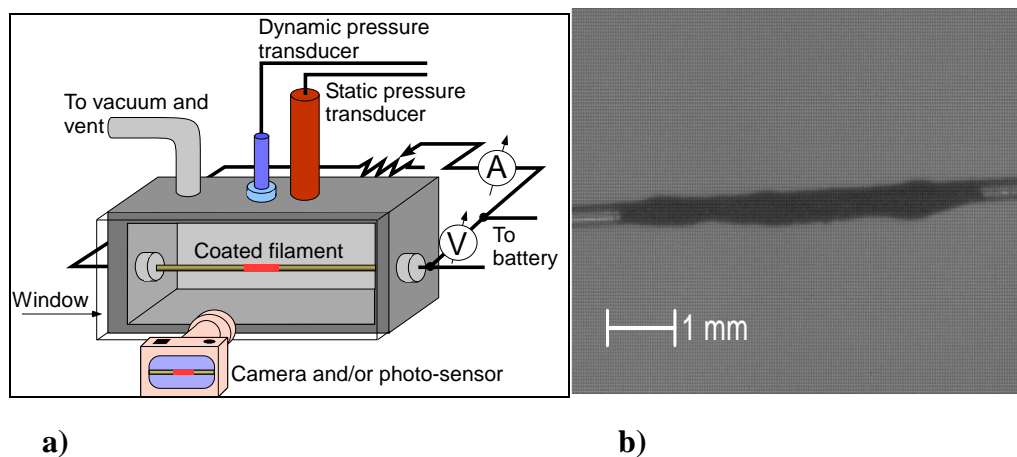


Figure 2.1 (a) Schematic layout of the heated filament ignition apparatus and (b) A close-up image of the Ni-Cr filament coated with $2\text{Al}\cdot 3\text{CuO}$ powder.

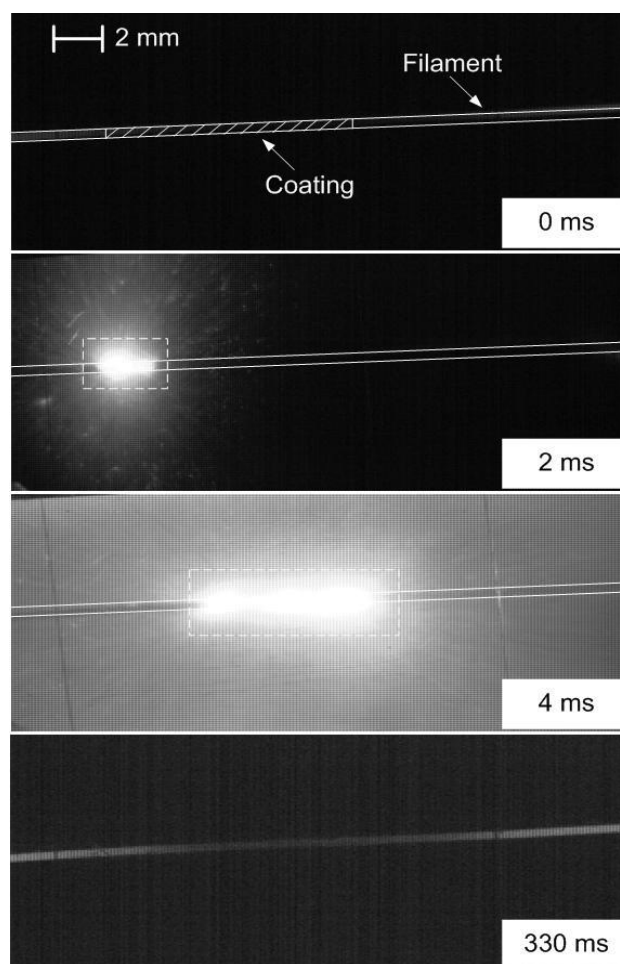


Figure 2.2 High speed camera images of ignited $2\text{Al}\cdot 3\text{CuO}$ coating on a heated Nickel-Chromium filament.

2.3 Materials

Four different nanocomposite materials were used in this work, $2\text{Al}\cdot 3\text{CuO}$, $2.35\text{Al}\cdot \text{Bi}_2\text{O}_3$, $4\text{Al}\cdot \text{Fe}_2\text{O}_3$, and $8\text{Al}\cdot \text{MoO}_3$ produced by ARM. The starting components, elemental aluminum and oxide powders, were milled in hexane, used as a process control agent (PCA) under argon environment using a Retsch PM 400MA planetary mill. Custom vials designed to withstand incidental pressure increase were used. The starting materials are listed in Table 2.1. The milling media was 9.4 mm (3/8") diameter hardened steel balls, powder load was 30 g per vial and ball to powder mass ratio was 3. Additional details on the milling procedure and parameters can be found elsewhere [5, 36, 56], and a summary is given in Table 2.2.

Scanning electron microscope (SEM) images for all the nanocomposite powders are shown in Figure 2.3. All materials are composed of irregularly shaped particles ranging from very fine to relatively coarse. As shown in Figure 2.3, $2.35\text{Al}\cdot \text{Bi}_2\text{O}_3$ appears to be the finest powder.

In addition to chemically reactive nanocomposite thermites, a set of four reference inert samples was prepared by ball milling with compositions similar to those shown in Table 2.2, but with aluminum replaced by copper. The same milling conditions as used to prepare nanocomposite thermites were used to prepare these reference samples. The goal of preparation of such inert reference samples was to observe whether the decomposition of oxide would occur upon its heating in absence of aluminum, while

maintaining the shape, size, and morphology of oxides, which are important for the rates of their thermal decomposition.

Table 2.1 Starting Materials Used for Preparation of Nanocomposite Thermites

Material	Supplier	Particle Size	Purity
Al	Atlantic Equipment Engineers	325 mesh (<45 μm)	99.5%
CuO	Sigma-Aldrich	25 μm	99%
MoO ₃	Alfa Aesar	325 mesh (<45 μm)	99.95%
Bi ₂ O ₃	Alfa Aesar	325 mesh (<45 μm)	99%
Fe ₂ O ₃	Alfa Aesar	325 mesh (<45 μm)	99.5%

Table 2.2 Milling Conditions Used for Preparation of Nanocomposite Thermites

Material	Milling Time (min)	Volume of PCA, mL of Hexane
2Al·CuO	60	24
2.35Al·Bi ₂ O ₃	150	24
8Al·MoO ₃	30	24
4Al·Fe ₂ O ₃	60	20

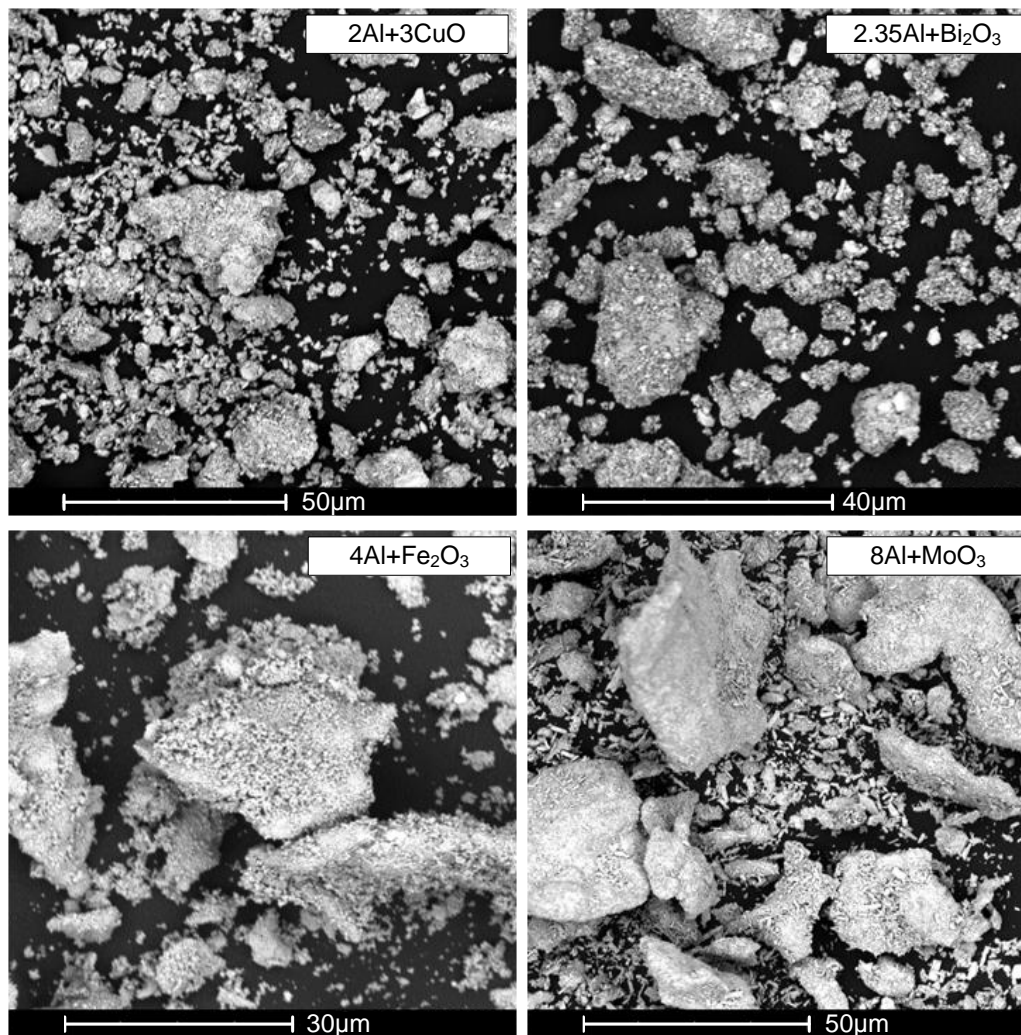


Figure 2.3 SEM images showing the powder morphologies for materials studied in this work.

2.4 Results

2.4.1 Pressure and Optical Emission Traces

No pressure or optical signatures were detected in experiments using any of the four prepared reference inert samples coated onto the electrically heated filaments. Figure 2.4 shows characteristic emission and pressure traces for each reactive material recorded at low heating rates. All pressure traces shown here and below are generated by the

dynamic (fast response) pressure transducer. Each plot also shows its respective temperature history for the filament. For consistency, all data are scaled over a 3-ms time interval. The onsets of pressure and emission signals effectively coincide with each other for each material. Note that scales for temperature, photodiode signal, and pressure are different for different traces. The ignition temperature for $2.35\text{Al}\cdot\text{Bi}_2\text{O}_3$ is noticeably lower, while its pressure pulse is much stronger compared to other materials. Both pressure and photodiode pulses are the sharpest for $2.35\text{Al}\cdot\text{Bi}_2\text{O}_3$ followed by $2\text{Al}\cdot 3\text{CuO}$ and then by relatively shallow pulses for $4\text{Al}\cdot\text{Fe}_2\text{O}_3$ and $8\text{Al}\cdot\text{MoO}_3$.

An unexpected observation was made when the heating rates increased: $2.35\text{Al}\cdot\text{Bi}_2\text{O}_3$ and $8\text{Al}\cdot\text{MoO}_3$ coatings did not ignite in vacuum when the heating rates exceeded 5,000 and 13,000 K/s, respectively. When ignition experiments were performed in ambient air (instead of the evacuated chamber), ignition for all nanocomposite thermites was observed at all heating rates.

Emission and pressure traces recorded for samples igniting at a low pressure at increased heating rates are shown in Figure 2.5; traces for $2.35\text{Al}\cdot\text{Bi}_2\text{O}_3$ and $8\text{Al}\cdot\text{MoO}_3$ coatings are shown for the heating rates below the threshold values above which ignition was no longer observed. The time scale spans for 10 ms for all traces shown. As in Figure 2.4, the scales for photodiode signal, pressure, and temperature are different for different traces. For all traces shown in Figure 2.5, except for $2.35\text{Al}\cdot\text{Bi}_2\text{O}_3$, the pressure pulse begins before the emission pulse. This effect became more and more

noticeable at higher heating rates. Comparing pressure and emission signals in Figures 2.4 and 2.5, one observes that the ignition temperatures are higher for all materials at higher heating rates. It is also interesting that the rates of increase of pressure and photodiode signals are higher at low heating rates. The effect is particularly strong for $2.35\text{Al}\cdot\text{Bi}_2\text{O}_3$. Unlike other materials, the maximum pressure achieved at the low heating rate for $2.35\text{Al}\cdot\text{Bi}_2\text{O}_3$ is almost an order of magnitude greater than that observed at the high heating rate. The effect of heating rate on the maximum pressure for other thermites is not pronounced.

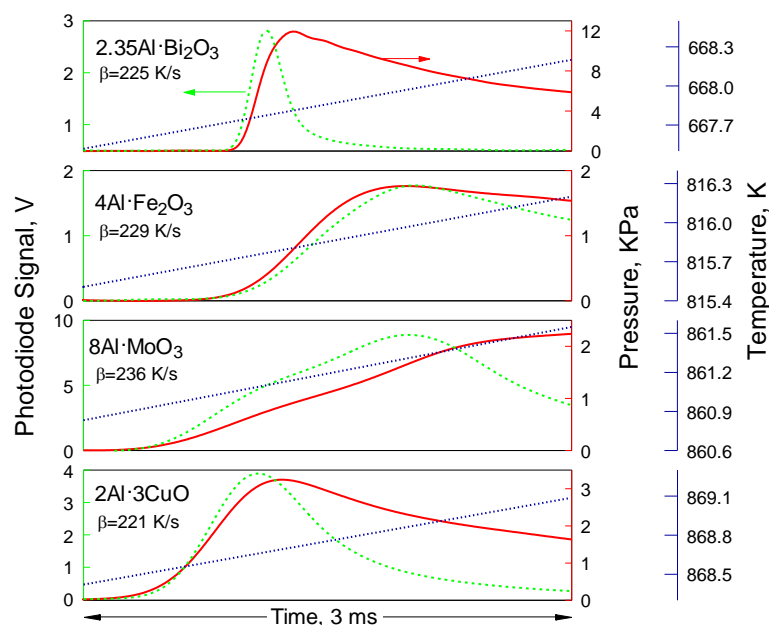


Figure 2.4 Photodiode signal and pressure traces recorded at a low pre-set heating rate for different materials. Temperature ramp is shown by a straight dotted line. Specific heating rate, β , is shown for each set of traces.

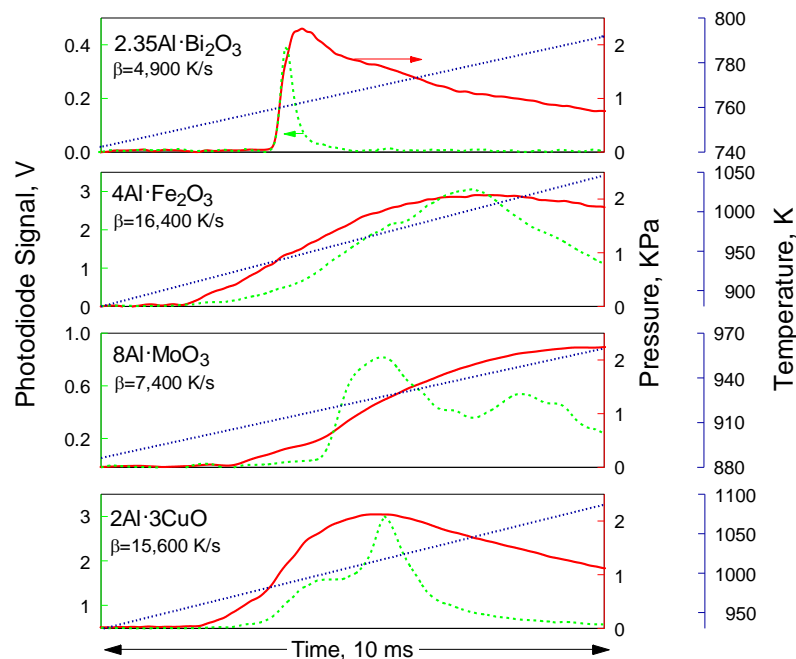


Figure 2.5 Photodiode signal and pressure traces recorded at a high pre-set heating rate for different materials. Temperature ramp is shown by a straight dotted line. Specific heating rate, β , is shown for each set of traces.

2.4.2 Effect of Heating Rate on Ignition Temperature

Ignition temperatures were consistently identified as the temperatures when the photodiode signal reached 1% of its maximum value. The results for different heating rates for all the four materials are shown in Figure 2.6. Each point represents at least 4 measurements. Here and below, the error bars show standard deviations of the individual data points. Note that both vertical and horizontal error bars are shown; however, for many points the horizontal error bars are smaller than the size of the symbol. Heating rates vary from ~ 200 to $\sim 17,000$ K/s. Note that the horizontal scale in Figures 2.6-2.8 is expanded for the heating rates below 2000 K/s. Despite the large vertical error bars, it is apparent that for all four materials at low heating rates (< 2000 K/s), the ignition temperature increases with the

heating rate. However, for all materials (except for $2.35\text{Al}\cdot\text{Bi}_2\text{O}_3$, for which the high heating rate measurements were limited) ignition temperatures remain relatively stable for heating rates above 2000 K/s.

For $2.35\text{Al}\cdot\text{Bi}_2\text{O}_3$, the ignition temperature increases as a function of the heating rate up to about 5000 K/s, just before the sample stops igniting. The ignition temperature for $2\text{Al}\cdot 3\text{CuO}$ is generally the highest of all the materials followed by $8\text{Al}\cdot\text{MoO}_3$, $4\text{Al}\cdot\text{Fe}_2\text{O}_3$, and $2.35\text{Al}\cdot\text{Bi}_2\text{O}_3$. All the materials except $2.35\text{Al}\cdot\text{Bi}_2\text{O}_3$ ignite in the range of 800 – 950K; $2.35\text{Al}\cdot\text{Bi}_2\text{O}_3$ ignites in the range of 650 – 800 K.

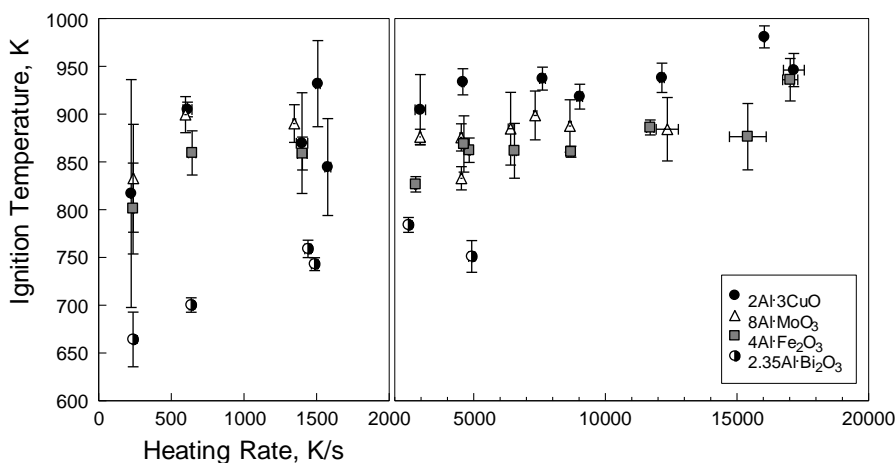


Figure 2.6 Ignition temperature as a function of the heating rate.

2.4.3 Effect of Heating Rate on Pressure Measurements

The recorded pressure traces were processed to identify the maximum pressure and average rate of pressure rise. The maximum pressure, P_{max} , was determined as the amplitude of the strongest peak in the recorded pressure trace. The average rate of

pressure rise characterizing ignition was determined as $\left(\frac{dP}{dt}\right)_{av} = \frac{P_{max} - 0.01P_{max}}{t_{P_{max}} - t_{0.01P_{max}}}$, where

$t_{0.01P_{max}}$ and $t_{P_{max}}$ are times when the pressure reaches 1% of P_{max} , and P_{max} , respectively.

The maximum pressures and average rates of pressure rise as a function of heating rate for all materials are shown in Figures 2.7 and 2.8, respectively. At low heating rates, $2.35Al \cdot Bi_2O_3$ generates a much higher maximum pressure than any other material. However, as the heating rates increase above 2000 K/s, the pressure generated by $2.35Al \cdot Bi_2O_3$ decreases markedly and becomes close to that generated by other materials. Except for $2.35Al \cdot Bi_2O_3$, the effect of heating rate on maximum pressure is weak for all materials.

The results for dP/dt are shown in a logarithmic scale because of significant differences in dP/dt between materials and because of substantial effect of heating rate on the dP/dt value. A general decreasing trend appears for dP/dt vs. heating rate for all materials. Ignition of $2.35Al \cdot Bi_2O_3$ has the highest dP/dt followed by $2Al \cdot 3CuO$, $4Al \cdot Fe_2O_3$, and $8Al \cdot MoO_3$ for most experimental runs. Of all four materials, $4Al \cdot Fe_2O_3$ has the smallest, while $2.35Al \cdot Bi_2O_3$ has the greatest change in dP/dt in the experimental range of heating rates.

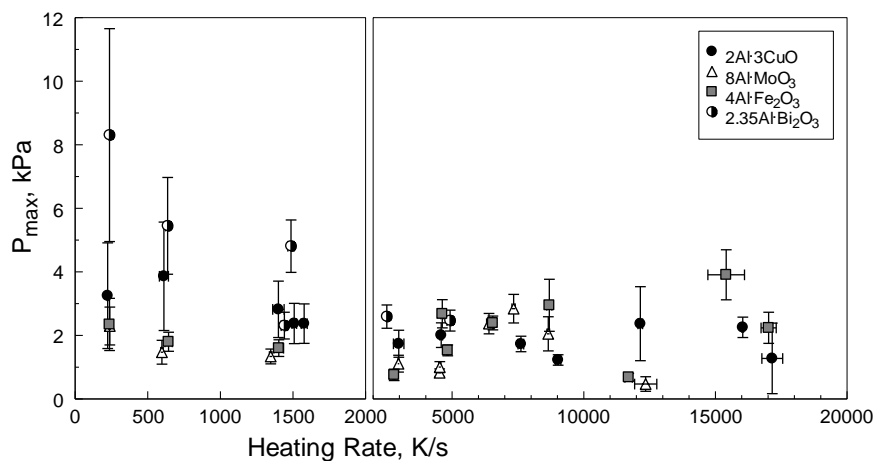


Figure 2.7 Maximum pressure as a function of heating rate.

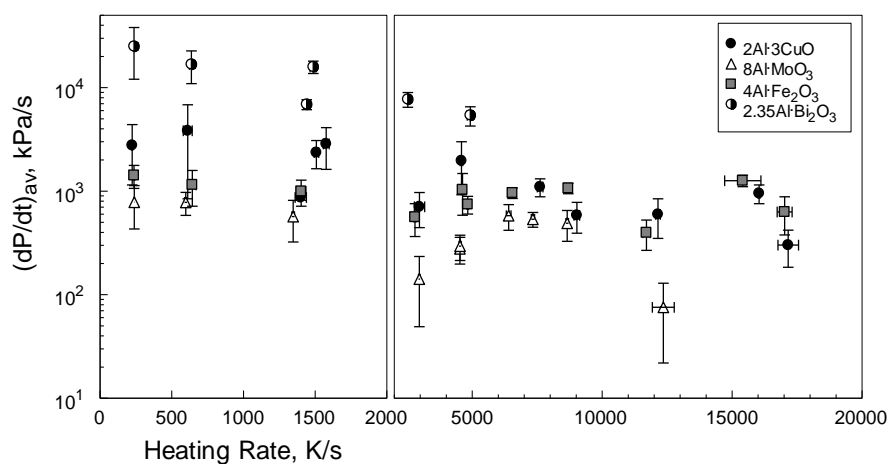


Figure 2.8 Average rate of pressure rise as a function of heating rate.

2.4.4 Time Delay Between the Pressure and Emission Pulses

As shown in Figure 2.5, at higher heating rates the pressure pulse is initiated before the detectable emission pulse. A more systematic presentation of the time shifts between the pressure and emission pulses is given in Figure 2.9. The pulse onsets are defined as instants when the respective signals (pressure or photodiode voltage) reach 1% of their maximum values. The time differences between onsets of the pressure and emission

pulses are shown for experiments performed with different materials and at different heating rates. As in Figures 2.6-2.8, the time scale of heating rates from 0 to 2000 K/s is expanded. Overall, the time difference is on the order of 1 ms. A slight increase in the time difference between the onsets of pressure and optical emission pulses is observed as the heating rate increases. Consequently, the corresponding onset temperatures for pressure and emission pulses shift to higher values proportional to the heating rate. The 8Al·MoO₃ composites show a noticeable time difference at heating rates as low as 600 K/s, while the time difference for all other materials becomes significant only at heating rates above 2000 K/s.

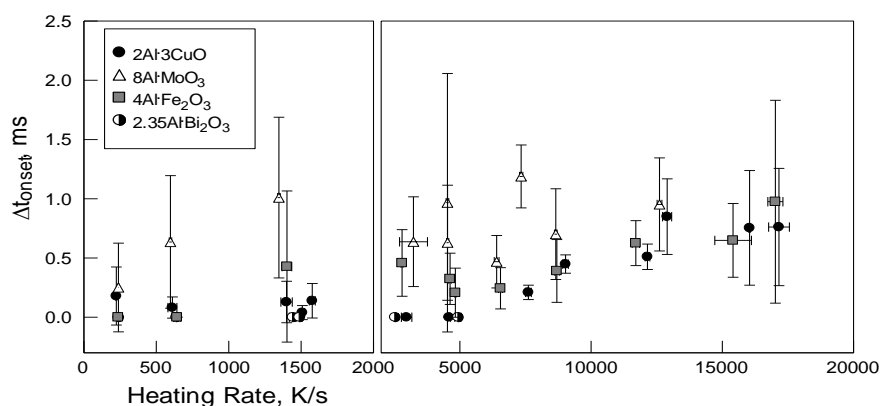


Figure 2.9 Time delay between onsets of the photodiode and pressure pulses as a function of the heating rate. Note that the temperature scales are different for the lower and higher heating rate sub-ranges.

2.5 Discussion

Present experiments show a certain correlation between optical emission and pressure pulses generated by ignited nanocomposite thermites. Several factors contribute to the pressure pulse. After ignition, transient gases are released that raise the pressure in the

chamber. Since the chamber at the beginning of the experiment has a finite pressure, the high combustion temperature causes the residual gas in the chamber to expand and raise the pressure as well. Finally, the oxidizer may decompose and release oxygen in the environment, which would also contribute to the pressure pulse. The recorded traces do not allow to distinguish separate features. However, transient gas release and the temperature effect are not present prior to ignition. The observation that the pressure pulse starts before the light emission therefore suggests that the oxidizers are decomposing prior to ignition.

Pressure and emission signals are not necessarily detected simultaneously. As the image sequence in Figure 2.2 shows, ignition of the powder coating starts locally at the edges and propagates along the filament length. In fact, the first sign of ignition may occur on the side of the filament facing away from the photo sensor, causing delayed detection of the light emission. This systematic mismatch between pressure and emission never causes emission to be detected earlier than the pressure pulse, and may contribute to the minor time difference observed for heating rates up to 5000 K/s for the Bi_2O_3 and CuO based composites (cf. Figure 2.9). At heating rates above 5000 K/s for all composites, and at all heating rates for MoO_3 based composites (Figure 2.9) the time mismatch becomes comparable to the propagation time of the combustion along the filament direction (cf. Figure 2.2), and is therefore unlikely to be caused by any obscuration effect. This provides a convincing argument for early oxidizer

decomposition and oxygen release as the source of the pressure pulse preceding the light emission. This is consistent with observations reported in Reference [48].

Further, this early oxidizer decomposition is not caused by thermal decomposition of the oxides, since no pressure signal was observed when chemically inert nanocomposite powders containing the same oxidizers were heated in vacuum. Therefore, it is reasonable to propose that the relatively slow, low-temperature reactions occurring during the powder heating prior to its ignition are not insignificant. Although the effect of such low-temperature reactions may not be substantial in terms of the added heat release, they are modifying solid oxidizers in contact with Al, e.g., by partially reducing the metal oxides. The presence of partially reduced oxide layers is suggested to destabilize the rest of the oxide and cause its further decomposition at relatively low temperatures. Although this mechanism is speculative at the present point of discussion, qualitatively similar behavior has been observed during the autocatalytic reduction of cuprous oxide to metallic copper at lower reaction rates [57]. Further investigation is warranted.

Acceleration of redox reactions leading to ignition in fully-dense, nanocomposite thermites was previously argued to be caused by changes in the transport properties of the growing Al_2O_3 layer separating the fuel and oxidizer [32, 33]. Such changes are not directly affected by decomposition of the oxidizer and thus may remain responsible for ignition. Because oxygen produced by the decomposing oxidizer generates a pressure

pulse, it is not immediately reacting with aluminum. Thus, it is likely that the principal effect of the observed oxygen release is to disrupt the thermal contact between the filament and powder coating. This, in turn, increases the likelihood of thermal runaway of the powder coating as a result of an exothermic redox reaction. The secondary effect of oxygen release, the changing properties of the decomposing oxidizer, could affect the rate of the respective redox reaction.

An increased delay between pressure and optical emission pulses at higher heating rates, as shown in Figure 2.9, indicates that different reaction kinetics laws govern changes in the transport properties of Al_2O_3 layer causing ignition, and oxygen release by the decomposing oxidizer. Indeed, if changes in transport properties of Al_2O_3 prompt an exothermic reaction leading to thermal runaway and ignition detected by optical sensor, the effect of heating rate on the temperature when the emission pulse occurs is governed by the respective kinetics of the Al_2O_3 evolution. If decomposition of oxidizer is characterized by different kinetics, the time delay between the decomposition (pressure pulse) and ignition (emission pulse) is expected to change as a function of the heating rate. However, these two processes are not independent of each other: they both depend on the extent of the preceding low-temperature redox reaction leading to both growth of the Al_2O_3 layer and depletion of oxygen from the partially reduced oxidizer.

It is of interest to discuss why ignition ceased to occur in vacuum for $2.35\text{Al}\cdot\text{Bi}_2\text{O}_3$ and $8\text{Al}\cdot\text{MoO}_3$ at higher heating rates, a somewhat unexpected effect observed in the present experiments. Ignition represents a thermal runaway, e.g., an exothermic process in the powder coating that must be fast enough to raise the powder temperature substantially above that of the filament. It cannot occur if the thermal conductivity of the powder coating is very high, so that the powder closely follows the filament temperature. A significant, three orders of magnitude, increase in thermal conductivity is well-known to occur in Bi_2O_3 at about 1003 K (730 °C), when a highly conductive, cubic $\delta\text{-Bi}_2\text{O}_3$ polymorph forms [58]. The reported polymorphic phase change temperature is higher than the ignition temperatures measured here (see Figure 2.6).

It was recently shown, however, that Bi_2O_3 polymorphs are oxygen deficient phases, $\text{Bi}_2\text{O}_{3-x}$, where x can vary from 0.022 to 0.033, and that different values of oxygen deficiency are associated with different polymorphs [59]. Changing the level of oxygen deficiency as a result of low-temperature reaction occurring while the material is heated prior to the detected ignition can alter stability of the initial Bi_2O_3 phase, reducing both its decomposition temperature and the temperature when the $\delta\text{-Bi}_2\text{O}_3$ polymorph is formed. For different heating rates, different levels of oxygen deficiency will be reached when the sample is heated to the same temperature. This can explain why the ignition is observed at low heating rates but stops occurring when the heating rates

increase. At low heating rates, the extent of low-temperature reaction is greater resulting in a more oxygen-deficient phase formed at relatively low temperature. Thus, decomposition of the oxygen-deficient oxide can occur at a much lower temperature than that expected for the oxide heated without a strong reducing agent (aluminum in our experiments). In other words, the decomposition would occur prior to the polymorphic phase change, resulting in the gas release and ensuing ignition.

For high heating rates, the oxide is less reduced, so that it may remain stable while being heated to higher temperatures. It thus approaches the temperature range when the polymorphic phase change is likely to occur; the temperature of the polymorphic phase change may still be somewhat reduced because of an increased oxygen deficiency in the oxide rapidly heated in presence of a reducing agent. If this happens, the thermal conductivity of the composite material would increase markedly and exothermic reactions occurring upon its further heating would be unable to result in a temperature runaway. Note that when the same experiment is performed in air, ignition is observed. This is easy to understand noting that the Bi_2O_3 partially reduced by low-temperature reaction with Al would quickly re-oxidize reacting with the ambient oxygen, so that the polymorphic transition would not occur until a higher temperature is reached. The information about thermal properties of MoO_3 is not as readily available as that for Bi_2O_3 ; however, multiple slightly oxygen deficient polymorphs of MoO_3 are also known [60] and are likely to have different thermal transport properties. Thus, a

scenario qualitatively similar to that described above for Al-Bi₂O₃ thermites may also be envisioned for Al-MoO₃.

The temperatures at which ignition is observed in the present experiments for 2Al·3CuO and 4Al·Fe₂O₃ can be compared to those reported in Reference [48] for analogous thermites comprising mixed nanopowders. The heating rates used in Reference [48] were close to 500,000 K/s, substantially higher than in the present experiments. The onset of gas release for 2Al·3CuO nanothermite occurred in the range of 850 – 1250 K [48]. Our results indicate ignition for 2Al·3CuO in a somewhat narrower (but overlapping) temperature range of 820 – 980 K, corresponding to the lower heating rate used. The difference between the present set of experiments and those reported in Reference [48] is relatively small. This suggests a weak effect of heating rate on ignition of 2Al·3CuO. For 2Al·Fe₂O₃, ignition was reported to occur in the temperature range of ca. 1100-1700 K. In the present experiments, the ignition occurred at lower temperatures (800 – 920 K), indicating an increase of ignition temperature with heating rate for this material, as is expected for a thermally activated initiation mechanism. Note that the Al/Fe₂O₃ ratio in thermites used in the present experiments was different from that used in Reference [48]; however this difference is expected to be insignificant for the initiation reaction, involving only a small fraction of material. Based on a difference in the effect of heating rate on ignition temperature for nanocomposite thermites using CuO and Fe₂O₃ as oxidizers, it is suggested that different

processes serve as ignition triggers for these two materials. A heating rate independent process, such as an invariant phase change may be triggering ignition in the Al-CuO system. However, it appears that a thermally activated reaction, such as exothermic oxidation accelerating at greater temperatures, may be the ignition trigger for Al-Fe₂O₃nanothermites.

Considering an earlier discussion on the importance of change in transport properties of the growing Al₂O₃ layer in triggering ignition, the observed difference in the effect of heating rate on ignition temperature for different thermites suggests that the respective Al₂O₃ layers are modified by different oxidizers. In other words, the redox reaction product may have slightly different compositions (e.g., involving ternary Al-Fe-O or Al-Cu-O phases) causing differences in its stability and polymorphic phase changes occurring upon its heating.

Finally, it is interesting to consider the observed effect of heating rate on the pressure pulses produced by different materials. A strong increase in the maximum pressure at lower heating rates was observed for 2Al·Bi₂O₃ (cf. Figure 2.7). Incidentally, this is the only thermite system considered in the present work, for which no large separation between the pressure and emission pulses upon ignition was observed. Thus, it remains unclear whether the observed pressure pulse (in the case of Bi₂O₃) is associated primarily with oxygen release, or it is caused exclusively by the vapor-phase reaction products and the temperature effect. It is reasonable to assume that at lower

heating rates, the extent of the low-temperature redox reaction is greater, leading to a greater partial reduction of Bi_2O_3 and growth of a thicker interfacial Al_2O_3 layer. At the same time, because of the relatively long low-temperature reaction times available at low heating rates, both oxygen concentration and temperature gradients in the decomposing Bi_2O_3 may be lower compared to the experiments performed at high heating rates. This would suggest that when ignited, the decomposition of Bi_2O_3 will proceed in its entire volume, whereas at high heating rates, heat and mass transport within the decomposing oxide might be affecting the reaction rate. Note that this reasoning can apply to other thermites as well, helping one to understand accelerated pressure rise observed consistently at lower heating rates (cf. Figure 2.8).

Several other processes could have occurred leading to lower rates of pressure rise consistently observed at higher heating rates. The rate of pressure rise can be negatively affected by temperature gradients in the powder coating increased at higher heating rates [61]. The increase in the temperature gradient would cause particles in immediate contact with the wire to ignite sooner than the particles located in the external layers of the coating. This process would generate a lower and less sharp pressure pulse compared to that produced by the entire powder coating ignited simultaneously. For the powders exhibiting a pressure pulse ahead of the emission pulse, part of the sample might be blown off the filament, so that the stronger the shift between pressure and emission, the less material may remain on the filament to ignite. In addition, an early release of

gaseous oxygen by decomposing oxide (occurring prior to ignition, with greater shift in oxygen release and ignition events at higher heating rates) can change the overall sample stoichiometry. Part of the gasified oxygen can diffuse away from the aluminum surface, thus reducing the amount of the oxidizer available for the thermite reaction.

2.6 Conclusions

Ignition of nanocomposite thermites upon their heating in vacuum is accompanied by pressure and optical emission pulses; these pulses do not occur simultaneously and the delay of optical pulse compared to the pressure pulse increases at higher heating rates. No pressure or optical emission is detected in similar experiments with reference inert nanocomposite samples, in which aluminum is replaced with copper. Pressure pulse and associated gas release detected in experiments with nanocomposite thermites heated in vacuum are assigned to oxygen generation by decomposing metal oxides for $2\text{Al}\cdot 3\text{CuO}$, $4\text{Al}\cdot \text{Fe}_2\text{O}_3$, and $8\text{Al}\cdot \text{MoO}_3$. However, this assignment could not be made unambiguously for $2.35\text{Al}\cdot \text{Bi}_2\text{O}_3$. The oxygen release is suggested to be caused by destabilization of the metal oxides partially reduced during a relatively slow, low-temperature redox reaction preceding ignition. Ignition is suggested to be triggered by a change in transport properties of the growing Al_2O_3 layers. These changes may be affected by the type of oxidizer, modifying the chemistry and properties of the produced Al_2O_3 -based layer. Both growth of Al_2O_3 layer leading to its changing transport

properties, and decomposition of metal oxide upon heating are directly affected by the low-temperature redox reactions preceding ignition.

CHAPTER 3
ON GAS RELEASE BY THERMALLY-INITIATED FULLY-DENSE
2Al₃CuO NANOCOMPOSITE POWDER

3.1 Introduction

There are multiple recent efforts aimed to understand and model ignition mechanisms of nanocomposite reactive materials [5, 31, 32, 37, 48, 62-67]. Although significant progress has been made, ignition mechanisms remain elusive. In addition, a robust ignition model is required to incorporate these materials in practical energetic formulations. Ignition of nanocomposite reactive materials needs to be described for a wide range of applications, including propellants, explosives and pyrotechnics [8, 10, 68]. At present, several limitations exist in the proposed relevant ignition models. In particular, a recent model for low-temperature exothermic reactions in nanocomposite 2Al₃CuO thermites was developed [31, 33] based on thermo-analytical studies, microcalorimetry, and single particle ignition experiments. This model is capable of interpreting the thermo-analytical experiments and ignition of individual thermite particles in a laser beam. However, it does not predict ignition of such particles in experiments where they are coated on an electrically heated filament. The model describes the evolution of the aluminum oxide layer growing between Al and CuO and respective changes in its diffusion resistance as critically affecting the rate of exothermic redox reaction leading to ignition.

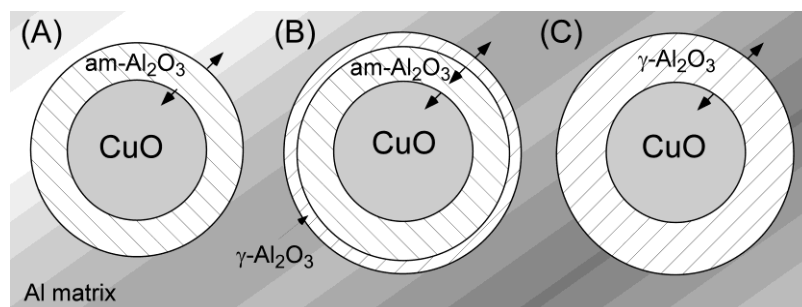


Figure 3.1 Configurations of CuO core, Al matrix, and Al₂O₃ shells for different reaction progress (see text for details).

The schematic of Figure. 3.1 illustrates a CuO inclusion within a continuous aluminum matrix, separated by an evolving layer of alumina. Individual phases are shaded differently, and arrows indicate the movement of interfaces. The unreacted nanocomposite material is characterized by the number and size of CuO inclusions, and by the initial thickness of the amorphous Al₂O₃ layer separating CuO and Al. The thin layer of amorphous alumina (shown in 3.1A) initially grows according to the Cabrera-Mott (CM) mechanism [31, 32, 39]. As the thickness increases, the CM reaction becomes less significant, and ordinary diffusion dominates. At some critical thickness, the amorphous alumina transforms into the γ -Al₂O₃ polymorph. The transformation is set to begin at the outer radius of the amorphous shell and propagates radially inwards as shown in Figure 3.1B. After all the amorphous alumina is consumed, the remaining γ -oxide continues to grow, as illustrated in Figure 3.1C. The model developed by [33] describes the Al+CuO reaction as rate limited by transport of the reacting species through the evolving alumina film; thus, it links diffusion rates and rates of phase changes affecting the diffusion resistance of this film with the rate of

reaction. The model describing reaction between Al and CuO does not consider any melting relations that may be observed in pure Al, or in various Al-Cu alloys once metallic Cu becomes available. The inability of that model to describe ignition in the heated filament experiments was suggested to be associated with possible gas release accompanying ignition [31, 48, 66]. This gas release could change thermal diffusivity of the powder layer coated on the filament; it can also provide gaseous oxidizer, which could alter the reaction mechanism between Al and CuO.

Heated filament experiments were previously conducted using a fully-dense nanocomposite powder of $2\text{Al}\cdot 3\text{CuO}$ prepared by Arrested Reactive Milling (ARM) [27] to investigate the effect of heating rate on its ignition behavior [31, 57]. The experiments were conducted at normal pressure and in the presence of an external oxidizer. In such experiments, pressure is generated upon ignition due to several processes: release of oxygen by decomposing oxidizer, formation of gaseous combustion products including suboxides of Al and boiling Cu vapors, and expansion of the gas trapped in pores. Only the former process is relevant to the ignition mechanism of interest in this study. Recently, heated filament ignition experiments were performed in vacuum for several nanocomposite thermites prepared by ARM [40]; in those experiments both pressure and optical emission signals were monitored simultaneously. In this paper, experimental work for $2\text{Al}\cdot 3\text{CuO}$ is expanded. Results are reviewed and interpreted considering the detailed model for heterogeneous redox reaction proposed for this material by [33]. The

correlation of the measured gas release with the described redox reactions and its effect on the ensuing ignition processes are considered in particular.

3.2 Experimental

3.2.1 Materials

The nanocomposite powder used in this work is $2\text{Al}\cdot 3\text{CuO}$ produced by ARM [27]. The starting material was a blend of aluminum and copper oxide powder. Aluminum powder (-325 mesh) of purity 99.5% was provided by Atlantic Equipment Engineers. Copper oxide powder by Sigma-Aldrich (25 μm) of 99+% purity was used. These starting components were milled in hexane and under argon environment for 60 min using a Retsch PM 400MA planetary mill. Additional details on the milling procedure and parameters can be found elsewhere [56]. As a reference, a chemically inert $2\text{Cu}\cdot 3\text{CuO}$ nanocomposite was also made under same milling parameters. Aluminum was replaced by copper powder provided by Alfa Aesar (-325 mesh, 99% purity). The resulting reference composite powder was expected to have the same particle sizes and morphology of mixing CuO in the metal matrix as the reactive thermite powder, but stay chemically inert. Scanning electron microscope (SEM) images for both powders are shown in Figure. 3.2 and a typical particle size distribution (PSD) for $2\text{Al}\cdot 3\text{CuO}$ given in Figure 3.3.

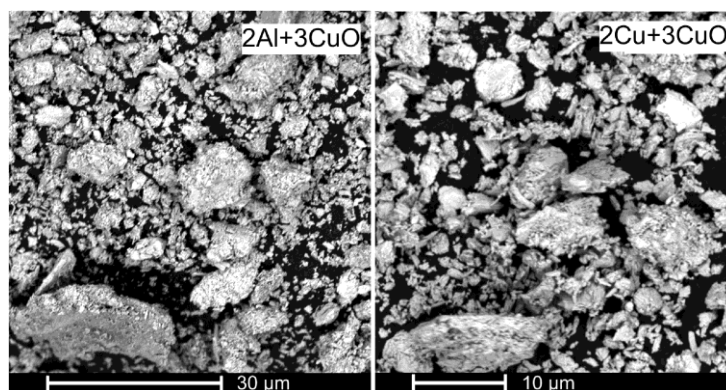


Figure 3.2 SEM images showing the powder morphologies of the powders used in this work. Left and right images show $2\text{Al}\cdot 3\text{CuO}$ and $2\text{Cu}\cdot 3\text{CuO}$, respectively.

The SEM images of $2\text{Al}\cdot 3\text{CuO}$ revealed irregularly shaped particles, mostly sized in the range of 10 – 30 μm , with no visible agglomerations. Smaller particles were also present and a minute portion of unreacted CuO (cylindrically shaped) particles that were not incorporated in the Al matrix could be seen. This material appears to be fairly well mixed with no visible formation of aluminum oxide or reduced metallic copper. The $2\text{Cu}\cdot 3\text{CuO}$ nanocomposite consisted of particles sized similarly to $2\text{Al}\cdot 3\text{CuO}$. These inert composite particles are also mainly irregularly shaped and apparently represent a good reference material for the reactive composite powder studied here.

The typical PSD, shown in Figure 3.3, is used to evaluate the number of $2\text{Al}\cdot 3\text{CuO}$ powder layers expected to be coated onto an electrically heated filament. The PSD was obtained using a Beckman-Coulter LS230 Enhanced Particle Analyzer and the powder was determined to have a volumetric mean particle size of 28.6 μm .

Based on the total coating layer thickness of $\sim 90 \mu\text{m}$ (cf. Figure 3.5a); it can include from 2-3 to as many as 10-15 layers of powder, depending on its packing. The

powder clearly includes a large number of fine particles with sizes less than 10 μm , which form multiple layers mixed with much larger particles, which could penetrate through several finer particle layers.

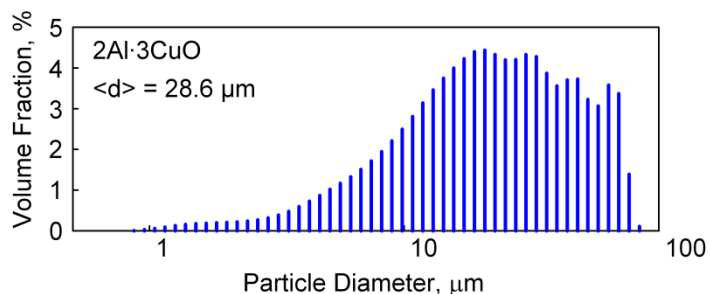


Figure 3.3 Particle size distributions of the nanocomposite 2Al·3CuO powder used in this work.

3.2.2 Filament Ignition

The experimental apparatus used in this work and shown schematically in Figure 3.4 consists of two key components: the electrical circuitry to heat the filament and the diagnostics to determine the time, temperature and pressure associated with ignition. The experiment was performed in a miniature vacuum chamber with a volume of 31 ml, selected to increase the sensitivity to real-time pressure changes. The chamber was constructed using polyoxymethylene having high stiffness and good dimensional stability. A removable window to the chamber was made of polycarbonate, transparent for optical observations.

The chamber was designed with customized airtight ports for static and dynamic pressure transducers. The absolute pressure was monitored using a low-frequency (static) pressure transducer, Omegadyne model PX209-30V45G5V with applicable pressure range of -14.7 to 45 psi (0 to 412 kPa). A PCB piezoelectric pressure sensor with a model 106B51 microphone was used for dynamic pressure measurements. It is well suited to record rapid changes in the chamber pressure associated with ignition. The dynamic pressure sensor was mounted in the chamber wall, in the proximity of the ignited powder to minimize any possible delays associated with the sound propagation through the chamber.

The chamber pressure was reduced prior to experiments using a platinum series JB model 0808 vacuum pump.

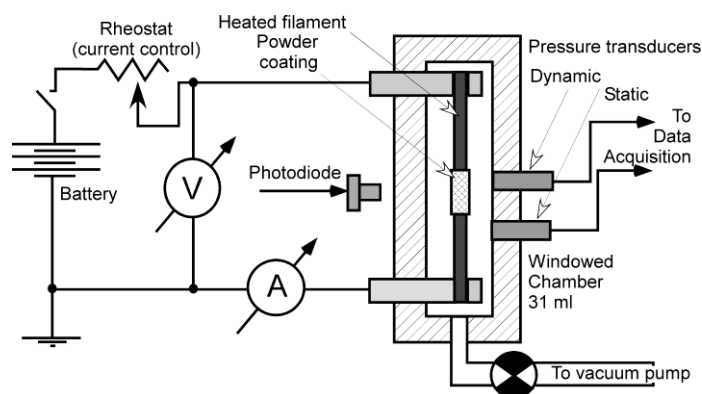


Figure 3.4 Schematic layout of the heated filament ignition apparatus.

The static pressure transducer provided an initial reading of pressure in the chamber, typically 2.5-5.0 kPa. Small leaks in the apparatus remained, so that once the

pump was turned off, the pressure increased slightly. The rate of pressure rise did not exceed 1 kPa/min. For consistency, all experiments were started at a static gauge pressure reading of 5.80 kPa and at least 5 experiments were carried out at each pre-set heating rate.

The filament (nickel-chromium alloy, diameter $\approx 492 \mu\text{m}$) was manually strain hardened (stretched) and cut into 6-cm sections prior to attaching it to the electrodes. A thin layer of thermite powder was coated on a 5-mm long section of the filament. To prevent sagging of the heated filament because of thermal expansion, one of the filament holders/electrodes was spring loaded. The window of the chamber was specially designed with electrical feed throughs for connection of the powder-coated wire to an external circuit. Multiple identically coated filaments were heated at different rates and ignition was monitored using real time optical emission and pressure measurements. Variation in the heating rate from 200 to 16,000 K/s was achieved using a voltage source including up to three car batteries connected in series and a rheostat. A current sensor by F.W. Bell CLN-50 (Inductor coil) and a voltage divider both powered by Tenma regulated DC power supplies were used to measure current and voltage through the circuit.

An SEM image of a typical, approximately 90- μm thick powder coating on the wire, and high speed camera images of the as deposited and ignited powders are shown in Figure 3.5. The optical emission signals were measured in real time using a Thorlabs

DET110 photodiode placed directly in front of the window of the chamber. Signals from the dynamic pressure transducer, photodiode, current and voltage measurement devices were recorded by a LeCroy WaveSurfer 64Xs Series oscilloscope. Current and voltage signals were used to calculate the filament temperature as a function of time, and thus the heating rate.

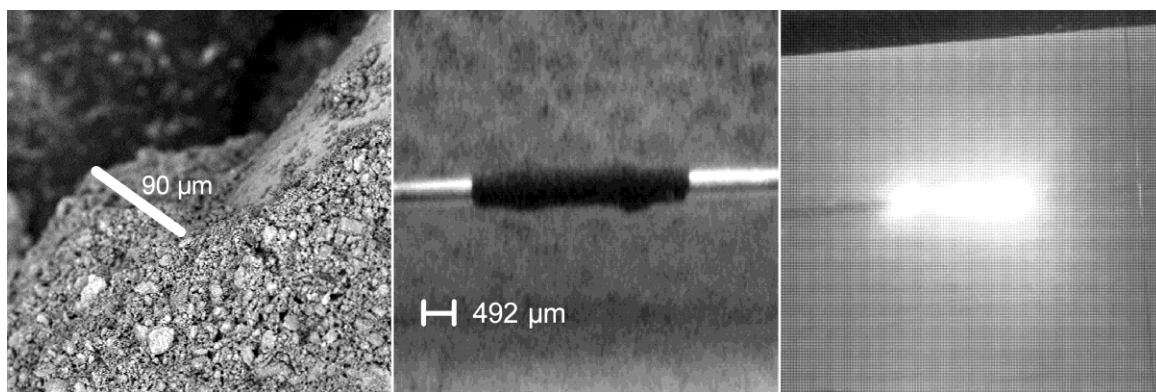


Figure 3.5 (a) SEM image of the nickel-chromium wire coated with nanocomposite 2Al•3CuO powders, (b) High speed camera image of freshly coated wire and (c) High speed camera image of the ignited coating.

A typical experimental record of emission and pressure upon ignition is shown in Figure 3.6. The data processing procedure involved determining the heating rate and the ignition temperature.

The heating rate was calculated assuming that the filament with mass m and specific heat C_p is heated by electric current adiabatically, so that, where I and V are the measured electric current and voltage, respectively. This estimate neglects the heat capacity of the coating compared to that of the filament and assumes a constant value of

Cp. This approach was found valid based on previous comparisons of the calculated filament temperature with that measured using an infrared pyrometer [54]. The thermal contact between the powder and filament is assumed to be very good so that the calculated heating rate can be applied to the powder as well as to the filament. The heating rate was observed to be constant over the duration of the peaks, and the absolute temperature, obtained by integrating the heating rate was found to be reproducible to within ± 25 K.

Since both pressure and emission signals were recorded, the ignition temperature could be determined from the onset of either one of them. For further analysis, the onset of the emission signal is taken as the time and corresponding temperature of ignition. The signal onsets were determined by fitting a straight line to a short section preceding the peaks, and subtracting that baseline from the signals. The root mean square (RMS) noise over the fitted section was determined, and the signal onset was identified when the signal exceeded the RMS noise by a factor of three.

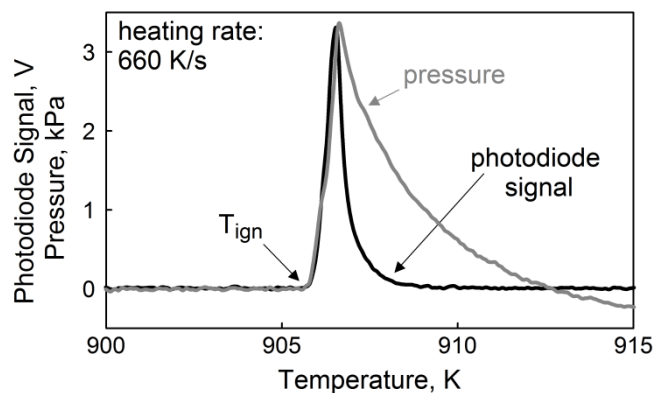


Figure 3.6 Photodiode and pressure signal for an ignited $2\text{Al}\cdot 3\text{CuO}$ sample.

3.2.3 Thermal Analysis

In addition to the ignition experiments, reactions in the prepared powders were characterized using Differential Scanning Calorimetry, DSC, at heating rates of 5, 10, and 20 K/min. A Netzsch simultaneous thermal analyzer STA 409 was used, samples were heated in argon and the methodology described by [37] was generally followed. Measurements were carried out with a sample mass of 2-5 mg of loosely packed powder loaded into the DSC sample carrier. The instrument was calibrated for temperature with the melting points of a set of metal standards resulting in a temperature accuracy of $\pm 1^\circ\text{C}$. To establish reproducible initial conditions for the DSC measurements, each sample was heated from room temperature to 50°C at $20^\circ\text{C}/\text{min}$ and kept at 50°C for about 60 min prior to the main heating program. The device was thoroughly flushed with argon prior to start of each experiments and flow rate controlled at $50\text{ mL}/\text{min}$ during experiments. The traces were baseline-corrected by subtracting the signal recorded during the second heating of the same sample and normalized by original sample mass.

3.3 Computations

The reaction mechanism for $2\text{Al}\cdot 3\text{CuO}$ nanocomposites outlined in the Introduction was implemented in MATLAB. Critical material parameters influencing the model are the number and size of the CuO inclusions, and the initial thickness of the alumina layer separating CuO from Al (cf. Figure 3.1). This thickness was determined earlier based

on low-temperature heat flow calorimetry [31, 32]. The inclusion size was varied between 100 and 200 nm, and the number of inclusions was adjusted to achieve the overall composition of $2\text{Al}+3\text{CuO}$. This implementation had been used to compute thermal analysis curves in Reference [33], and was applied here as well. The computation assumed constant heating rates, corresponding to experiments. The heat losses from the sample were neglected. The temperature-invariant phase changes in the sample, such as aluminum melting, were assumed to occur fast compared to the rate of temperature change, so that their respective effects on the oxidation kinetics were neglected. Further details of the algorithm are given by Reference [33].

To model the ignition of particles coated on a filament, heat transfer between filament, coating, and environment needs to be modeled accurately. An algorithm for this was previously published by Reference [61], and was incorporated in a separate code. Briefly, the coating was modeled as a close packing of uniformly-sized spheres surrounding the filament in concentric layers. Heat is allowed to flow via conduction and radiation between adjacent layers and from and to the filament and the environment. Since the experiments were performed in vacuum, convection was not allowed in the computations. The size of these spheres represents the average particle size of the powder. Considering the particle sizes shown in Figure 3.3 and the measured coating thickness shown in Figure 3.5, it was assumed that the coating consisted of three concentric particle layers.

3.4 Results

As illustrated in Figure 3.6, both pressure and optical emission peaks were recorded when the nanocomposite $2\text{Al}\cdot 3\text{CuO}$ powders were heated in vacuum, clearly marking ignition events. At low heating rates, the onset of the pressure signal nearly coincided with the onset of the emission signal; however, the emission was delayed by about one millisecond at the highest heating rates. Figure 3.7 shows this time difference between the onset of the pressure and emission signals.

No pressure or optical emission signals were observed upon heating of the prepared reference samples in which aluminum was replaced with copper.

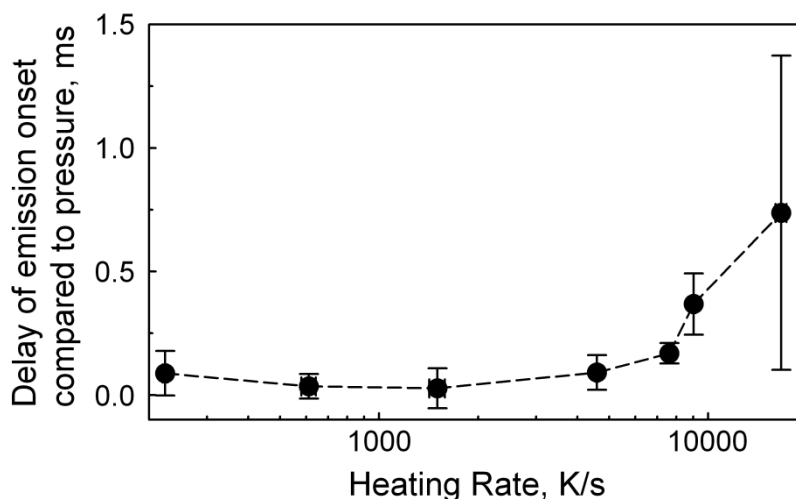


Figure 3.7 Effect of heating rates on the shift between onsets of pressure and emission pulses.

3.4.1 Thermal Analysis and Ignition

Figure 3.8 shows an experimental heat flow curve recorded at 20 K/min. For comparison, two calculated heat flow curves are shown as well, with CuO inclusion sizes

of 100 and 200 nm, respectively. The experimental curve shows the following features: a low-temperature onset of the exothermic reaction near 400 K, after which the heat flow remains nearly constant until it increases slightly starting at about 700 K. An endothermic peak occurs above 800 K, and was previously attributed to equilibrium melting reactions in the Al-Cu binary system [37]. Finally, a strong exothermic peak is observed near 900 K.

The computed curves match various aspects of the experiments and help illuminate the underlying processes. To clarify different features observed in the computed curves, consider Figure 3.9, which shows the individual processes contributing to the heat flow according to the current model. The processes identified are: the growth of an amorphous alumina layer controlled by CM kinetics, growth of amorphous alumina controlled by conventional diffusion, and growth of γ alumina also by conventional diffusion.

Growth of only one of the alumina polymorphs is taken as rate-controlling at any given time. As a result of this, the transition between the amorphous and γ alumina polymorphs causes a step-wise change in the reaction rate at the time and temperature when the growth of γ alumina becomes rate-limiting. This is a simplification chosen for computational feasibility, since in actuality the amorphous and γ polymorphs will grow at the same time over some temperature range, and the reaction rate will be limited by diffusion through both. However, it was previously shown that this simplification

matches the underlying physical process reasonably well for the transition between amorphous and γ alumina [34, 69].

The top two plots in Figure 3.9 show the heat flow under thermal analysis conditions, where heat transfer effects were neglected. The top curve corresponds to an actual experimental heating rate. The CM reaction dominates at low temperatures. As the temperature increases, the rate of CM reaction decreases as a result of increasing oxide thickness. At the same time, the rate of conventional diffusion through amorphous oxide layer increases, resulting in a first exothermic peak. As the temperature continues to increase, so does the oxide thickness resulting in a slower rate of diffusion. At some point defined by a combination of temperature and oxide thickness, a polymorphic phase transition producing γ alumina occurs. Because γ alumina is much denser than amorphous alumina, this phase transition is accompanied by disruption of the oxide layer continuity. Thus, a sharp increase in the reaction rate is observed. As the reaction continues, the openings in the oxide heal and the reaction rate slows down. For the heating rate corresponding to the top curve in Figure 3.9, the polymorphic phase change occurs by the end of the first exothermic peak.

The center curve shows an intermediate heating rate between rates typical for thermal analysis and filament ignition experiments. For this intermediate heating rate, the conventional diffusion through amorphous oxide accelerates at higher temperatures,

but the phase change yielding γ alumina is predicted to occur well before the end of this first exothermic peak.

The bottom curve is calculated for a high heating rate, with heat flow to and heat losses from the powder coating accounted for. In this calculation, accounting for temporal changes in the sample properties and temperature, the temperature remained constant during Al melting. As a result, the thickness of the alumina layer continued to increase at the aluminum melting point of 933 K, causing a reduction in the CM reaction rate and a small step observed at that temperature. More importantly, the reaction controlled by conventional diffusion through the amorphous oxide starts accelerating at even higher temperatures and is immediately interrupted by the polymorphic phase change.

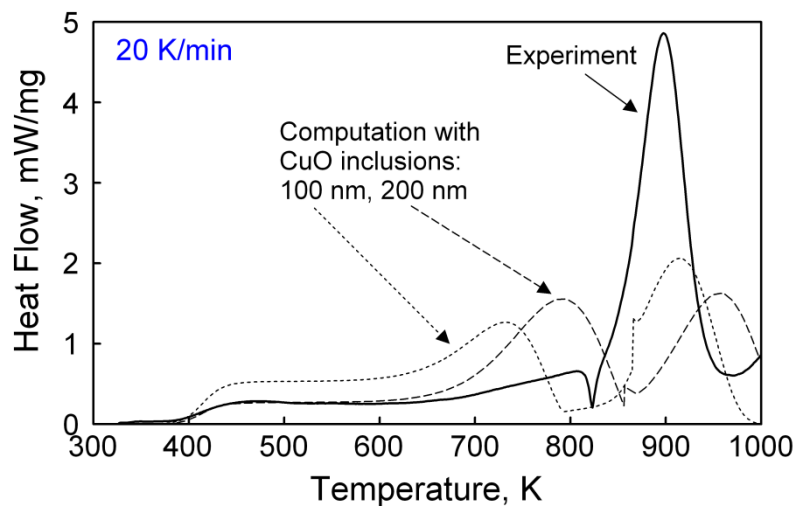


Figure 3.8 Experimental and computed DSC curves for the nanocomposite $2\text{Al}\cdot 3\text{CuO}$ powder.

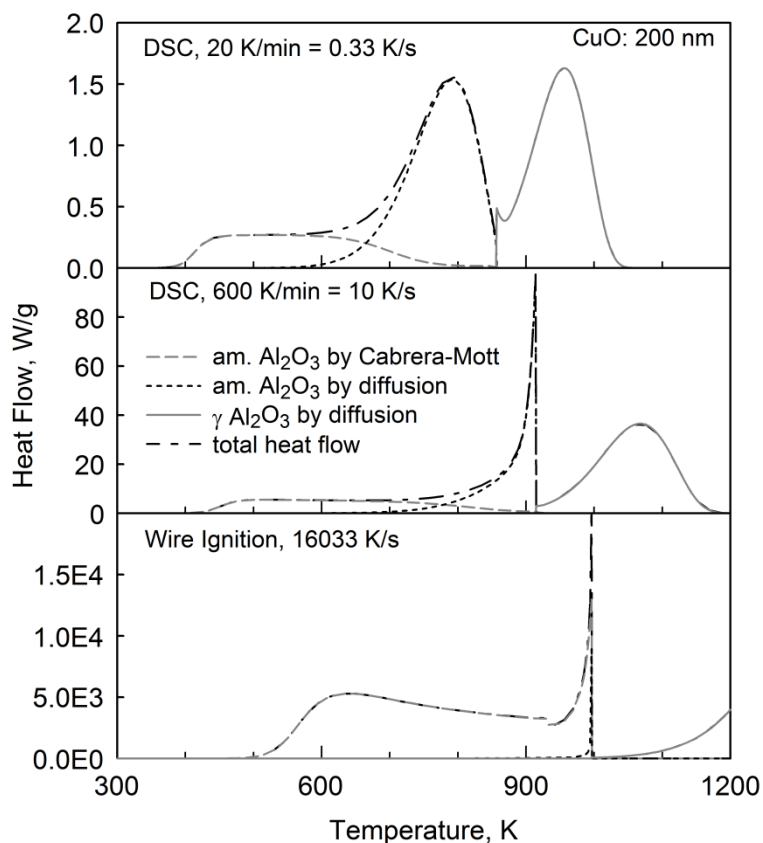


Figure 3.9 Computed heat flow curves under thermal analysis conditions (no heat transfer effects), and under filament ignition conditions (accounting for heat transfer to and from the powder coating). Component reactions are shown.

To relate thermal analysis experiments at lower heating rates and ignition experiments at high heating rates, it is instructive to compare suitable reference points on a plot of logarithmic heating rate vs. inverse temperature. Following our earlier work [35, 37], a plot in Kissinger coordinates (e.g., [70]) is shown in Figure 3.10. Experimental data are shown by symbols, and results of computations are shown by lines. The following reference points were chosen:

(1) To track the start of the CM-controlled growth of amorphous alumina, the low-temperature inflection point (peak of the derivative of the heat flow) was identified in the experimental thermal analysis measurements (circles in Figure 3.10) as well as in the corresponding computations under DSC heat flow conditions (solid line at low temperatures).

(2) A weak inflection point could be identified in the experiments in the 700-800 K range (referred to as inflection point before Al melting in Figure 3.10). It is shown by squares in Figure 3.10. In the computations for the DSC heat flow conditions, this inflection point is predicted when the rate at which amorphous alumina grows by diffusion accelerates (see Figure 3.9, top curve, the onset of the first exothermic peak). The leading inflection point of the corresponding peak is shown by a solid line at the respective temperature. The solid line has two nearly straight sections. The first section, at lower heating rates, corresponds to the inflection point defined by the shape of the exothermic peak produced by the accelerated diffusion, as shown in top curve in Figure 3.9. As the heating rates increase, the peak is interrupted by a phase change (see center curve in Figure 3.9), and the inflection point coincides with the resulting sharp spike produced. This effect is represented by the second portion of the calculated line, showing a smaller change in temperature as a function of the heating rate.

(3) The DSC peak near 1000 K is shown by triangles.

(4) Filament ignition temperatures, as measured in the vacuum chamber, are shown by stars.

(5, 6) Computations under filament ignition conditions are shown by dashed lines: the low-temperature inflection point leading to the CM growth of amorphous alumina, and the inflection point before Al melting, leading to the diffusion-controlled growth of amorphous alumina at higher temperatures. Although a detailed heat transfer model was accounted for in calculations for the filament ignition experiments and neglected for DSC experiments, the kinetic trends predicted for the two inflection points tracked in both calculations are consistent with each other.

Ignition clearly correlates with the kinetic trend predicted for the sharp spike caused by the polymorphic phase change in the growing alumina.

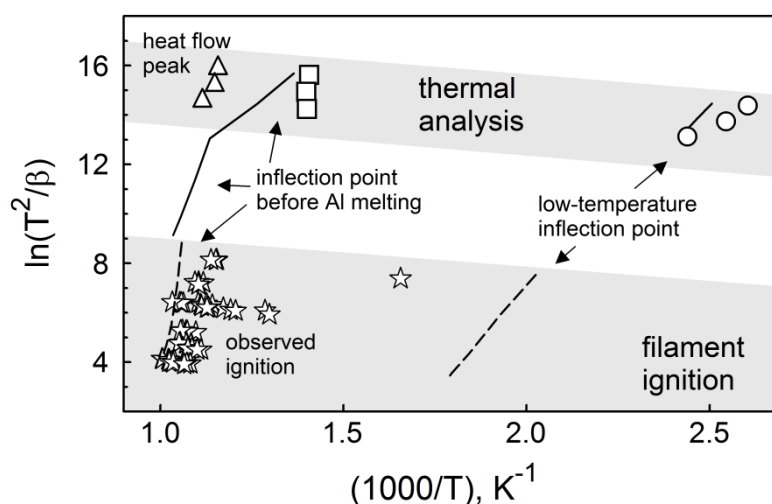


Figure 3.10 Summary of experimental DSC features, filament ignition temperatures, and corresponding computational results (200-nm CuO inclusions). See text for details.

3.4.2 Partial Reduction of CuO and Ignition

Despite earlier successful numeric modeling of powder coated on an electrically heated filament [61], and equally successful prediction of single-particle laser ignition of $2\text{Al}\cdot 3\text{CuO}$ composite particles [33], the current calculations did not predict a thermal runaway for the powder. In many cases, the evolved heat was not even sufficient to raise the nanocomposite powder temperature above that of the filament. Therefore, ignition was not predicted directly. At the same time, the model does not account for the gas release, which caused the pressure peak preceding ignition. The gas release possibly dramatically reduced heat transfer between powder and filament, so that the powder temperature could have increased much higher than predicted in a model considering the powder coating. Although not predicting the gas release directly, the model describes the rate of oxygen consumption by the redox reaction beginning at low temperatures (as specified by the Cabrera-Mott mechanism) and thus predicts a change in the oxygen concentration in the copper oxide serving as an oxidizer. This partial reduction of copper oxide is suggested to result in its reduced stability and lead to its eventual decomposition accompanied with the release of gaseous oxygen. Indeed, without the low-temperature redox reaction, as was the case in experiments with the reference inert $2\text{Cu}\cdot 3\text{CuO}$ composite, no CuO decomposition was observed in the entire range of temperatures. Thus, correlations between observed ignition temperatures and predicted compositions of the partially reduced copper oxide are of interest. Figure 3.11

shows experimentally observed ignition temperatures as a function of the heating rate. In addition, curves of constant oxygen consumption are shown for values corresponding to the reduction of CuO to CuO_{0.98}, CuO_{0.97}, and CuO_{0.95}, respectively. Finally, the temperature of the sharp heat flow peak (see Figure 3.9, bottom) is indicated as well.

According to the results summarized in Figure 3.11, the amount of oxygen consumed at the temperatures where ignition is experimentally observed is significant. Therefore, it is hypothesized that the copper oxide partially reduced as a result of low-temperature redox reaction has its properties altered compared to the starting CuO. In particular, a substantial decrease in the thermal stability is expected for the partially reduced CuO_{1-x} phases, with $0 < x < 1$. The unstable CuO_{1-x} can decompose with release of gaseous oxygen at temperatures substantially lower than decomposition of CuO normally occurs. This oxygen release could cause the measured pressure pulse, which is particularly important to interpret the cases when the pressure onset is observed before optical emission. Note that the delayed emission pulse cannot be explained by temperature gradients across or along the heated powder. Calculations do indicate a difference in the temporal temperature profiles for particles in the inner and outer coating layers; however, these differences as a function of the heating rate do not follow the trend observed for the delay in experiments.

The curves of constant oxygen consumption in Figure 3.11 do not correlate directly with the trend for the ignition temperatures. The temperature effect is greater

for the constant consumption curves than it is for the ignition temperatures. It suggests that the stability of CuO_{1-x} reduces markedly when x increases. For example, the 3% consumption curve is below the ignition curve at low heating rates (cf. Figure 3.11), suggesting that the respective oxide $\text{CuO}_{0.97}$ was stable at the temperature at which it was formed under those heating conditions. At higher heating rates, this same composition is formed at a higher temperature, closely matching that of ignition. It can be thus suggested that at this higher temperature, $\text{CuO}_{0.97}$ became unstable, resulting in the gas release and ensuing ignition.

The effect of heating rate on the temperature location of the heat flow spike is relatively weak, which is, in fact, quite similar to its effect on the ignition temperature, as is also seen in Figure 3.10.

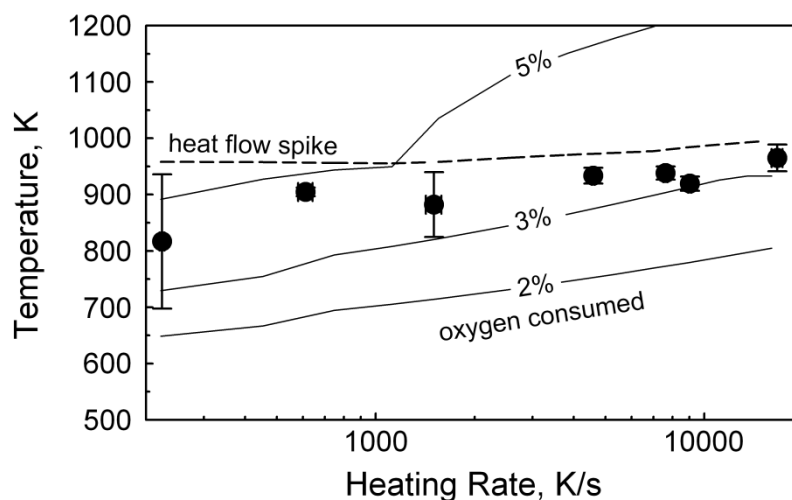


Figure 3.11 Effect of heating rate on the experimental ignition temperature and reference points predicted in calculations. Constant oxygen consumption curves and the trend showing occurrence of a sharp heat flow spike caused by the polymorphic phase change in alumina are calculated for 200-nm CuO inclusions.

3.5 Discussion

Results presented in Figure 3.10 are consistent with previous measurements [31-33, 37], all suggesting that the relatively weak, low-temperature exothermic reactions cannot be neglected when describing ignition of fully dense $2\text{Al}\cdot 3\text{CuO}$ powders at high heating rates. These low-temperature reactions were shown to be well-described by the CM kinetics [31-33]. However, applying the current reaction mechanism based on calorimetric measurements does not result in the temperature runaway, characteristic for ignition. Thus, the effect of concurrent processes, especially pressure release observed upon ignition should be considered.

The pressure increase due to decomposition of CuO, and release of O_2 in the environment can be estimated based on the volume of the reaction chamber, and the amount of powder typically used. Assuming that the material is fully dense, the density of individual particles calculated based on densities of Al and CuO is 5.16 g/cm^3 . Assuming then the packing fraction of 0.5, the mass of the coating used in each experiment can be estimated for a 5-mm long and 90- μm thick layer as $\sim 0.023 \text{ mg}$. This amount contains about $1.2\cdot 10^{-4}$ moles of CuO, which, if fully decomposed would release $0.6\cdot 10^{-4}$ moles of O_2 . In the chamber with a volume of 31 cm^3 , this would generate a pressure increase of up to 15 kPa at the ignition temperatures near 1000 K. This estimate predicts the highest possible pressures discounting cooling of the

expanding gases. Note that higher pressures may be anticipated after ignition, when Cu vapors and gaseous aluminum suboxides can form.

From the experimental data, the pressure at the onset of the emission signal can be determined. The observed trend resembles Figure 3.7, with values averaging around 0.03 kPa at lower heating rates, eventually increasing to an average 0.15 kPa at the highest heating rates. According to the pressure estimate above, this corresponds to a release of approximately 1 % of the oxygen contained in the CuO. In other words, the oxidizer remains largely intact even after the observed gas release, while the released gas is certainly capable of disrupting the heat transfer between powder coating and the filament. In fully-dense nanocomposite powders prepared by ARM, this gas release can also cause particle cracking producing fresh reactive surfaces.

The observed delay of the light emission pulse compared to the pressure pulse (Figure 3.7) at the onset, where full-fledged combustion has not yet occurred, clearly indicates that the initial gas release detected in these experiments is due to CuO decomposition rather than to evaporating Cu. This conclusion is further supported by the low temperatures at which the gas release is occurring, which do not exceed even the melting point of Cu (1378 K). As noted above, CuO decomposition did not occur in reference experiments using the chemically inert $2\text{Cu}\cdot3\text{CuO}$ nanocomposite material. Thus, initial, low-temperature redox reaction occurring in the $2\text{Al}\cdot3\text{CuO}$ prior to the gas release by decomposing CuO is essential in forming a metastable CuO_{1-x} phase, which

releases oxygen much more readily compared to CuO when heated to approximately 1000 K.

This work shows that the present mechanism describing exothermic heterogeneous Al/CuO reaction [31-33] can be considered as also describing formation of the metastable CuO_{1-x} phase. In order to directly model ignition in the present coated filament configuration, an additional mechanism, describing decomposition of that phase as a function of x and temperature must be added. To support development of such a mechanism, additional experiments are necessary, in which the gas release and ignition temperatures are characterized for powders with different sizes of CuO inclusions. The improved model must further describe a change in transport properties of the coating caused by the gas release, e.g., increase in its porosity, which could reduce the efficiency of heat transfer between powder and filament, and thus result in thermal runaway of the reacting powder particles removed from the filament. Such model modifications are particularly important for situations when porosity of the material is an essential parameter, e.g., for ignition of consolidated reactive materials.

3.6 Conclusions

Experiments with fully-dense $2\text{Al}\cdot 3\text{CuO}$ nanocomposite powders prepared by ARM and placed on a metal filament electrically heated in vacuum showed that both optical and pressure pulses accompany onset of combustion. No gas release or optical emission

were observed in similar experiments with reference inert composite powder, in which Al was replaced with Cu. For the reactive composites, the pressure pulse occurred before the optical emission could be detected. The delay between the pressure and emission signals increased at higher heating rates. The results are interpreted proposing that the low-temperature redox reaction described by the Cabrera-Mott kinetics produces a metastable CuO_{1-x} phase which releases oxygen upon heating to approximately 1000 K. Thus, it is shown that despite a relatively small heat release, the low-temperature redox reactions in nanocomposite thermites are important as producing destabilized, partially reduced oxide phases that decompose with a gas release upon heating. In the present experiments, the gas release changed thermal properties of the powder coating reducing the efficiency of its heat exchange with the supporting filament and thus enabling its thermal runaway and ignition.

CHAPTER 4
VALIDATION OF THE THERMAL OXIDATION MODEL
FOR Al·CuO NANOCOMPOSITE POWDER

4.1 Introduction

Nanocomposite thermites represent an interesting class of energetic materials, most notably because of their high energy densities, adiabatic flame temperatures, and reaction rates [5-7]. They have been actively investigated for a wide range of potential applications including propellants, explosives, and pyrotechnics [8, 12]. The development of nanocomposite thermites eliminated significant limitations of traditional micron-sized metal/metal oxide powder mixtures, including low burn rates and long ignition delays [11, 12].

Nanocomposite thermites are composed of a reactive metal, in most cases aluminum, mixed on the nano-scale with a relatively easily reduced metal oxide. The nano-scale mixing results in a highly developed interface area between reactive components. The ignition characteristics of these materials are strongly influenced by these highly developed reactive interfaces, and self-sustaining exothermic reactions begin at much lower temperatures compared to conventional thermite powders [5]. Very high burn rates for nano-thermites have been observed in previous experimental studies [13, 14]. Flame propagation speeds in Al·Fe₂O₃, Al·CuO, and Al·MoO₃ nanocomposite

materials were shown to be on the order of km/s [13], three orders of magnitude faster than the flame speeds observed for traditional thermites [15].

Nanocomposite thermites can be prepared by several techniques, including powder mixing [16-18], sol-gel processing [19-21], self-assembly [22-24], vapor layer deposition [25, 26], and arrested reactive milling (ARM) [27-30]. Depending on the preparation method employed, significant variation in particle sizes, surface morphologies and active metal content may occur, leading to differences in ignition mechanisms. Fully dense nanocomposite powders prepared using ARM have the unique advantage of maintaining high reaction rates associated with nano-scale mixing of reactive components and respective high specific surface area of the reactive interfaces, while offering relative simplicity of handling and mixing, typical for conventional micron-sized powders. Each particle in a nanocomposite powder is fully dense and made of solid phases mixed on the scale of ca. 100 nm or less. Previous results suggest that in ARM-prepared nanocomposites, the components are separated by passivating layers with a thickness of about 0.5 nm, much less than the natural oxide layers formed on surface of air-passivated aluminum [31]. The unique interface morphology is thought to cause the exothermic redox reactions in such materials to begin at lower temperatures compared to other types of nanocomposite thermites [5].

Low temperature exothermic reactions are expected to contribute significantly to the processes that lead to ignition of fully dense nanocomposite thermites [31, 32]. For

aluminum-based compositions, there are multiple reaction steps associated with formation of different polymorphs in the growing alumina layer [33], which are qualitatively similar to the steps observed for aluminum oxidation in gaseous oxidizers [34]. However, recent studies of nano-thermites [35-37] prepared by ARM showed that the onset of low-temperature redox reactions occurred earlier than for Al oxidation with gas oxidizers.

Recent work attributed the accelerated oxidation in nano-thermites at low temperatures to Cabrera-Mott (CM) reaction [9, 31-33, 39, 41], where the growth of very thin alumina layers is accelerated by an electric field induced across such layers. A reaction mechanism including multiple oxidation steps starting with the CM reaction followed by direct oxidative growth of and phase changes in different alumina polymorphs was proposed for a stoichiometric $2\text{Al}\cdot 3\text{CuO}$ nanocomposite powder prepared by ARM [33]. The mechanism specified activation energies and pre-exponents for each step based on matching the calculations with experimental thermo-analytical data for one specific nanocomposite sample. The model predictions are affected by two groups of parameters: those characterizing kinetics of different reaction steps and those affected by the assumed structure and morphology of the nanocomposite powder. The latter material characteristics may need to be altered for the powders prepared using different procedures. Nevertheless, the kinetics represented by the activation energies and pre-exponents describing different steps of the Al-CuO reaction are expected to

remain valid for reactive materials with different scales of mixing, interface morphologies, and component ratios, as long as the components remain Al and CuO. In this work, the objective is to establish whether the kinetic model stays valid and can describe reactions in nano-composite materials with the same reagents, prepared using different conditions and thus having different mixing morphology, and, possibly stoichiometry compared to the initial samples for which the kinetics was derived.

4.2 Experimental Techniques

4.2.1 Materials Synthesis

Four nanocomposite powders with the same starting composition of $2\text{Al}\cdot 3\text{CuO}$ were prepared by ARM using different milling times [27]. The starting material was a blend of aluminum and copper oxide powders. Aluminum powder (-325 mesh) of purity 99.5% was provided by Atlantic Equipment Engineers. Copper oxide powder from Sigma-Aldrich (25 μm) with 99+% purity was used. A Retsch PM 400MA planetary mill, in which the milling compartment was additionally cooled using an air conditioner, was used to prepare composite powders. Four different composite powders were prepared by milling the blended starting materials in hexane and under argon environment for 30, 40, 60 and 80 minutes, respectively. Milling times longer than 80 min were not considered because of an undesirable substantial reaction between Al and CuO during milling. Custom-built 150-mL milling vials were used, designed to withstand the temperatures

and pressures of accidental mechanical initiation of the thermite reaction. Each milling vial was loaded with 30 g of powder, with ball to powder mass ratio of 3. Hexane (24 mL) was added in each vial. Additional details on the milling procedure and parameters can be found elsewhere [56].

4.2.2 Materials Characterization

Powder morphology and elemental composition were examined using a LEO1530 Field Emission scanning electron microscope (SEM), equipped with an energy dispersive X-ray spectrometer (EDX). Samples were embedded in epoxy and cross-sectioned for analysis. Images were taken using backscattered electron imaging. Phase compositions of the samples were analyzed using X-ray diffraction (XRD) on a PANalytical Empyrean multi-purpose research diffractometer.

Particle size distributions of the prepared materials were measured with low-angle laser light scattering using a Beckman-Coulter LS230 Enhanced Particle Analyzer. Powder suspensions for analysis were prepared in distilled water and ultra-sonicated to minimize particle agglomeration. Note that prepared powders could have reacted with water; however, it was observed that at room temperature such reactions were only initiated after an extended (about 3 days) exposure [4]. No reactions with distilled water were detected in the present experiments, each size distribution measurement taking less than 15 min.

Differential scanning calorimetry (DSC) was carried out at 2, 5 and 10 K/min using a Netzsch Simultaneous Thermal Analyzer STA409 PG. Prior to experiments, powders were dried in vacuum overnight to remove residual hexane. Samples were heated in argon with a flow-rate of approximately 50mL/min in alumina pans and the methodology described by [37] was followed. Heat release was also studied using a microcalorimeter TAM III by TA instruments under isothermal conditions at different temperatures in the range from 303 to 413 K. A sample mass of 150 ± 30 mg was used for each experiment carried out for a minimum of 24 hours. Measurements could be directly interpreted as heat release from the thermite reaction only after the sample thermally equilibrated in the calorimeter. Further details of experimental methodology can be found elsewhere [31].

4.2.3 Reaction Model Summary and Validation Approach

A multi-step reaction kinetics model was recently developed for fully dense 2Al-3CuO nanocomposite [31, 33], where redox reaction, $2\text{Al} + 3\text{CuO} \rightarrow \text{Al}_2\text{O}_3 + 3\text{Cu}$, is assumed to occur. This model describes an increase in the thickness, h , of the Al_2O_3 layer growing between Al and CuO. The diffusion resistance of this layer changes, which affects the rate of the exothermic reaction leading to ignition. The changes in diffusion resistance occur because of an increased thickness and because of the polymorphic phase transformations in alumina. The model assumes that uniformly sized, spherical CuO inclusions are embedded into the Al matrix, as shown in Figure 4.1 [33].

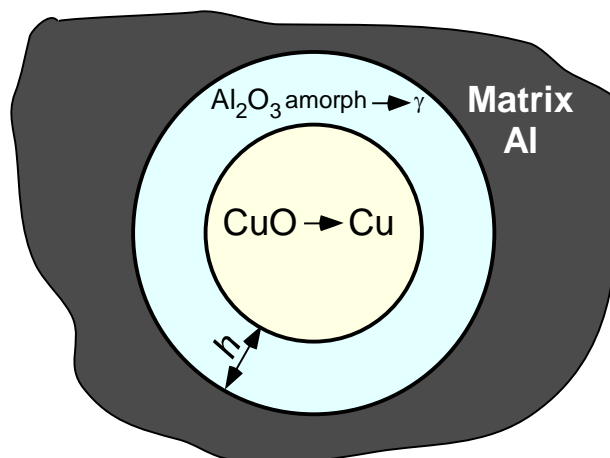


Figure 4.1 Schematic diagram of the composite material described in the reaction model.

Assumptions of both uniform inclusion sizes and their spherical shapes represent substantial simplifications of the true inclusion morphology illustrated in Figures 4.2 (inclusion shapes visible in images B) and 4.3. Initially, each inclusion is assumed to be surrounded by a very thin amorphous aluminum oxide layer. Its initial thickness is specified based on processing TAM III experiments [31]. The reaction is assumed to be fully controlled by transport of reactive species through the growing Al_2O_3 layer. The size of CuO inclusions (transforming into Cu) is decreasing as the reaction occurs.

Specific reaction stages characterized by individually described reaction rates include:

- 1) Initial growth of amorphous alumina, described using the CM mechanism [31]. The CM reaction rate decreases as the oxide thickness increases.
- 2) Growth of amorphous alumina due to regular thermal diffusion. This process occurs simultaneously with the previous one, but it becomes more important as both the thickness of the oxide layer and temperature increase.

- 3) Transformation of the amorphous alumina into the γ -Al₂O₃ polymorph. During this phase change, the thickness of the remaining amorphous alumina decreases, which could result in a short-time acceleration of the CM reaction.
- 4) Growth of γ -Al₂O₃ polymorph by thermal diffusion.

Additional processes, including a phase change to α -Al₂O₃ and its growth are neglected because they typically occur at relatively high temperatures and are expected to be irrelevant for the reactions leading to ignition in nano-thermites.

The total heat flow measured in DSC or TAM III experiments is expressed as:

$$\dot{Q} = \chi \Delta H \sum_i \frac{dm_i}{dt} \quad (4.1)$$

Where terms dm_i/dt express rates of mass increase for alumina polymorphs, with the summation index i representing both amorphous and γ -Al₂O₃, ΔH is the reaction enthalpy based on the stoichiometric redox reaction and taken as a function of temperature [71], and χ is the number of inclusions per unit mass in the nanocomposite particle, representative of the sample composition. For each alumina polymorph, the model includes a reaction kinetics expression, which can be generally written as:

$$\frac{dm_i}{dt} = \pi d^2 \sum_j K_j \quad (4.2)$$

Where d is the inclusion diameter, index j numbers various reaction steps, and K_j stands for specific expressions for reaction kinetics of different reaction steps, including

respective activation energies, pre-exponents, and other pertinent parameters specified by [31]. Reaction kinetics models (expressions for individual K_j terms), were identified based on experiments with a single batch of the stoichiometric $2\text{Al}\cdot 3\text{CuO}$ prepared by a 60-min milling [56]. For that material batch, based on the sample analysis, the parameters d and χ were correspondingly identified as 100 nm and $3.1\cdot 10^{13} \text{ kg}^{-1}$. This combination of d and χ represented the sample composition of $2.7\text{Al}\cdot 3\text{CuO}$, which agreed with the analyses of prepared composite particles. Because the starting composition was $2\text{Al}\cdot 3\text{CuO}$, the powder included excess of CuO, present as individual, unattached CuO particles. The number of such unattached particles is expected to decrease with increased milling time. Respectively, at longer milling times, the composition of the prepared composite is expected to approach the starting composition more closely.

The approach taken in this study is to validate the present model considering experiments performed with materials with the nominal composition of $2\text{Al}\cdot 3\text{CuO}$ (determined by the ratio of the starting Al and CuO powders) prepared using different milling conditions. If the model is valid, descriptions of reaction kinetics, i.e., expressions for K_i , in Eq. (4.2) should remain the same as in [31], while changes in the sample morphology can be reasonably represented by the properly adjusted values of d and χ . Further, the appropriate values of d and χ can be also determined from

independent sample analyses and should match the values required for Equations (4.1) and (4.2) to describe the experiments.

4.3 Experimental

4.3.1 Particle Sizes and Morphology

Figure 4.2 shows SEM images of the cross-sections of the four nanocomposite powders with the nominal composition of $2\text{Al}\cdot 3\text{CuO}$ milled for 30, 40, 60 and 80 minutes. All images were taken using backscattered electrons to highlight phase contrast between the dark epoxy background, gray Al matrix and light areas rich in CuO. The images on the left 1-4(A) were taken at a low magnification in order to observe particle size, morphology and degree of mixing. Images on the right 1-4(B) were taken at a higher magnification for more details on inclusion size and morphology.

The SEM images revealed irregularly shaped particles, mostly sized in the range of 10–30 μm . Poorly mixed particles of almost pure Al and CuO were present, amongst the well mixed Al-CuO nanocomposite particles. The images show an increased homogeneity and improved mixing for the samples prepared with longer milling times. The number of unmixed particles for both Al and CuO reduces visibly as the milling time is increasing from 30 to 80 min.

Inclusion size distributions were obtained processing several high magnification images for each sample. The characteristic dimensions of the copper oxide inclusions are

typically in the submicron size range. The images were thresholded as shown in Figure 4.3, so that each CuO inclusion that appears brighter than Al or epoxy could be recognized as an individual object and then sized classified. The smallest detected inclusion was defined as an object including at least four pixels, corresponding to approximately 20 nm considering the magnification used.

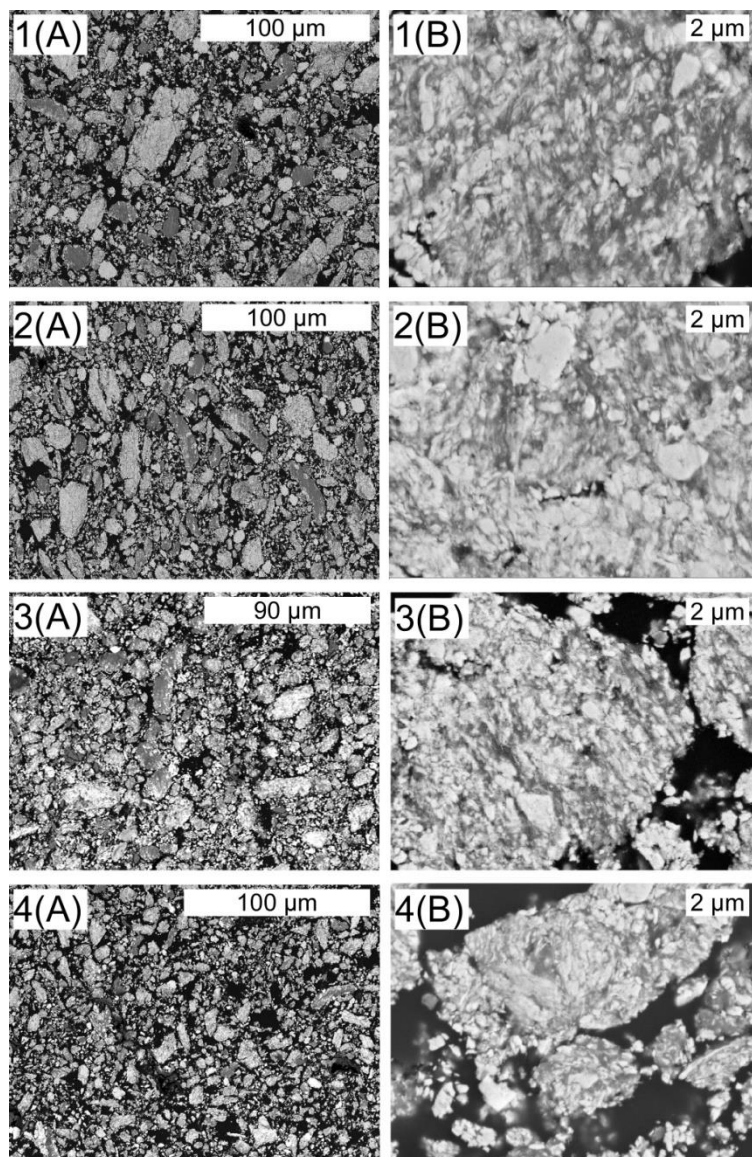


Figure 4.2 Backscattered electron SEM images of cross-sectioned and embedded in epoxy nanocomposite powders with the nominal composition of $2\text{Al}\cdot 3\text{CuO}$ prepared using different milling times: 1(A, B): 30min; 2(A, B): 40min; 3(A, B): 60min; 4(A, B): 80min.

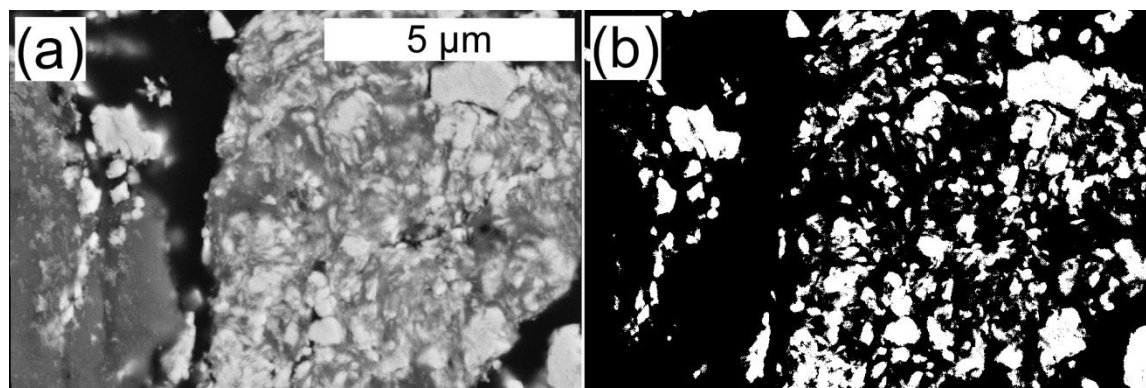


Figure 4.3 SEM images showing (a) cross-sectioned sample and (b) thresholded image with white areas indicating CuO inclusions used for the inclusion size analysis.

Image processing was carried out using UTHSCSA Image Tool version 3.0. The Feret diameter (defined as the square root of the inclusion area divided by π) was used as a representative dimension for each inclusion. Each size distribution was derived from at least 1000 inclusions. Obtained size distributions are shown in Figure 4.4. Inclusions for all samples remain in a size range of ca. 30-1000 nm and size distributions peak around 130 nm for all samples. CuO domains with sizes less than 100 nm were observed in samples milled for 30 and 40 minutes, but could not be detected in the samples milled longer. Upon closer examination of the processed SEM images, such domains were found to be mainly unattached CuO particles that were not incorporated into the Al matrix. Note that presence of the fine unattached particles skews the average particle sizes shown in Figure 4.4. Instead of such averages, the size distribution peak positions and overall shapes should be used to compare inclusion dimensions for different prepared composite powders.

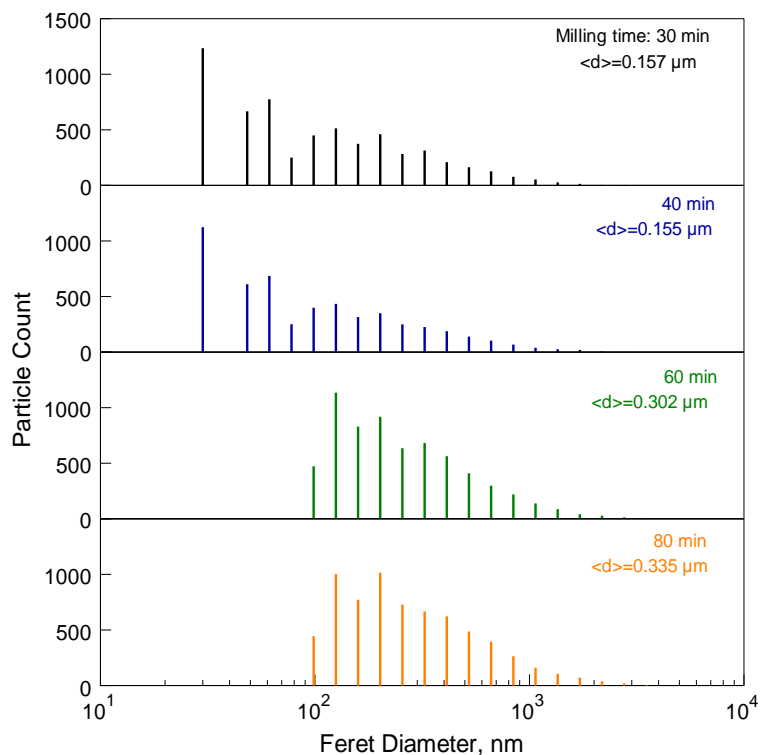


Figure 4.4 Size distributions of copper oxide inclusions determined from SEM images of nanocomposite powders with the nominal composition of $2\text{Al}\cdot 3\text{CuO}$ prepared using different milling times.

Particle size distributions for the prepared powders are shown in Figure 4.5. The volumetric mean particle sizes, 9.5, 11.0, 9.8 and 8.6 μm for the samples milled for 30, 40, 60 and 80 min., respectively are close to one another; these sizes are in agreement with those observed in SEM images. Thus, both SEM examination and particle size analysis for the prepared materials suggest that milling for longer times does not result in significant changes in the average particle size or particle size distribution.

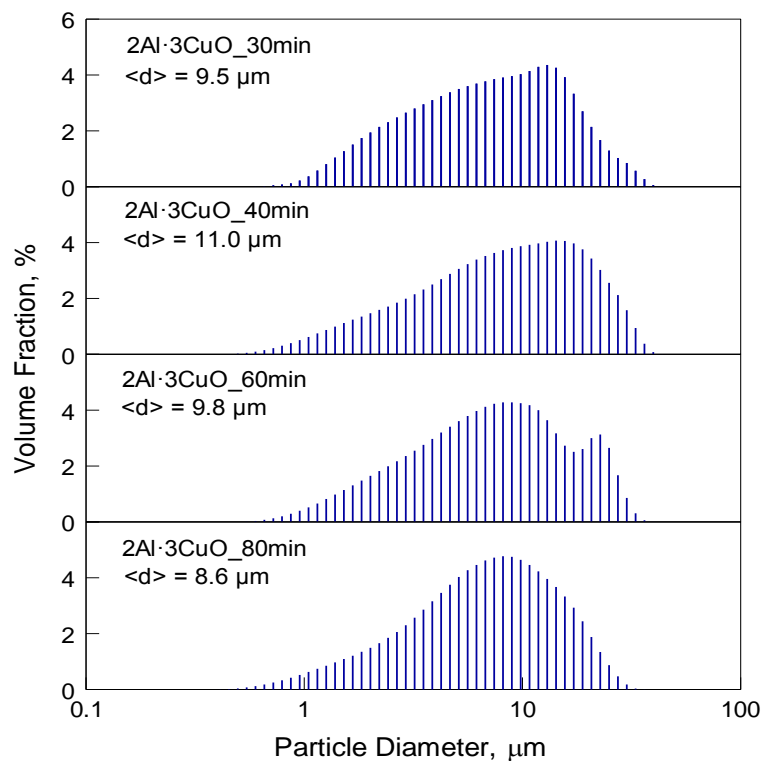


Figure 4.5 Particle size distributions of nanocomposite powders with the nominal composition of $2\text{Al}\cdot 3\text{CuO}$ prepared using different milling times.

4.3.2 Phase Identification

Characteristic XRD patterns collected for the four samples prepared with varying milling times are shown in Figure 4.6. Scans with the angle range of $30\text{-}50^\circ$ are shown with the vertical scale selected so that the strongest Al and CuO peaks present in all samples are cut, while smaller peaks are emphasized. The observed peaks were generally similar for each sample except for the angle range of $43\text{-}45^\circ$, where peaks for Cu, Cu_2O , and Cu_9Al_4 were observed. These peaks were detected for samples milled for 60 and 80 minutes. In addition, γ -alumina peaks were found in all samples. No detectable broadening of CuO peaks was observed, indicative of unchanged CuO crystallite sizes for powders prepared

using different milling times. This is in agreement with the inclusion size analysis (cf. Figure 4.4) that suggests that the same range of CuO inclusion sizes was present in all prepared samples.

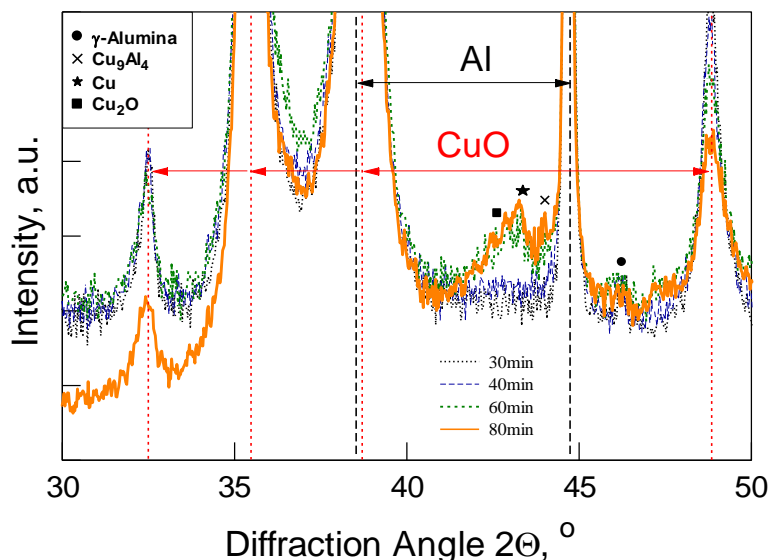


Figure 4.6 XRD patterns of nanocomposite powders with the nominal composition of 2Al·3CuO prepared using different milling times.

4.3.3 Composition Analysis

Prior to milling, stoichiometric proportions of Al and CuO were loaded into the planetary mill. However, based on milling time, variation has occurred in both degree of mixing and final composition of the nanocomposite particles produced. More specifically, as shown in Figure 4.2, some of the CuO particles remain separated from Al, so that the prepared composite particles contain a greater Al/CuO ratio than the starting powder blend. This effect diminishes with increased milling times. To quantify this effect, an approach based on processing composition-sensitive SEM images collected with backscattered electrons

was used. Images used to characterize each individual prepared material were collected at the same SEM setting, including extra high tension voltage of 10 kV and working distance of 8-10 mm. Although working distance varied slightly from sample to sample due to difference in height of the sample holders, it was held fixed for each individual sample. The methodology used is illustrated in Figure 4.7 and Table 4.1. Figure 4.7 shows a typical SEM image. There are poorly mixed and well mixed portions observed in the cross-section; Al-rich regions are dark gray while CuO-rich regions are white in appearance. The brightness of the nanocomposite regions where Al and CuO are mixed falls in between these two extremes. To calibrate the brightness in terms of composition, several parts within an image were selected as shown in Figure 4.7, and their respective Energy-Dispersive X-ray (EDX) spectra were collected and interpreted using standard-free analysis. The results are shown in Table 4.1, indicating the molar ratios of Al, Cu and O for each case.

To obtain the image brightness calibration for each sample, three images for each of the four different milled samples were analyzed and the corresponding EDX implied compositions were quantified for multiple selected areas in each image. Five to ten areas were selected in each image covering the entire range of compositions (and respective range of brightness levels), going from relatively pure Al to pure CuO. The average brightness values of the same selected areas were determined. Calibrations between average brightness and average composition for each sample are shown in Figure 4.8. For

each sample, brightness was fitted to composition using a straight line; the obtained fits were used to quantify the compositions of multiple composite particles based on the average brightness of SEM images of their cross-sections.

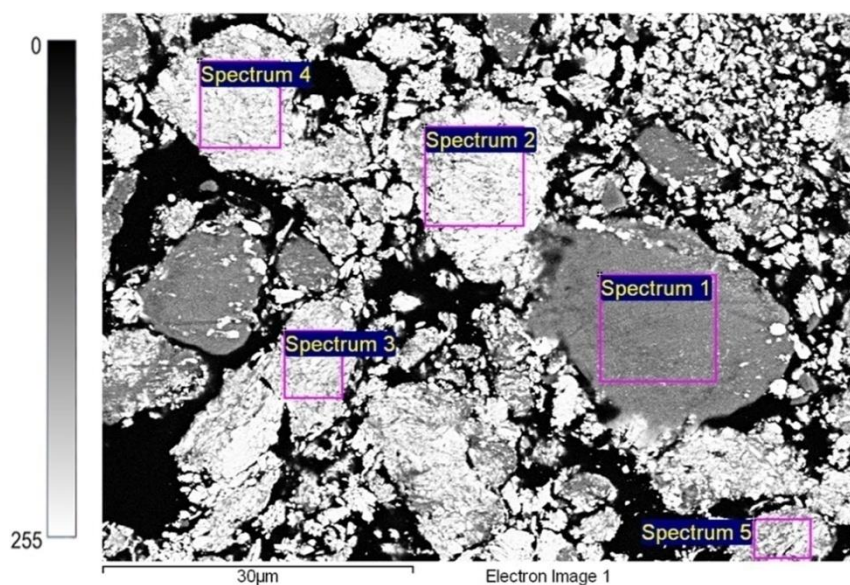


Figure 4.7 An example SEM image identifying areas for EDX composition analysis used for calibration of composition with brightness (This sample was prepared using 30-min milling time).

Table 4.1 Normalized Compositions of the Areas Shown in Figure 4.7 in Atomic %, Determined by Standard-free EDX Analysis

Spectrum	O	Al	Cu
1	8.47	91.12	0.41
2	42.56	21.42	36.02
3	38.14	32.49	29.37
4	40.04	27.20	32.77
5	34.21	41.80	23.99

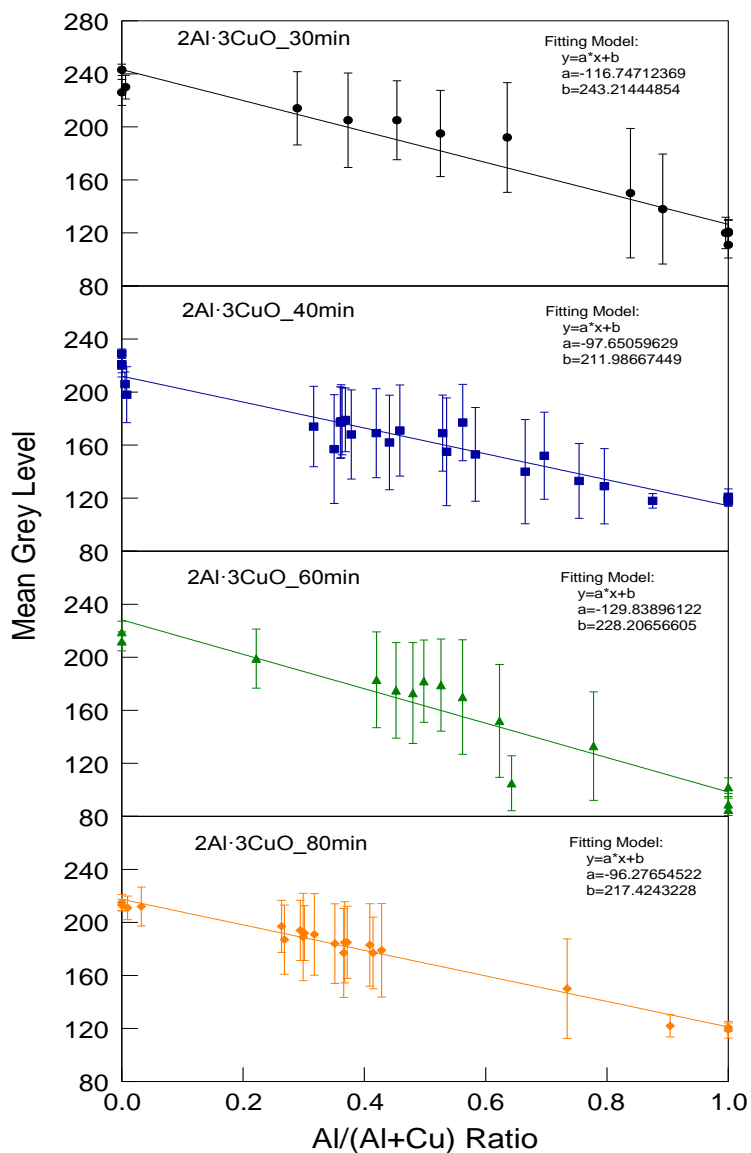


Figure 4.8 Calibration of composition with brightness for nanocomposite powders with the nominal composition of 2Al·3CuO prepared using different milling times.

With the image brightness calibration available, average compositions for individual composite particles were obtained for each of the prepared materials. Particle size was also measured for each analyzed particle to determine whether the particle composition is a function of its size. Because all composite particles were brighter in

color than the background epoxy, their low-magnification SEM images were thresholded by brightness to identify particles, as illustrated in Figure 4.9. Image shows all individual particles being thresholded. Image analysis yielded both Feret diameter and average brightness for each object-particle. The brightness was converted to composition using the calibrations shown in Figure 4.8. Three to five images of each of the four samples were analyzed. Particle size range between 200 nm and 20 μm was broken down into seven logarithmically spaced bins and average compositions for particles in each bin size were determined. The results are shown in Figure 4.10. Particles with sizes $<1 \mu\text{m}$ appear to be generally darker. Closer examination of images used for brightness calibration did not show that such particles are aluminum-rich; instead, it was concluded that for such small particles, the average brightness measurement was skewed by dark surroundings. Higher resolution images would be required to properly identify their composition; however, their mass fraction in the sample was relatively low and such additional measurements were not warranted.

Compositions for particles with sizes $>10 \mu\text{m}$ vary; such large particles likely represent an unmixed or poorly mixed portion of material. These particles are not expected to contribute significantly to low temperature reactions. The size range between 1-10 μm is likely to encompass the bulk of the nanocomposite powder (cf. Figure 4.5). The compositions for particles in this size range do not change substantially for each powder. A systematic composition shift is observed in Figure 4.10 for powders milled using

different times. The composition of the prepared composites approaches that of the initial blend of starting materials as the milling time increases.

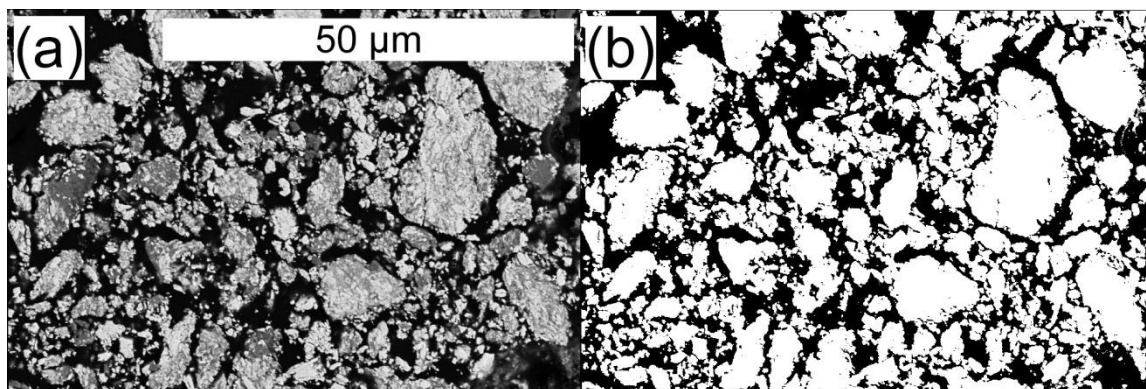


Figure 4.9 SEM images showing (a) cross-sectioned sample and (b) thresholded image with light areas indicating whole particles used in average composition analysis.

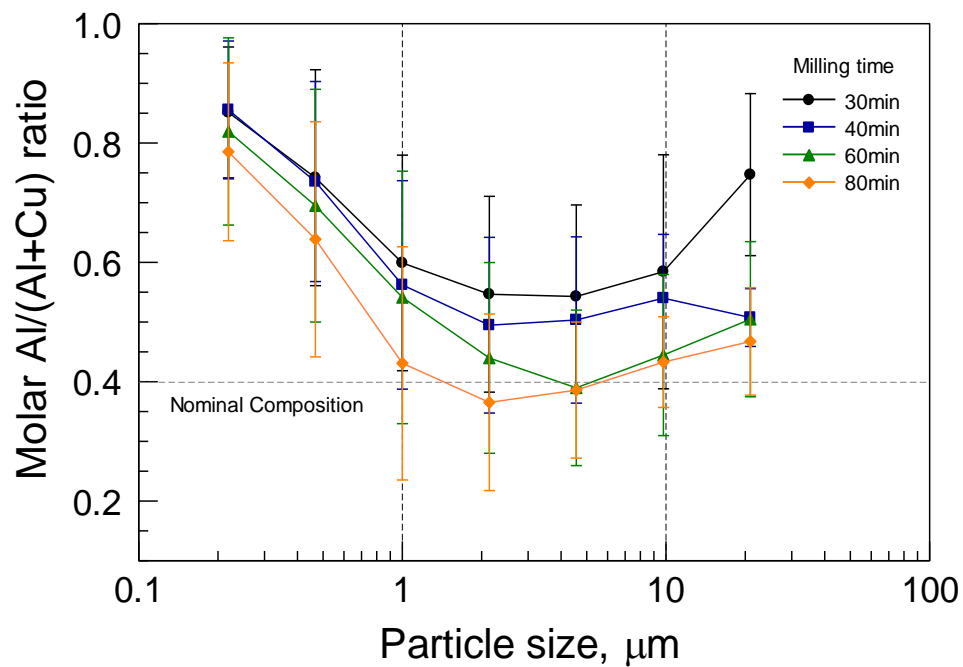


Figure 4.10 Average composition for different size fractions of nanocomposite powders with the nominal composition of 2Al-3CuO prepared using different milling times.

Note that analysis presented in Figure 4.10 does not account for the intermediate phases, such as Cu_2O , and Cu_9Al_4 . Amounts of such phases are expected to be relatively small based on their weak XRD signatures (Figure 4.6). Based on SEM imaging, it was observed that such phases formed locally and were present in some particles, whereas most of the powder remained unreacted.

4.3.4 Thermal Analysis

Figure 4.11 shows heat flows for all samples in the temperature range of 350-650 K where low-temperature reactions are expected to be significant. For greater accuracy of these measurements, the mass of material loaded in the DSC sample holder was increased to ca. ~30 mg. The maximum temperature was limited to 650 K for safety (to prevent the sample ignition). The traces shown were baseline-corrected by subtracting the signal recorded during the second heating of the same sample. A clear difference in DSC traces for samples prepared using different milling times is observed. Samples become more reactive, showing stronger exothermic rise and plateau at the higher heat flow when milling times increase. Following the present model, the initial rise in the DSC signals between ca. 350 and 450 K is interpreted as heat released in a relatively weak exothermic event, when the initially thin amorphous layer grows according to the CM kinetics. This is followed by a plateau while the thickness of the amorphous oxide increases and the CM reaction becomes less significant.

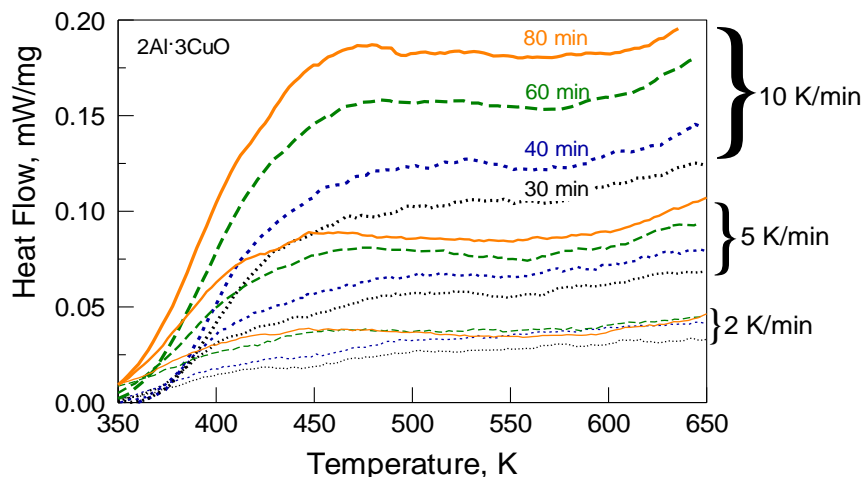


Figure 4.11 Experimental DSC curves for nanocomposite powders with the nominal composition of 2Al-3CuO prepared using different milling times.

TAM III measurements for each sample at different temperatures in the range of 323-403 K are shown in Figure 4.12. The rate of heat release is normalized by sample mass and the results are shown after the TAM III signal became free of heat flow disturbances, i.e., 60 minutes after the sample was exposed to the bath temperature. The results indicate an expected increase in reaction rate with temperature. It is also observed that for each temperature, the reaction rate increases for samples prepared using longer milling times. The measured heat flow curves decay in time monotonically for both 323 and 363 K. For 403 K, additional features are observed at extended exposure times, likely indicative of new reaction stages for relatively high overall progress of the redox reaction. Such high reaction progress processes are outside the scope of the present work.

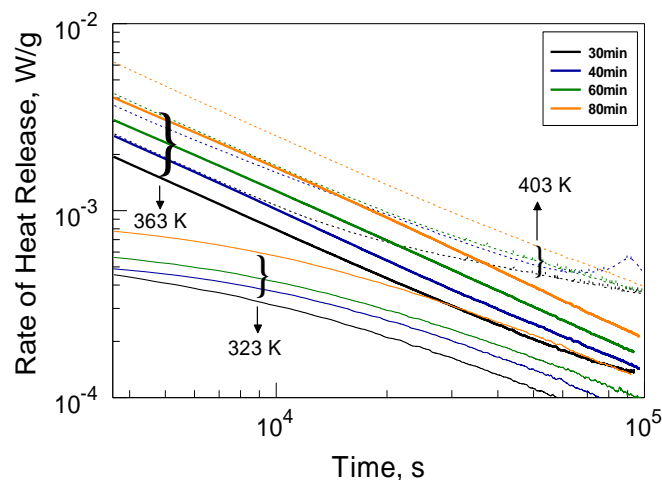


Figure 4.12 Experimental TAM curves for nanocomposite powders with the nominal composition of 2Al·3CuO prepared using different milling times.

4.4 Model Validation

Previously, a multistep kinetic model for reaction in the Al/CuO composites was proposed based on experiments with a sample with the nominal composition 2Al·3CuO milled for 60 min [31, 33]. In this work, a similar sample was prepared in addition to three more Al/CuO composite samples. In these additional samples, the balance between initial Al and CuO powders was maintained while different milling times were employed (30, 40 and 80 min). According to Equations (4.1) and (4.2), the heat flow in both DSC and TAM III experiments is sensitive to the specific kinetic models used, K_j , as well as to the size of CuO inclusions, d , and to their number per unit mass of the composite particle, χ .

Variation in milling time was expected to have an impact on the sample morphology, which is represented in model by parameters d and χ . However, the

description of K_j should remain the same as long as the same reactants are present. Thus, the reaction kinetics model can be validated if changes in the values of d and χ , supported by the sample characterization, can account for observed differences between DSC and TAM III traces observed for different samples, as shown in Figures 4.11 and 4.12.

The parameters d and χ were treated as adjustable parameters while kinetic models K_j were used according to Equations (4.1) and (4.2) [31, 33] to match the experimental data shown in Figure 4.11. The results of this analysis are shown in Figure 4.13. For the 60-min sample, the initial values of d and χ gave a good match with the experimental data, suggesting reproducibility in the materials characteristics. For other samples, predictions using initial values of d and χ did not result in matching the experiments and the parameters were adjusted.

It was first observed that matching the experimental DSC traces at different heating rates simultaneously for each sample was unachievable by adjusting the inclusion size d only. This result was not surprising because experimentally the inclusion sizes were shown not to change significantly from sample to sample, and a 100 nm inclusion size used in the initial model offered a reasonable approximation for all prepared samples (cf. Figure 4.4). Thus, the value of d remained fixed at 100 nm and parameter χ was adjusted. Simultaneously matching experimental DSC curves at all heating rates for the samples milled for 30, 40 and 80-min was possible by adjusting χ and finding its

corresponding value for each sample. These results are shown in Figure 4.13 and a summary of the resulting values for χ , respective Al/(Al+CuO) ratios and compositions for the nanocomposite powders are shown in Table 4.2. The match between the predicted and measured curves is satisfactory and the results suggest (in qualitative agreement with data shown in Figure 4.10) that the composition and not inclusion sizes are being affected by changing milling time.

A discrepancy between the calculations and experiments at low temperatures, especially noticeable for the samples prepared using longer milling times, is likely associated with an error in identifying the initial thickness of the Al₂O₃ layer separating Al and CuO. The samples prepared with longer milling times are more sensitive to this error because of a better mixing between Al and CuO and thus a greater overall Al₂O₃ surface area. At higher temperatures, the thickness of the Al₂O₃ exceeds significantly its initial thickness, and thus the effect of the initial thickness on the predicted heat flow diminishes.

A quantitative comparison of the sample compositions described in terms of Al/(Al+CuO) ratios obtained as adjustable parameters required to fit the experimental DSC traces, and those implied by the sample SEM/EDX analyses are shown in Figure 4.14. The composition averaged among particles with sizes in the range 1-10 μm (cf. Figures 4.5, 4.10), considered to represent the bulk of the nanocomposite powder for each sample, is shown in Figure 4.14. Consistently with Figure 4.10, it is observed that

longer milling times result in a better mixing, so that the final composition approaches the starting bulk composition of the powder blend. The average composition value from SEM/EDX analysis for the 80-min sample is even slightly lower than the nominal stoichiometric composition. However, the discrepancy is small and within the error bar, implied by scatter in the measurements. As shown in Figure 4.8, the composition/brightness calibration is also determined with some error, which should be taken into account for more detailed comparisons. Generally, Figure 4.14 suggests that SEM/EDX analysis supports the DSC model-implied composition changes for samples prepared with different milling times. Comparison of results shown in Figure 4.13, Table 4.2 and Figure 4.14 suggests that the reaction model described in Reference [33] is validated.

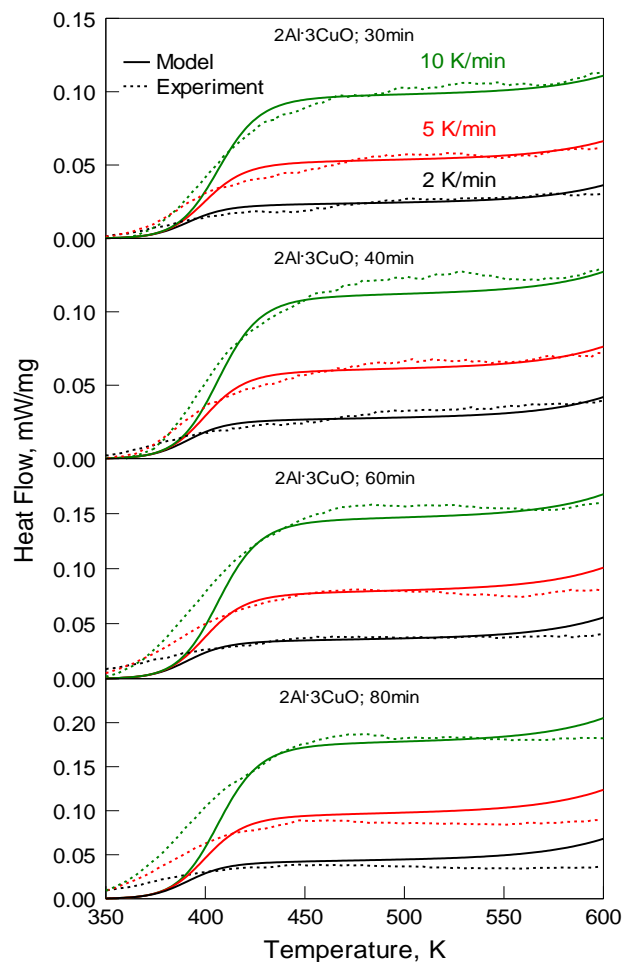


Figure 4.13 Experimental and model DSC curves for nanocomposite powders with the nominal composition of 2Al-3CuO prepared using different milling times.

Table 4.2 Sample Compositions and Numbers of Inclusion per Unit Mass Based on Model

Milling Time (min)	$\chi(\text{kg}^{-1})$	Al/(Al+Cu) Ratio	Effective Composition
30	1.5×10^{13}	0.57	4Al-3CuO
40	1.8×10^{13}	0.54	3.5Al-3CuO
60	2.3×10^{13}	0.47	2.7Al-3CuO
80	2.8×10^{13}	0.42	2.2Al-3CuO

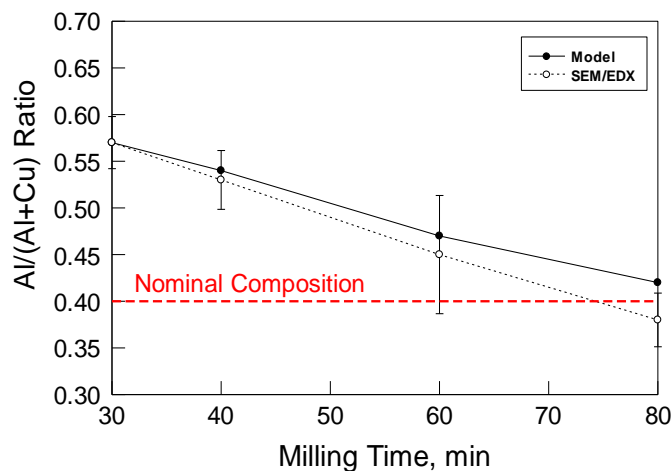


Figure 4.14 SEM/EDX analysis supported and model-implied composition changes for nanocomposite powders with the nominal composition of $2\text{Al}\cdot 3\text{CuO}$ prepared using different milling times.

In order to assess the accuracy of the present validated model for describing the low-temperature reactions detectable by TAM III measurements, the model was used to calculate the heat flow curves corresponding to the experiments shown in Figure 4.12. Values of χ reported in Table 4.2 were used for different samples. The measured and calculated heat flow curves are shown in Figure 4.15. Note that for TAM III experiments, two additional factors affect the results significantly. First, aging of a freshly prepared sample for a few days may lead to an appreciable change in the early reaction rates. This effect is accounted for by the reaction model, considering the samples exposed to room temperature for a period between their preparation and the actual TAM III experiments. Second, the sample is actively reacting during the initial one-hour period while it is thermally equilibrating within the calorimeter. The reaction during this time is difficult to predict theoretically because the sample temperature is

changing in a poorly quantified fashion. This second effect is not accounted for in the present calculations. In all cases shown in Figure 4.15, the model over-predicts the heat release compared to that seen experimentally. The difference between the model and experiment is rather consistent and is likely explained by the lack of an accurate account for the sample reaction during its equilibration in the calorimeter. Considering that it is possible to “tune” the model by introducing appropriate aging for each of the samples to match the experimental curves better, the match between the predicted and measured heat flow trends was considered to be acceptable.

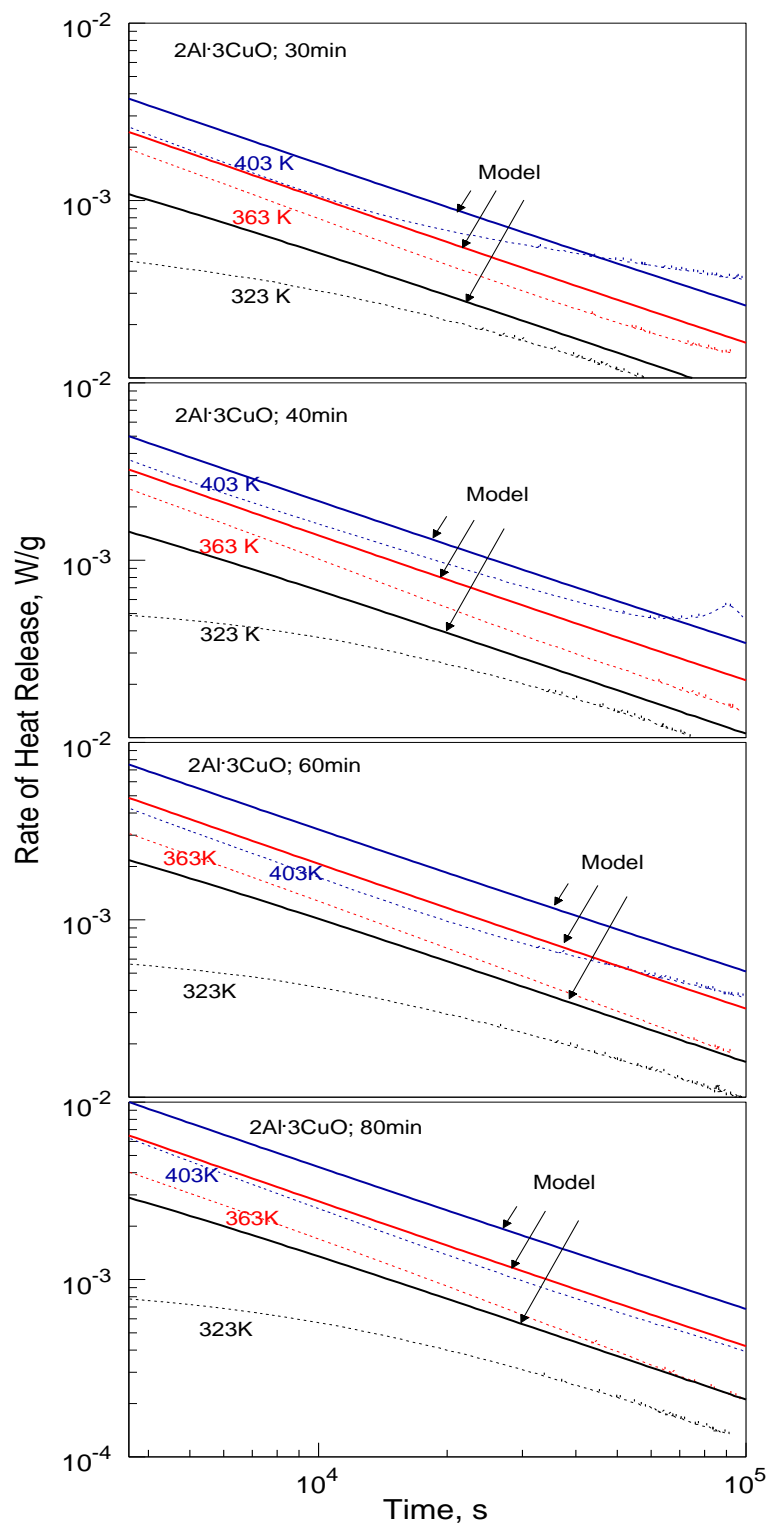


Figure 4.15 Experimental and calculated TAM III curves for the nanocomposite 2Al·3CuO powders prepared with different milling times.

4.5 Conclusions

The experiments showed that in the nanocomposite Al·CuO powders prepared by ARM, the CuO inclusion size remains nearly unchanged at different milling times. It is also observed that the mixing between Al and CuO in the nanocomposite particles enhances as the milling time gets longer, approaching the nominal composition implied by the balance of the starting Al and CuO powders. The nanocomposite powders prepared with shorter milling times are typically rich in Al, and the balance of CuO is present as fine unattached particles mixed with the composite material.

The description of reaction kinetics for the Al·CuO nanocomposite powders using a multistep model developed by Reference [33] remains valid for powders prepared with different milling conditions and, therefore, characterized by different Al/CuO ratios within the composite material. To describe quantitatively the rate of redox reactions in specific nanocomposite powders, the model must use the appropriate size of CuO inclusions as well the number of inclusions per unit of mass in the nanocomposite particle.

The TAM III measurements for redox reactions in nanocomposite thermites are strongly affected by the sample aging occurring during its thermal equilibration in the calorimeter.

CHAPTER 5
LOW-TEMPERATURE EXOTHERMIC REACTIONS IN FULLY-DENSE
Al/MoO₃ NANOCOMPOSITE POWDERS

5.1 Introduction

Nanocomposite thermites are composed of a reactive metal, in most cases aluminum, mixed on the nano-scale with a relatively easily reduced metal oxide. The nano-scale mixing results in a highly developed interface area between reactive components. The high interface area assures a high reaction rate, attractive for many applications. Over the years, nanocomposite thermites have been actively investigated for a wide range of potential applications including propellants, explosives, and pyrotechnics [8, 72, 73]. This work considers fully dense nanocomposite powders prepared using arrested reactive milling (ARM) [5, 27, 29]. Such powders are characterized by high reaction rates associated with nano-scale mixing of reactive components and respective high specific surface area of the reactive interfaces, while offering relative simplicity of handling and mixing, typical for conventional micron-sized powders. The unique interface morphology is thought to cause the exothermic redox reactions in such materials to begin at lower temperatures compared to other types of nanocomposite thermites.

Low temperature exothermic reactions are expected to contribute significantly to the processes that lead to ignition in fully dense nanocomposite thermites [31, 32, 40, 41]. For aluminum-based compositions, there are multiple reaction steps associated with

formation of different polymorphs in the growing alumina layer [33, 42], which are qualitatively similar to the steps observed for aluminum oxidation in gaseous oxidizers [34]. Recent work attributed the accelerated oxidation in the ARM-prepared nano-thermites at low temperatures to the Cabrera-Mott (CM) mechanism [31, 32], where the growth of very thin oxide layers is accelerated by an electric field induced across such layers. A reaction mechanism including multiple oxidation steps starting with the CM reaction followed by direct oxidative growth of and phase changes in different alumina polymorphs was developed for a stoichiometric $2\text{Al}\cdot 3\text{CuO}$ nanocomposite powder prepared by ARM [33]. The reaction kinetics describing these reaction steps were shown to remain valid for the ARM-prepared reactive composites with different scales of mixing, interface morphologies, and component ratios, as long as the components remained Al and CuO [42].

This work is aimed to establish whether the same multistep model can be adapted to describe reaction in another ARM-prepared thermite system, where aluminum is oxidized by molybdenum trioxide, MoO_3 .

5.2 Experimental

5.2.1 Materials

The nanocomposite powder used in this work, metal-rich thermite $8\text{Al}\cdot\text{MoO}_3$ produced by ARM, has been used in several recent studies focused on its ignition and combustion

[36, 40, 64]. It was prepared using an aluminum powder, -325 mesh, 99.5% purity by Atlantic Equipment Engineers and molybdenum oxide powder, -325 mesh, 99.95% purity by Alfa Aesar. The starting powders were blended and milled in hexane under argon for 30 min using a Retsch PM 400MA planetary mill. Additional details characterizing the milling procedure and parameters are similar to those reported elsewhere [56]. The age of the prepared powders was tracked with an accuracy of hours, from the time they were recovered from the ball mill. This tracking was necessary to account for the effect of slow redox reactions occurring during the powder aging and resulting in changing properties of the interface separating Al from MoO_3 inside the composite particles. While undetectable by electron microscopy, such changes were observed in preliminary experiments to affect calorimetric measurements discussed below.

Powder morphology and elemental composition were examined using a LEO1530 Field Emission scanning electron microscope (SEM), equipped with an energy dispersive X-ray spectrometer (EDX). The sample was embedded in epoxy and cross-sectioned for analysis. Figure 5.1 shows SEM images of cross-sections of the prepared $8\text{Al}\cdot\text{MoO}_3$ nanocomposite powder. The images were captured using backscattered electrons to highlight phase contrast between the dark epoxy background, gray Al matrix and light areas rich in MoO_3 . The image on the left was taken at a low magnification in order to observe particle size, morphology and degree of mixing. The image on the right was taken at a higher magnification for more details on inclusion size and morphology.

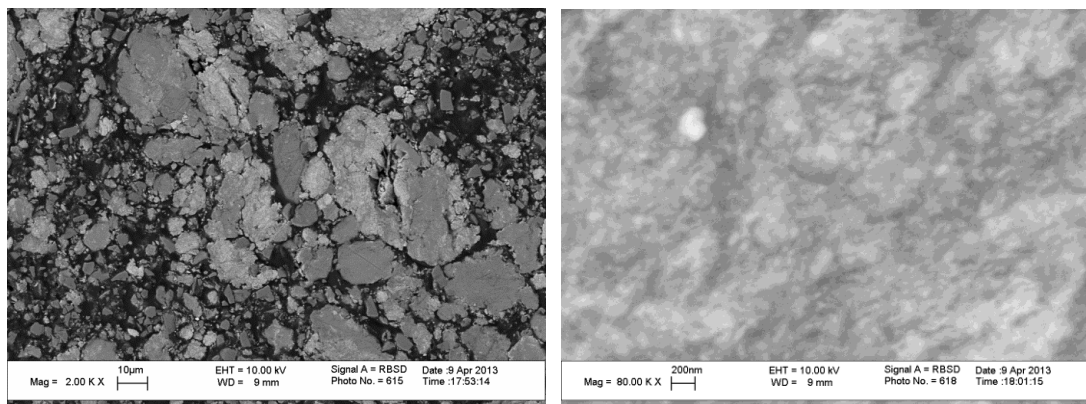


Figure 5.1 Backscattered electron SEM images of cross-sectioned $8\text{Al}\cdot\text{MoO}_3$ nanocomposite powder at low (left) and high (right) magnifications.

The low magnification SEM image revealed irregularly shaped particles, mostly sized in the range of 0.5 to 50 μm . Cursory inspection of such images as presented on the left side of Figure 5.1, shows varied brightness of individual particles. EDX spectra (interpreted using standard-free analysis) for lighter, apparently well mixed composite particles imply compositions close to the starting component mixture, $8\text{Al}\cdot\text{MoO}_3$, slightly rich in MoO_3 . Darker particles appearing to be richer in Al, were found to contain measurable quantities (1-4 atomic %) of molybdenum. No pure unattached oxide particles could be identified, unlike previously observed with similarly prepared and characterized $2\text{Al}\cdot 3\text{CuO}$ nanocomposite powders [42].

Although the difference in the brightness between Al and MoO_3 in the high magnification images was clear, the boundaries of the MoO_3 inclusions were difficult to trace. It appeared that many inclusions contacted one another, making it impossible to identify individual inclusions using image processing. Thus, inclusion sizes or inclusion

size distributions could not be directly obtained using image processing as was done for $2\text{Al}\cdot 3\text{CuO}$ nanocomposite powders [42]. The characteristic dimensions of the molybdenum oxide inclusions visually appear to be in the size range of 10 – 200 nm. It was also difficult to make a qualified assessment of the inclusion shapes. Both inclusion size and shape were therefore treated as adjustable variables as discussed below.

The phase composition of the sample was analyzed using X-ray diffraction (XRD) on a PANalytical Empyrean multi-purpose research diffractometer. The XRD pattern is shown in Figure 5.2. Most observed peaks correspond to the crystalline phases of Al, MoO_3 , and $\text{MoO}_3\text{H}_{0.5}$, respectively. The latter material, also known as molybdenum hydrogen bronze [74] has been observed to form during mechanical milling in previous investigations [75]. The nonpolar hexane, used as a process control agent during milling, is expected to be the source for the hydrogen in $\text{MoO}_3\text{H}_{0.5}$.

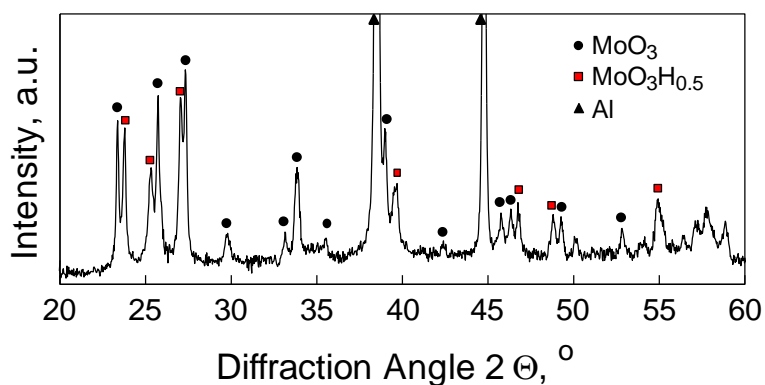


Figure 5.2 XRD pattern of the prepared $8\text{Al}\cdot\text{MoO}_3$ nanocomposite powder.

5.2.2 Thermal Analysis

Differential scanning calorimetry (DSC) and thermo-gravimetric (TG) measurements were carried out at 2, 5 and 10 K/min using a Netzsch Simultaneous Thermal Analyzer STA409 PG. Samples were heated in argon and the methodology described by [37] was generally followed.

For selected experiments, evolved gas was analyzed using a quadrupole mass spectrometer (Extrel, Model 5221) operating in residual-gas analyzer mode and coupled with the Netzsch STA. The Netzsch STA was operated in differential thermal analysis (DTA) mode with corresponding larger crucibles in order to maximize the amount of sample, and the resulting evolved gas.

Heat release was also studied using a microcalorimeter TAM III by TA Instruments under isothermal conditions at different temperatures in the range from 303 to 413 K. A sample mass of 150 ± 30 mg was used for each experiment carried out for a minimum of 24 hours. Measurements could be directly interpreted as heat release from the thermite reaction only after the sample thermally equilibrated in the calorimeter. Further details of experimental methodology can be found elsewhere [31]. In addition, TAM III measurements were carried out in scanning mode at very low heating rates of 0.0083, 0.0167 and 0.0333 K/min (0.5, 1, and 2 K/h, respectively). A sample mass of 1000 ± 50 mg was used in these scanning microcalorimetry measurements carried out from 298 to 400 K.

5.3 Experimental Results

5.3.1 Microcalorimetry

TAM III measurements for $8\text{Al}\cdot\text{MoO}_3$ at different temperatures in the range of 303–423 K are shown in Figure 5.3. The rate of heat release is normalized by the sample mass and results are shown after the signal became free of heat flow disturbances, i.e., 60 minutes after the sample had been fully inserted into the calorimeter. The results indicate an expected increase in reaction rate with temperature. The measured heat flow curves decay in time monotonically for all temperatures, except for 423 K where additional features are observed at extended exposure times. This is likely indicative of advanced stages of the redox reaction at a high overall reaction progress. Such high reaction progress processes achieved at relatively low temperatures are unlikely to occur at either ignition or aging processes, and thus are outside the scope of the present work.

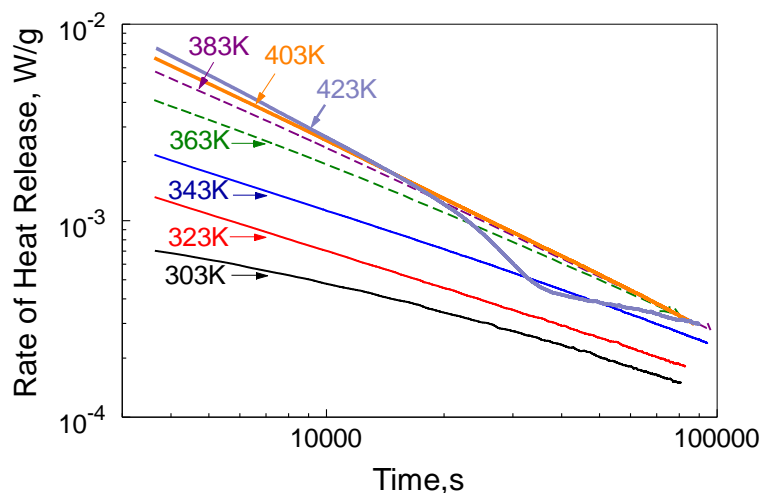


Figure 5.3 Isothermal TAM III measurements for nanocomposite $8\text{Al}\cdot\text{MoO}_3$ powders.

Figure 5.4 shows scanning TAM III measurements of heat flow for $8\text{Al}\cdot\text{MoO}_3$ in the temperature range of 300-400 K where low-temperature reactions are expected to be significant. The traces were baseline-corrected by subtracting the signal recorded with the same amount of an unmilled powder blend of identical composition to the sample. Similarly shaped heat flow signals were observed for $8\text{Al}\cdot\text{MoO}_3$ at different heating rates. There is an initial rise in the heat flow between ca. 300 and 360 K, followed by a plateau.

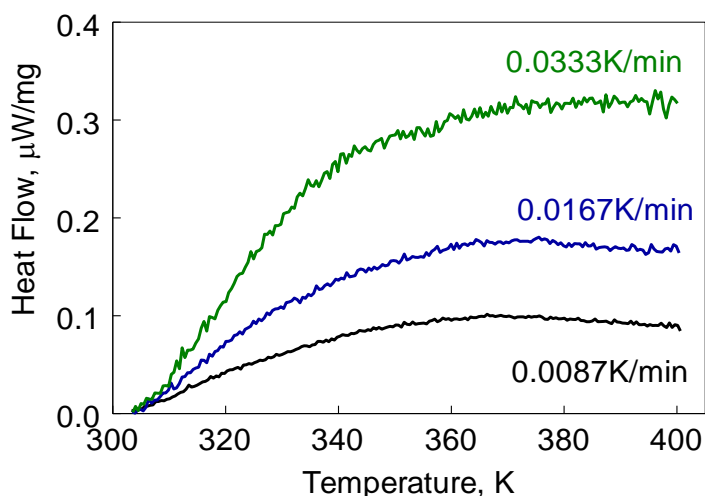


Figure 5.4 Scanning TAM III measurements for nanocomposite $8\text{Al}\cdot\text{MoO}_3$ powders.

5.3.2 Differential Scanning Calorimetry and Thermogravimetric Analysis

Figure 5.5 shows heat flows for $8\text{Al}\cdot\text{MoO}_3$ measured using DSC in the temperature range of 350-1000 K, at much higher heating rates than the TAM III measurements. These measurements were carried out with a sample mass of 3-5 mg material loaded into the DSC sample carrier. The traces were baseline-corrected by subtracting the signal recorded during the second heating of the same sample. The shapes of the recorded DSC for $8\text{Al}\cdot\text{MoO}_3$ were very similar to observations made previously [36] using the same

material. For all heating rates, the first exothermic process starts at a temperature below 400 K. A gradual rise in heat flow occurs in the temperature range of 400 – 600 K, followed by an exothermic hump observed close to 650 K. A strong exothermic peak was observed to occur between 850 and 920 K, with additional weak and poorly resolved exothermic features. A strong endothermic peak was observed in the temperature range of 930-950 K, assigned to the melting of Al_{12}Mo and peritectic formation of Al_5Mo as previously reported [36].

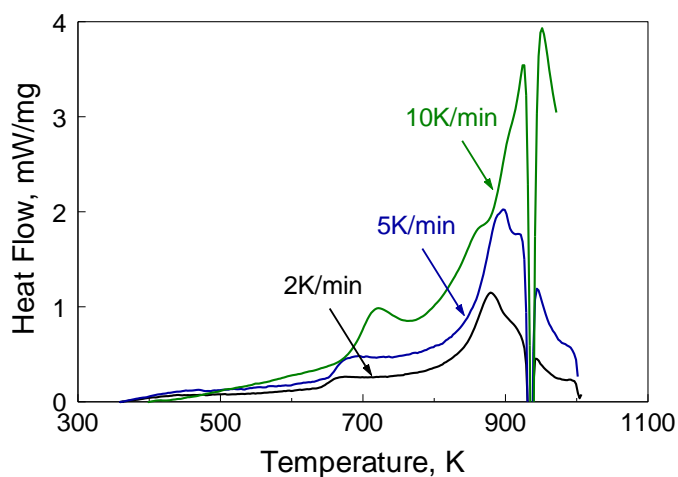


Figure 5.5 DSC curves for nanocomposite $8\text{Al}\cdot\text{MoO}_3$ powders.

To improve the accuracy and resolution of the low-temperature measurements, the mass of material loaded in the DSC sample holder was increased to ca. ~30 mg. The maximum temperature was limited to below 700 K for safety, to prevent ignition. At the final temperature of 700 K, the samples were held for 3 h to substantially react the material, and prevent reaction during the subsequent second heating. The second heating to 700 K was used to baseline-correct the DSC traces shown in Figure 5.6. The

shapes of the recorded DSC traces for $8\text{Al}\cdot\text{MoO}_3$ at low temperatures were substantially different compared to those obtained earlier for $2\text{Al}\cdot 3\text{CuO}$ [31, 42]. An endotherm is observed in the temperature range of 325-400K, followed by a gradual rise in heat flow to 600 K after which reaction accelerates. This was unlike a characteristic initial sharp rise and plateau observed at low temperatures for $2\text{Al}\cdot 3\text{CuO}$. Corresponding TG and dm/dt traces for $8\text{Al}\cdot\text{MoO}_3$ collected simultaneously with DSC at each heating rate are also shown in Figure 5.6. A weight loss in the range of 0.8-1.0% was observed. Although the total weight loss was not very substantial, it began immediately after the start of the experiment. Based on the dm/dt traces, it occurred in two steps with a stronger first step coinciding with the DSC endotherm. Samples were dried in vacuum prior to each experiment, which eliminated the possibility of free moisture being the source of this weight loss. No such weight loss was observed under identical experimental condition for $2\text{Al}\cdot 3\text{CuO}$.

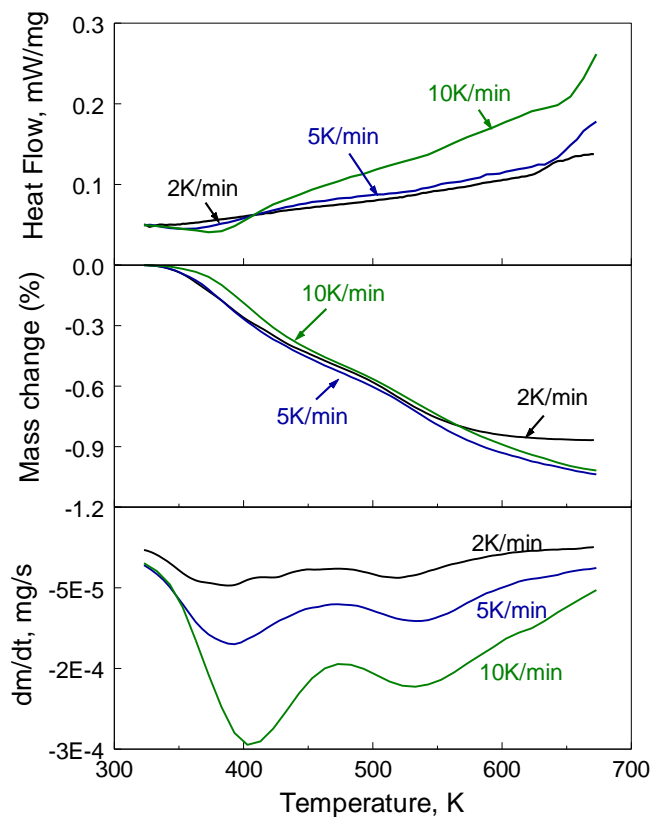


Figure 5.6 Low-temperature DSC, TG and derivative mass loss, dm/dt , traces for nanocomposite $8Al \cdot MoO_3$ powders.

To identify potential sources of the weight loss, the exhaust of the Netzsch STA was connected to the inlet of the mass spectrometer. The measurement was performed in DTA mode at a heating rate of 10 K/min. Figure 5.7 shows that the peaks of the derivative mass loss, and the DTA trace correlated with a distinct signal increase at the mass-charge ratio $m/z = 18$, corresponding to water. A second, less well correlated signal was observed at slightly higher temperatures for $m/z = 57$, corresponding to the strongest peak in the hexane mass spectrum [76]. Water as one of the main components in the evolved gas can be expected based on the observation of the hydrogen-containing $MoO_3H_{0.5}$ (see Figure 5.2). Because the material was stored submerged in hexane for

protection from oxidation, hexane in the evolved gas is also reasonable to expect. No additional gases were detected. The water peak at $m/z = 18$ is better correlated with the TG and DTA data, suggesting that the main contribution to the mass loss and the endothermic heat flow comes from the decomposition of $\text{MoO}_3\text{H}_{0.5}$.

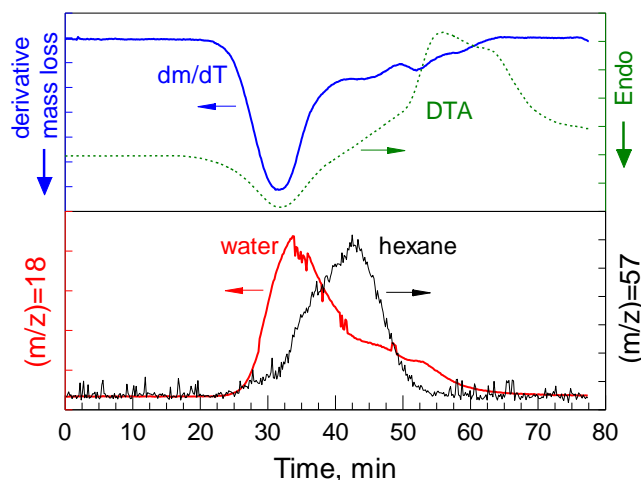


Figure 5.7 Correlation of derivative mass loss and DTA peaks with species in the evolved gas.

5.3.3 Corrected DSC and TAM III Measurements

In order to use the heat flow curves from both, DSC and TAM III measurements to quantify steps of the exothermic redox reactions, the signals had to be corrected to account for the endothermic dehydration. The DSC heat flow, Φ , was corrected by

$$\Phi' = \Phi - \Delta H_{decomp} \cdot \frac{dw}{dt} = \Phi - \Delta H_{decomp} \cdot \frac{dw}{dT} \cdot \beta \quad (5.1)$$

assuming that the relative mass loss $w = (m - m_0) / m_0$ (see Figure 5.6) is associated with an endothermic decomposition enthalpy, ΔH_{decomp} , that is constant over the relevant

temperature range. In Equation (5.1), β is the heating rate. From TG data, a minimum decomposition enthalpy of $\Delta H_{decomp} = 4000$ kJ/kg was found to consistently yield an overall non-endothermic heat flow. Deriving this value from thermodynamic reference data is difficult, since the phases involved are not well known, but it can usefully be compared with the enthalpy of sublimation of water of 2834 kJ/kg [77]. The above value of ΔH_{decomp} was then used to correct the corresponding heat flow for the dehydration process. The correction of the DSC signal is illustrated in Figure 5.8a for a heating rate of 10 K/min with a comparative summary of the measured and corrected DSC curves of all heating rates shown in Figure 5.8b.

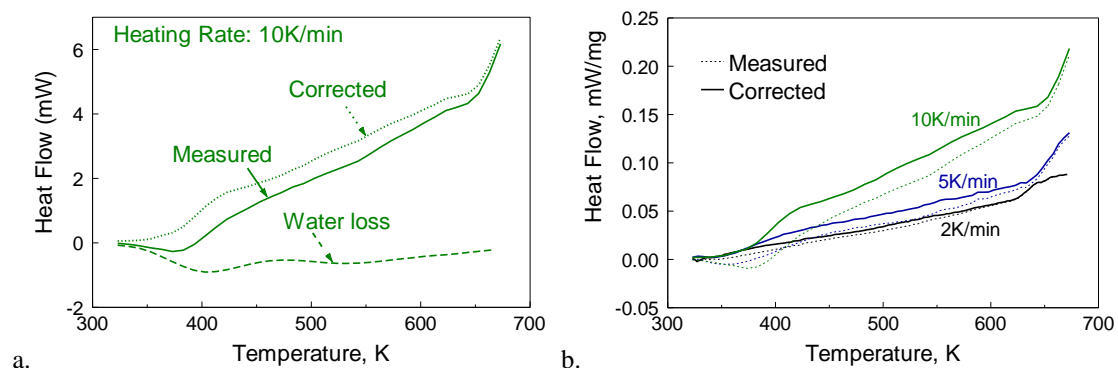


Figure 5.8 Corrected and measured DSC heat flow data accounting for dehydration. a. Correction details. b. Summary for different normalized heating rates.

The microcalorimetry measurements were performed at much lower heating rates, and gave no simultaneous information regarding any mass loss. Direct correction is therefore not possible. From the TG measurements (see Figure 5.6), it can be observed that the mass loss does not show a pronounced systematic shift with the heating rate. This suggests that the decomposition occurs near the hydration/dehydration equilibrium

and depends on temperature alone. Therefore, the mass loss as recorded by TG was averaged, $\bar{w}(T) = \sum_i w_i(T)$, and its temperature derivative was multiplied by the heating rates of the microcalorimetry experiments to obtain the estimated time derivative and the appropriate heat flow correction (see Equation 5.1). The corrected microcalorimetry measurements are shown in Figure 5.9.

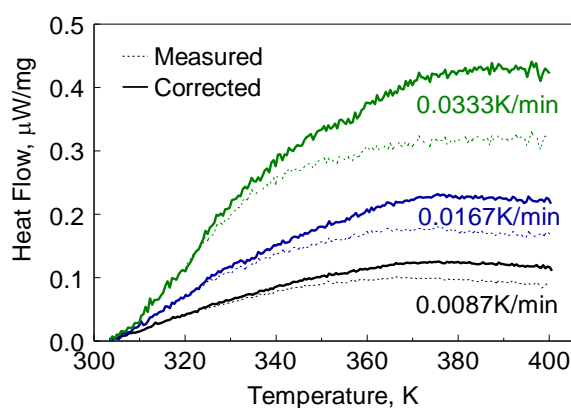


Figure 5.9 Corrected and measured microcalorimetry heat flow data accounting for dehydration.

5.4 Reaction Model

The general methodology used previously to develop a reaction mechanism for $2\text{Al}\cdot 3\text{CuO}$ nanocomposites [31] was applied to describe low temperature reaction in $8\text{Al}\cdot \text{MoO}_3$. Critical material parameters influencing the model are the geometry and size of the oxidizer inclusions and the initial thickness of the alumina layer separating oxidizer from aluminum. Due to lack of clarity in SEM images of particle cross-sections for $8\text{Al}\cdot \text{MoO}_3$ (see Figure 5.1), both spherical and planar inclusion geometries were considered, as shown schematically in Figure 5.10.

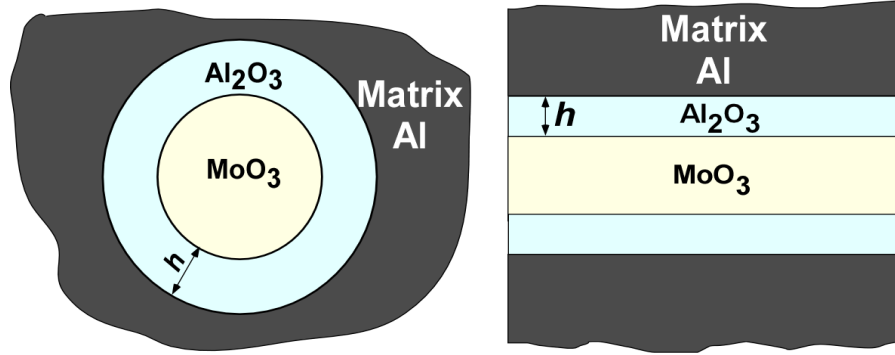


Figure 5.10 Schematic diagram for the core-shell and planar geometries considered in the reaction model.

The model previously used to describe the low-temperature reaction in terms of the rate of growth of the alumina layer by CM kinetics for $2\text{Al}\cdot 3\text{CuO}$ in [31] was applied to $8\text{Al}\cdot \text{MoO}_3$, and only a brief description is presented here. The equation describing an increase in the Al_2O_3 layer thickness, h , with temperature, T , combines an Arrhenius expression with an exponent affected by the Mott-potential:

$$\frac{dh}{dt} = k_0 \exp\left(-\frac{E_1}{RT}\right) \exp\left(\frac{E_2}{k_B T} \frac{f(h)}{h}\right) \quad (5.2)$$

Where k_0 and E_1 represent the Arrhenius preexponent and activation energy, respectively. For the Mott-potential exponent, k_B is the Boltzmann constant and parameter E_2 represents the effect of Mott potential on the rate of mass transfer. It was taken as a linear function of temperature, following [31]:

$$E_2(T) = a + bT \quad (5.3)$$

Where a and b are constants. In the case of spherical geometry the function, $f(h)$, in Equation (5.2) is the ratio of the radii of the Al_2O_3 shell and MoO_3 core. For the planar case, $f(h)=1$.

The heat effect produced by the growth of oxide layer according to Equation (5.2) was correlated with the TAM III and DSC measurements considering the redox reaction:



The total heat flows measured in TAM III and DSC measurements were expressed based on the individual heats of formation of components in reaction (5.4):

$$\dot{q}_{\text{exp}} = \frac{1}{M} \sum_i \Delta H_i \dot{m}_i \quad (5.5)$$

Where subscript i stands for Al, Al_2O_3 , MoO_3 and Mo; ΔH_i is the specific enthalpy of formation of a respective component at the experimental temperature [71], and M is the total mass of material, corrected for the dehydration loss. Calculation of the individual \dot{m}_i terms accounts for the size (diameter or thickness) and shape (spherical or planar) of the MoO_3 inclusions. In calculations describing different DSC or TAM III traces, the inclusion diameter or its thickness changed in time as a function of progress of the reaction (5.4) assuming that all metallic Mo remained inside the inclusion.

Instead of reaction (5.4), the actual reaction in the nanocomposite, particularly at early stages is likely to involve formation and subsequent decomposition of partially reduced molybdenum oxides. However, when the aluminum oxide layer is correspondingly thin, its volume change, and therefore the enthalpy generation as calculated by equation (5.5), is proportional to its thickness, so that the enthalpy of reaction (5.4) and the pre-exponent k_0 in equation (5.2) form an effective combined factor that cannot meaningfully be separated. Further, accounting for the actual, partially reduced molybdenum oxides involved would increase the reaction enthalpy per amount of aluminum oxidized by a factor of two at most [78]. At the same time, the oxide layer thickness h in the denominator of the second exponent has a much stronger influence on the overall calculated enthalpy change. Therefore, reaction (5.4) was chosen as a sufficiently representative process, and no attempt was made to more accurately account for the phases involved. For the same reasons, the decomposition of the molybdenum hydrogen bronze $\text{MoO}_3\text{H}_{0.5}$ was not explicitly considered.

The unknown kinetic parameters used in the model include k_0 , E_1 (Equation 5.2) a , and b (Equation 5.3). In addition, parameters h_0 and the inclusion size, d , (diameter for sphere or thickness for planar layer), used as initial parameters for calculations were unknown. Thus, for each shape of the oxide inclusion, the model included six adjustable parameters. They were found fitting thirteen experimental curves described above, including seven isothermal TAM III measurements, three scanning TAM

III measurements, and three DSC measurements (cf. Figures 5.3, 5.8 and 5.9). The methodology of fitting is described elsewhere [31].

The rate of the low-temperature reactions addressed here was not expected to be negligible at room temperature; respectively, the sample age, varied from several hours to several weeks, was taken into account while processing the experimental data. Thus, the aging time served as an additional experimental variable affecting the apparent thickness of the Al_2O_3 layer separating Al from MoO_3 , specific for each measurement.

5.5 Model Parameters

Results showed that assuming spherical shapes for oxide inclusions yields a better match with experimental data than planar layers. Respectively, the following discussion is focused on the reaction model parameters for spherical MoO_3 inclusions. The values of the CM model parameters found by matching Equations (5.2-5.5) with the experimental curves are shown in Table 5.1, including the diameter of MoO_3 inclusions, d . As noted above, the very small value of h_0 in Table 5.1 cannot represent the thickness of a continuous Al_2O_3 layer; instead it is an effective value characterizing properties of an interface existing between Al and MoO_3 prior to the formation of a continuous layer of alumina.

The model predictions are very sensitive to the initial effective Al_2O_3 thickness, which was expected to be different for the samples stored for different times used in different experiments. The thickness predicted as a function of the sample storage time at room temperature is shown in Figure 5.11. Most of the isothermal TAM III measurements were performed with freshly prepared samples. The scanning TAM III measurements were performed with the samples stored for about one week, so that the effective Al_2O_3 thickness was expected to be close to 0.11 nm. The DSC measurements were performed with the samples stored between two and three weeks, implying the Al_2O_3 thickness close to 0.13 nm.

Table 5.1 Values of Kinetic Constants or their Ranges Obtained from Processing TAM III and DSC Measurements

Model Parameter	Values
h_0 , nm	0.08
d , nm	50
k_0 , nm/s	$3 \cdot 10^{-5}$
E_I , kJ/mol	28
a , 10^{-22} J·nm	-88
b , 10^{-22} J·nm/K	0.33

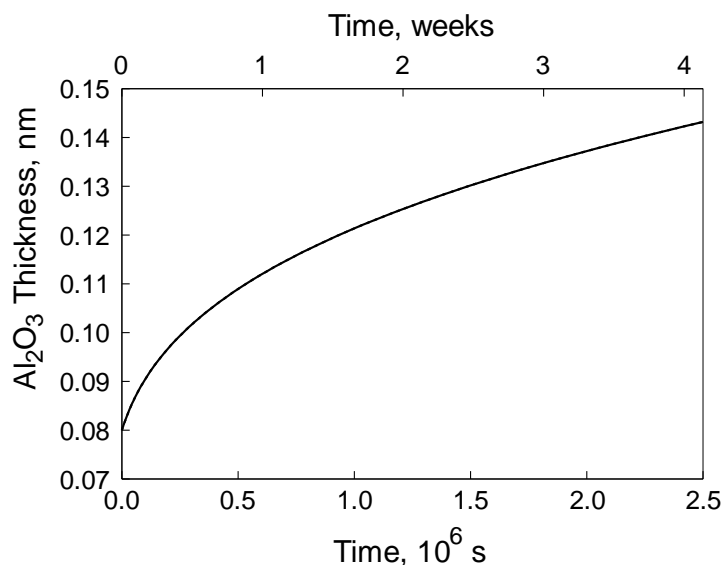


Figure 5.11 Predicted effective thickness of the Al_2O_3 layer as a function of the storage time of the $8\text{Al}\cdot\text{MoO}_3$ samples at room temperature.

Plots for the experimental heat flows and inferred Al_2O_3 layer thickness as a function of time for three, selected for example, isothermal TAM III traces are shown in Figure 5.12 along with the respective calculated curves. Although the samples used in these tests were not stored for any extensive periods of time, the measurements did not start until after about 1 hour after the sample was placed in the pre-heated calorimeter. The time “0” in Figure 5.12 corresponds to the beginning of the measurement. The reaction, occurring during the previous hour, necessary to equilibrate the sample, must have resulted in a greater initial Al_2O_3 thickness compared to that given in Table 5.1. The maximum initial thickness for each sample was estimated assuming that the material was subjected to the pre-set calorimeter temperature for an hour. These estimates are shown in Table 5.2. The actual thickness must have been smaller because of the thermal inertia of the sample. In order to compare the experiments and calculations, a specific, reasonable Al_2O_3

thickness must be assumed for each temperature. These assumptions were made so that the thickness inferred directly from the heat flow curves coincided with that in the model for the beginning of each experiment, time “0”. These assumed thickness values are also shown in Table 5.2 for each temperature. They are, as expected, less than the maximum estimated thickness.

During each isothermal measurement, the measured heat flows changed by more than an order of magnitude, which is well represented in the model. All calculated heat flow curves are somewhat overpredicting the experimental data at short times but become lower than the experimental heat flows at longer times. The agreement between experimental and simulated oxide thickness growth is reasonably good for all temperatures.

Table 5.2 Estimated and Assumed Effective Initial Thickness of the Al₂O₃ Layer for the Samples Used in Isothermal Calorimetry Experiments

Temperature, K	Effective Al ₂ O ₃ thickness, nm	
	Estimated: subject to the calorimeter temperature for 1 hr	Assumed to achieve match with experiment at t=0
323	0.09	0.08
343	0.12	0.10
383	0.19	0.14

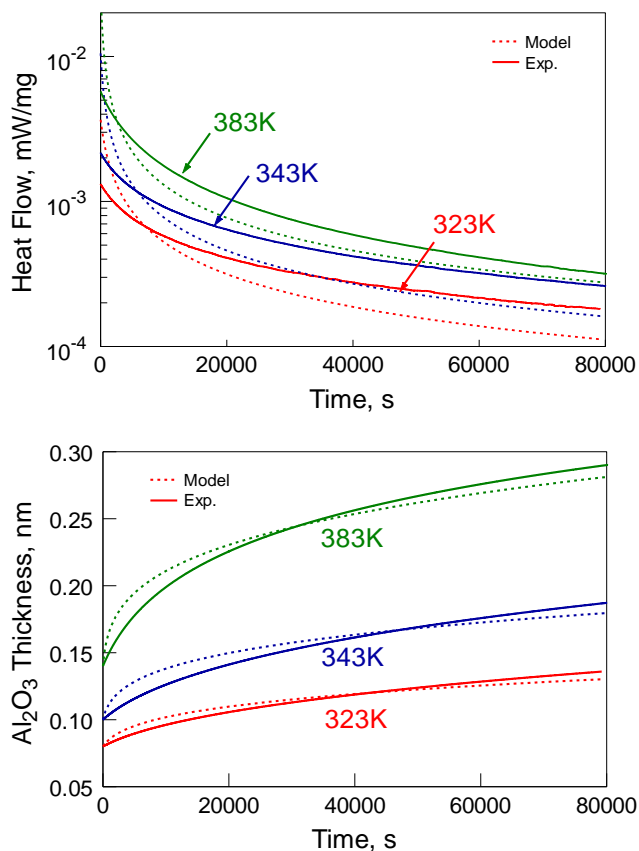


Figure 5.12 Heat flows and respective alumina thickness as a function of time for isothermal calorimetry experiments. Solid lines represent measurements; dashed lines are predicted using the identified reaction kinetics.

Comparisons of experiments and calculations for the scanning calorimetry experiments for a broad range of heating rates are shown in Figures 5.13, 5.14. The model represents equally well the initial, low-temperature reaction for the range of heating rates spanning three orders of magnitude, from 0.0083 to 10 K/min. The agreement is good for both heat flows and respective effective thicknesses of the growing Al₂O₃ layers.

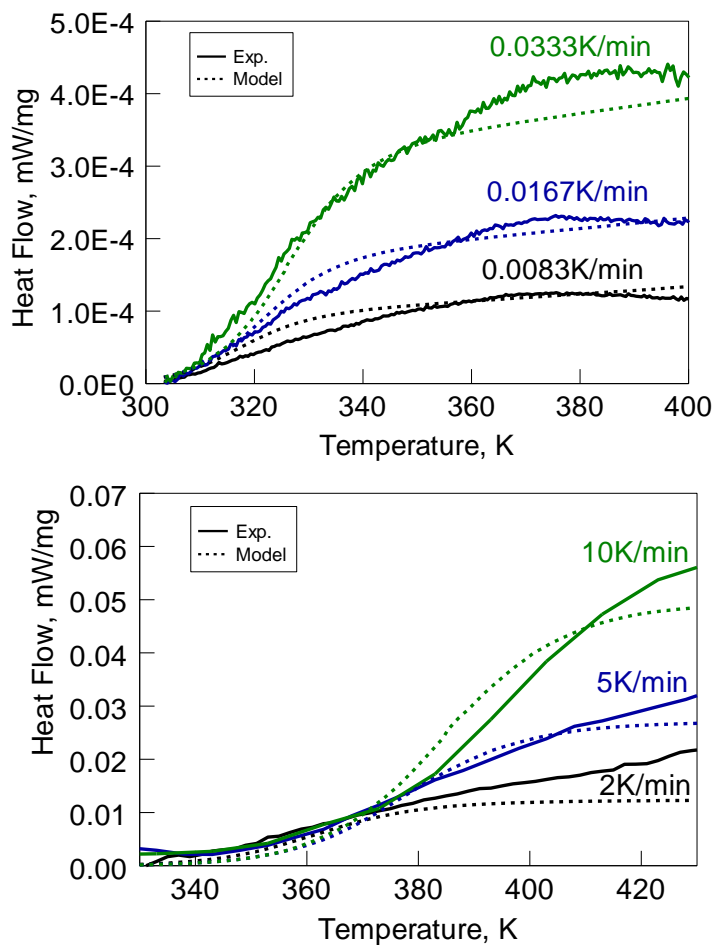


Figure 5.13 Experimental and calculated heat flows from TAM III experiments (left) and DSC (right).

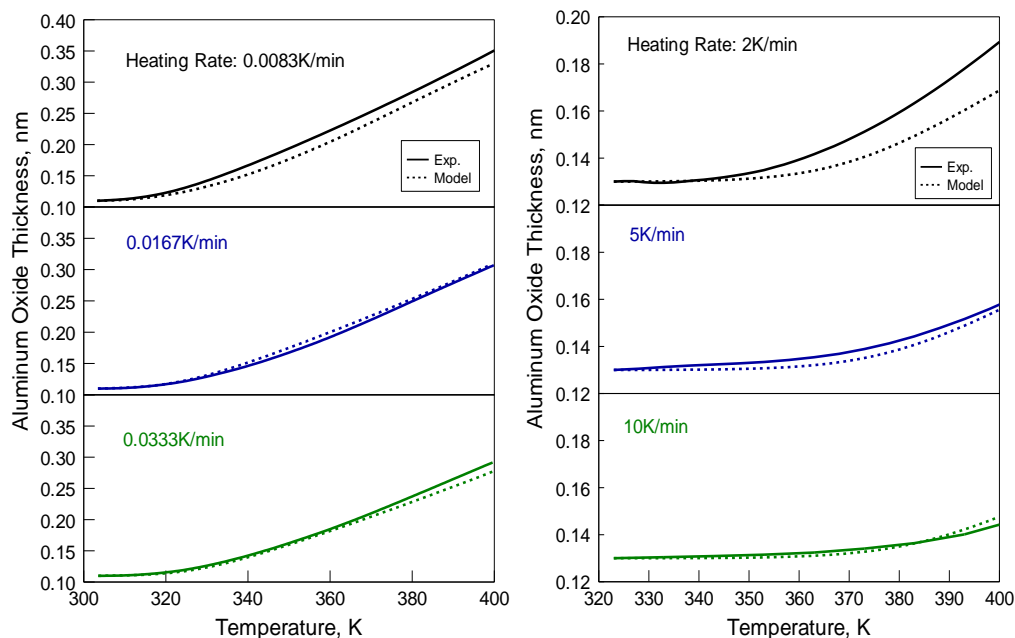


Figure 5.14 Inferred from experiments and calculated thicknesses of the Al_2O_3 layer for TAM III experiments (left) and DSC (right).

The parameters for the CM model shown in Table 5.1 were identified considering experimental data at temperatures below 400 K, used for all comparisons in Figures 5.12 – 5.14. The predicted data begin systematically deviating from the DSC measurements at temperatures exceeding 400 K. The model predicts a plateau in the heat flow, similar to that observed earlier for Al/CuO composites [31], whereas the experiments with Al/MoO₃ show a slowly accelerating reaction (cf. Figure 5.8). Exothermic features observed at temperatures higher than 600 K (cf. Figure 5.5) were similar to those observed for Al/CuO; they were reasonably well described by the multistep model accounting for growth of individual alumina polymorphs and respective polymorphic phase transitions [33]. However, the temperature range between 400 and 600 K was not properly described. Postulating different alumina growth kinetics in the presence of Mo, which would become

relevant at higher temperatures, did not result in a better match between observation and prediction.

The current CM model is sensitive to the parameters shown in Table 5.1, and it is therefore possible that slightly different parameters will reproduce the behavior between 400 K and 600 K better than the current set. The current parameters do, however, represent the best fit with all considered experiments, including isothermal and scanning measurements over a wide range of heating rates, and further parameter optimization is not possible. Without claim as to a specific physical process, and to demonstrate the parameter sensitivity, it can be noted that a simple change of one parameter, the activation energy E_1 from 28 kJ/mol below 400 K, to 54 kJ/mol above 400 K better describes the observed DSC measurements. The resulting match is illustrated in Figure 5.15. The switch in the activation energy E_1 at 400 K may represent a change in properties or structure of the forming clusters of Al_2O_3 at the Al/MoO_3 interface. It cannot be ruled out that additional processes, related to the stepwise decomposition of MoO_3 to MoO_{3-x} (generalized) contribute to the mismatch between observation and prediction between 400 K and 600 K. Without direct observation of partially reduced MoO_3 , and its location relative to the MoO_3/Al interface, these considerations remains speculative, however.

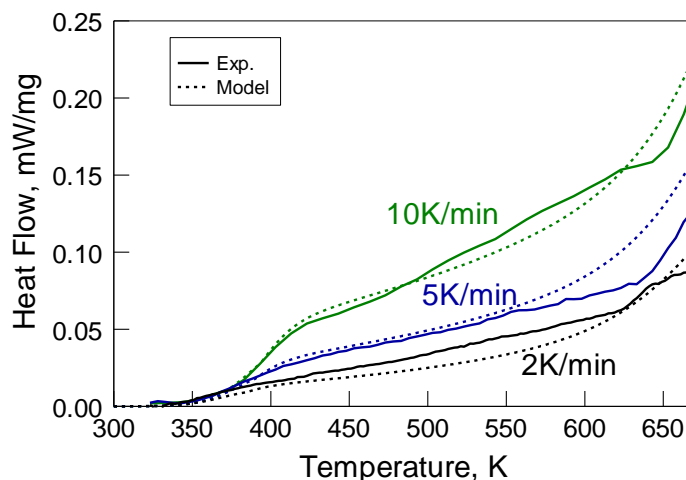


Figure 5.15 Experimental and calculated DSC curves for $8\text{Al}\cdot\text{MoO}_3$ at heating rates of 2, 5, and 10 K/min. For temperatures below 400 K, $E_I=28$ kJ/mol. For temperatures above 400 K, $E_I=54$ kJ/mol.

5.6 Discussion

Experiments with fully-dense nanocomposite $8\text{Al}\cdot\text{MoO}_3$ powder prepared by ARM were successfully processed using a multi-step reaction model validated previously for a different nanocomposite Al/CuO thermite material. Unlike for Al/CuO composites, the size and shape of the MoO_3 inclusions in aluminum matrix could not be determined by electron microscopy and had to be treated as adjustable parameters. It was observed that spherical inclusions resulted in a better match between model-predicted and measured heat flow rates in all experiments. It was further found that an average inclusion diameter of 50 nm needs to be used to describe the present experiments. This is generally consistent with the scale of mixing between Al and MoO_3 that can be semi-qualitatively assessed from the SEM images, such as shown in Figure 5.1.

Changes in the model parameters were required for the initial reaction step described by the CM mechanism. In addition, an endothermic heat effect associated with the weight loss observed for $8\text{Al}\cdot\text{MoO}_3$, primarily around 400 K, was accounted for. The weight loss was primarily assigned to dehydration. While small compared to the enthalpy of the redox reaction, and probably negligible for the analysis of ignition of such materials, this heat effect was necessary to consider in order to properly quantify the parameters of the exothermic reactions of interest.

Yet another correction, involving an adjustment in the Arrhenius activation energy was required in order to describe the raising heat flow rates measured between 400 and 600 K; without such an adjustment, the calculated heat flow becomes nearly constant, as was indeed observed for Al/CuO but not for Al/MoO₃ thermites. This adjustment is thought to represent a change in the properties of the interface separating Al from MoO₃ occurring near 400 K.

The thickness of the above interface, assumed initially to be composed of Al₂O₃, was also treated as an adjustable parameter. With a value of 0.08 nm, it was identified in the model to be surprisingly small – less than 0.14 nm, the diameter of an oxygen (II) ion. In our previous study on Al/CuO nanocomposites this thickness was close to 0.5 nm, which can be compared to bilayers of close-packed oxygen (II) ions, similar to layers found along the [111] direction in gamma alumina ($d_{111} = 0.457$ nm), or along the crystallographic c axis in alpha alumina ($1/3 d_{001} = 0.433$ nm), and therefore may be interpreted as a forming

Al_2O_3 monolayer (values from [79]). This discrepancy is striking: this thickness clearly does not describe a true oxide layer. Instead, it gives an effective value of the interface thickness. It can be proposed that the interfacial layer separating metal and oxidizer is not continuous. Instead, it can include separated clusters, in which oxygen-aluminum bonds are present. The number of such clusters would increase with temperature, resulting in an effective increase in the interface thickness as represented in the model. Considering this complex interface morphology, the detailed reaction mechanism implied by the CM model and rate limited by electric field accelerated diffusion may appear as somewhat naïve. However, the ability of the CM model to describe a wide range of experiments reported here is impressive and may be practically useful.

A preliminary assessment of the utility of the present model for describing ignition of $8\text{Al}\cdot\text{MoO}_3$ nanocomposite powder can be obtained by applying it to a situation of the powder placed on a heated substrate. A respective computational model was presented earlier [33] to interpret experiments with powders ignited on an electrically heated filament. Here, the reaction model modified for $8\text{Al}\cdot\text{MoO}_3$ was used; powder was considered to consist of $22\ \mu\text{m}$ particles, representing the average particle size for the prepared material. The powder was placed on a filament forming a $90\text{-}\mu\text{m}$ thick coating. Heating rates varied in a broad range from 10^3 to 10^9 K/s were considered. Rates of $10^3\text{-}10^4$ K/s represent the filament ignition experiments, whereas the higher heating rates occur for powders heated by a laser beam, electric spark, or in a fireball produced by a high

explosive. The heat transfer processes considered in the computational model account for the conduction between the substrate and powder, conduction within the powder particles, and for convection in the surrounding air. The model was not altered for different heating rate calculations. As the heating rate increases, the temperature gradients in the heated powders grow; at the same time, the effect of heat losses becomes smaller. While not representing different experimental situations perfectly, the calculations evaluate the effect of exothermic reactions in different heating scenarios.

Results in terms of the rate of heat production by the heated particles are shown in Figure 5.16. A spike observed at the lowest heating rates, between 900 and 1000 K represents a transition from amorphous to γ -Al₂O₃. This is the temperature range in which ignition occurs in the heated filament experiments. The rate of heat generation is observed to exceed ca. 0.1 mW/g. It is interesting that at higher heating rates, unachievable with the heated filament experimentally, but occurring for alternative ignition stimuli, the rate of heat generation passes the threshold of 0.1 mW/g at much lower temperatures, below 400 K. For such low temperatures, the only substantial heat generation is produced by the CM mechanism considered in detail here. Thus, it is reasonable to suggest that at very high heating rates, the low-temperature exothermic reactions described by Equations 5.2-5.5 cause a rapid self-heating of the nanocomposite thermite particles leading to their ignition.

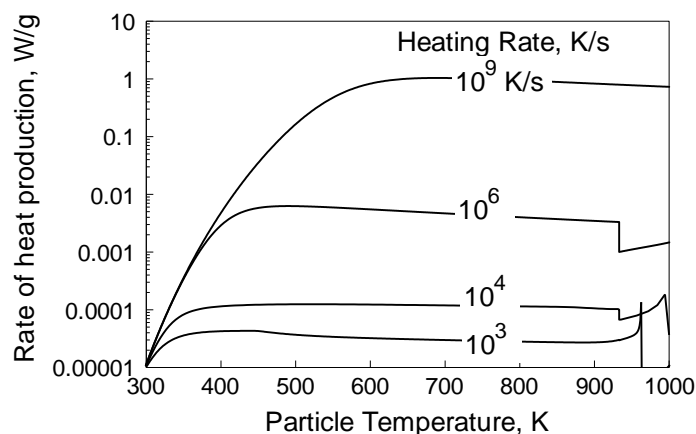


Figure 5.16 Calculated rates of heat production by 22- μm diameter nanocomposite $8\text{Al}\cdot\text{MoO}_3$ particles placed on a surface heated at different rates.

5.7 Conclusion

Low temperature, exothermic reactions in the Al/MoO_3 nanocomposite thermites prepared by arrested reactive milling were successfully described by Cabrera-Mott formalism, similar to the reactions in nanocomposite Al/CuO nanocomposite powders considered in earlier work. To interpret the experiments, it was necessary to quantitatively account for a small weight loss observed during the sample heating and assigned to its dehydration. In addition, to describe the heat flow observed in DSC experiments to increase continuously from 400 to 600 K, it was necessary to assume a stepwise increase in the activation energy employed by the CM model at 400 K. Thirteen experimental curves were used to recover six unknown CM model parameters for $8\text{Al}\cdot\text{MoO}_3$. The resulting model describes satisfactorily thermo-analytical experiments with heating rates varied over 3 orders of magnitude as well as a set of isothermal micro-calorimetry measurements at different

temperatures. One of the adjustable parameters describes a thickness of the Al_2O_3 layer separating Al from MoO_3 ; the model converges when that thickness is taken to be much smaller than the molecular dimension of Al_2O_3 . This is interpreted as an indication that no continuous Al_2O_3 layer forms between Al and MoO_3 in the ARM-prepared materials. A model introduced earlier and accounting for diffusion-limited growth of and polymorphic phase changes in the Al_2O_3 layer separating Al from MoO_3 at temperatures above 600 K describes the DSC features observed at respective temperatures reasonably well.

Preliminary estimates suggest that the low-temperature reaction described by the CM mechanism quantified in the present study may lead to rapid self-heating and ignition of Al/ MoO_3 nanocomposite powders at very high heating rates.

CHAPTER 6
IGNITION OF FULLY-DENSE NANOCOMPOSITE THERMITE
POWDERS BY AN ELECTRIC SPARK

6.1 Introduction

Electro-static discharge (ESD) ignition sensitivity is one of the most important characteristics considered in the development and utilization of flammable materials. Usefulness of materials with high ESD sensitivities is limited due to dangers associated with their handling and storage. ESD is a common ignition stimulus for various flammable substances and testing the ESD ignition sensitivity is a widely accepted practice in many industries dealing with a broad range of materials [80-83]. Multiple tests, standards, and evaluation methodologies have been and continue being developed, such as American National Standards Institute ANSI/ESD S20.20, European Standard EN 13821, British Standard CLC TR 50404, National Fire Protection Association NFPA 77, and International Electrotechnical Commission IEC R60079-32, to investigate ignition behavior of different substances struck by a spark [84-87]. In particular, ESD ignition sensitivity is routinely characterized for powder-like energetic components and additives to propellants, explosives, and pyrotechnics, such as metals, oxidizers, and composite materials.

Most ESD ignition testing standards, including those used for propellants and energetic materials [88, 89], employ sparks produced by discharge of a high-voltage capacitor [90]. A commonly used measure of powder sensitivity is the so-called minimum

ignition energy (MIE). MIE is defined, somewhat loosely, as the minimum energy stored in the capacitor, for which ignition following the ESD can be visually detected. This parameter may be useful for a practical assessment of danger associated with the ESD-ignited material; however, it is poorly suited for experiments aimed to identify the ignition mechanism. The energy stored in the capacitor may not necessarily represent the energy transferred from the spark to the igniting material. Another deficiency of MIE deals with a broad range of optical signatures, which may or may not be considered as visually detectable, and thus qualified as ignition depending on the surrounding lighting and the operator's experience.

Work has been conducted recently to understand which discharge characteristics and material parameters affect ignition for flammable metals [91-95]. Studies with powders of Mg, Al, and Ti examined correlations between ESD energy, energy transfer to the powder, ignition delays, and sizes of the ignited particles [91-96]. It was shown that only a fraction of the energy stored in the capacitor is delivered to the powder [93, 94]. The experimental observations were described adequately by a simplified model assuming that most of the discharge energy is transferred to the powder as a Joule energy released at selected particle-particle contacts, presenting the main electrical resistance to the electric current through the metal powder layer [91-96]. These contacts can be identified and their resistance can be estimated considering how a polydisperse powder is packed and taking into account Paschen breakdown curve [94, 96] to describe the spark propagation through

small gaps between adjacent conductive particles. The powder is primarily heated by the passing current (Joule heat) and ignites when a thermally activated surface oxidation becomes self-sustaining. This mechanism of ESD ignition is expected to apply for all conductive powders.

Several ESD-induced burning scenarios were observed. For Mg, a burning powder cloud was always observed [93]. For Al, a burning powder cloud formed only when the ESD energy exceeded a certain threshold. Below that threshold, the ESD initiation produced individual burning particle streaks with no apparent interaction between ignited particles [94]. In the latter case, both the number and size of ignited particles increased at greater ESD energies. For Ti, particles fused to one another in thick sample layers with little to no burning particles observed, until the sample layer thickness was reduced to a monolayer [91, 95]. It was observed that when Ti powder was placed in a monolayer, individual particle streaks were produced. The particle burn times were much shorter than expected based on the powder particle sizes. The short burn times were explained by the spark discharge fragmenting the initial Ti powder particles. Thus, the powder layer thickness dramatically affected if and how the powder ignited.

The work with flammable metal powders outlined above serves as a foundation for the present effort, aimed to describe and understand ESD-induced ignition in fully-dense nanocomposite thermites prepared by arrested reactive milling (ARM) [27]. Such materials are much more sensitive to ESD ignition than pure metals. They comprise both

conductive and dielectric or semiconductor components and thus, their interaction with ESD might be more complex than it is for conductive metal powders. It is expected that powder packing, layer thickness, and particle size distributions will remain important parameters affecting ignition. In addition, the structure and morphology of the composite particles are expected to affect the ESD/powder interaction. Finally, powders with different metals and oxidizers may exhibit different ignition characteristics.

Recent work identified chemical mechanisms leading to ignition in some of the ARM-prepared materials upon their heating. It was shown that low-temperature exothermic reactions occurring in the solid phase can explain relatively low ignition temperatures observed experimentally. Such reactions are controlled by the mass transfer of reagents through a very thin growing layer of the reaction product, as described by the Cabrera-Mott mechanism.

As with pure metals, it is desired to establish a correlation between the thermal ignition mechanism mentioned above and heating the ARM-prepared nanocomposite powders by ESD. This experimental effort is focused on two nanocomposite materials: Al·CuO, for which thermal initiation was described previously [31, 33, 41, 42], and Al·MoO₃, that is being investigated currently [97]. It is expected that the present results would be helpful in establishing the applicability of the model describing thermally initiated ignition for the ESD-ignited powders.

6.2 Experimental

6.2.1 Materials

The nanocomposite powders used in this work are $2\text{Al}\cdot 3\text{CuO}$ and $8\text{Al}\cdot \text{MoO}_3$ produced by ARM [27]. They were prepared using an aluminum powder, -325 mesh, 99.5% purity, by Atlantic Equipment Engineers; copper oxide powder, 25 μm , 99+% purity, by Sigma-Aldrich; and molybdenum oxide powder, -325 mesh, 99.95% purity, by Alfa Aesar. These specific compositions were selected because their ignition by an electrically heated filament was extensively studied and characterized recently [40, 41]. Therefore, comparison of the present experiments with earlier data would be useful for the future development of a quantitative ignition model considering different ignition stimuli.

To prepare nanocomposite powders with different scale of mixing between components, each oxide powder was blended with aluminum and milled in hexane and under argon environment for 30 and 60 min using a Retsch PM 400MA planetary mill. Additional details on the milling procedure and parameters can be found elsewhere [56]. In addition to freshly milled powders used in these measurements, samples of these same nanocomposite powders prepared six months earlier (aged materials) were also tested. These materials were stored in hexane after they were prepared. Similarly, the freshly milled samples were recovered and stored under hexane prior to the ignition experiments. In order to investigate how diluting the nanocomposite thermite with a much less flammable material affects its ignition, blends of nanocomposite powders with pure metals

(Al and Ti) were prepared. Both thermites were blended with a spherical aluminum powder, nominal size 10–14 μm by Alfa Aesar, and with titanium “sponge” powder by Atlantic Equipment Engineers, Inc. For titanium, particles were shaped as rocks and had dimensions varied from about 4 to 70 μm . The thermites/metal blends were prepared by mixing the powders in a shaker mill without milling media. This mixture was agitated for 10 min. The amount of added titanium was 50 wt %. The amount of added aluminum varied from 35 to 50 wt %.

Scanning electron microscope (SEM) images for the powders used are shown in Figure 6.1. Differences in SEM images between the nanocomposite thermites samples milled for 30 and 60 min were difficult to observe, therefore only images for the samples milled for 30 min are shown in Figure 6.1 for both $2\text{Al}\cdot 3\text{CuO}$ and $8\text{Al}\cdot \text{MoO}_3$ powders. Images of the blends prepared using the same nanocomposite thermites mixed with the pure metals are also shown.

For both $2\text{Al}\cdot 3\text{CuO}$ and $8\text{Al}\cdot \text{MoO}_3$, metal and oxidizer appear to be well mixed with no visible formation of aluminum oxide or reduced metallic phase. Both nanocomposite thermites are composed of irregularly shaped particles ranging from very fine to relatively coarse. For the nanocomposite thermite powders blended with Al, the nanocomposite powder particles can be easily differentiated in the SEM images shown in Figure 6.2 from spherical particles of Al. The powders appear to be well mixed with each other; some small thermite particles appear to be deposited onto aluminum surface. It is

more difficult to distinguish nanocomposite thermite from Ti sponge powder particles because both powders have irregular particle shapes. Titanium particles appear a bit brighter in the images obtained using backscattered electrons. They are also generally coarser than nanocomposite thermite particles for both $2\text{Al}\cdot 3\text{CuO}$ and $8\text{Al}\cdot \text{MoO}_3$.

The particle size distributions (PSD's) were obtained using a Beckman-Coulter LS230 Enhanced Particle Analyzer and are shown in Figure 6.2. For both $2\text{Al}\cdot 3\text{CuO}$ and $8\text{Al}\cdot \text{MoO}_3$ longer milling times resulted in a reduction in the volumetric mean particle size. The mean size of $2\text{Al}\cdot 3\text{CuO}$ was generally smaller compared to that of $8\text{Al}\cdot \text{MoO}_3$. These observations agree with the respective SEM images. Specific values of volumetric mean particle sizes for all samples are shown in Figure 6.2. The volumetric mean particle sizes for the pure metal powders used in blends were measured as 21.5 and 30 μm for Al and Ti, respectively.

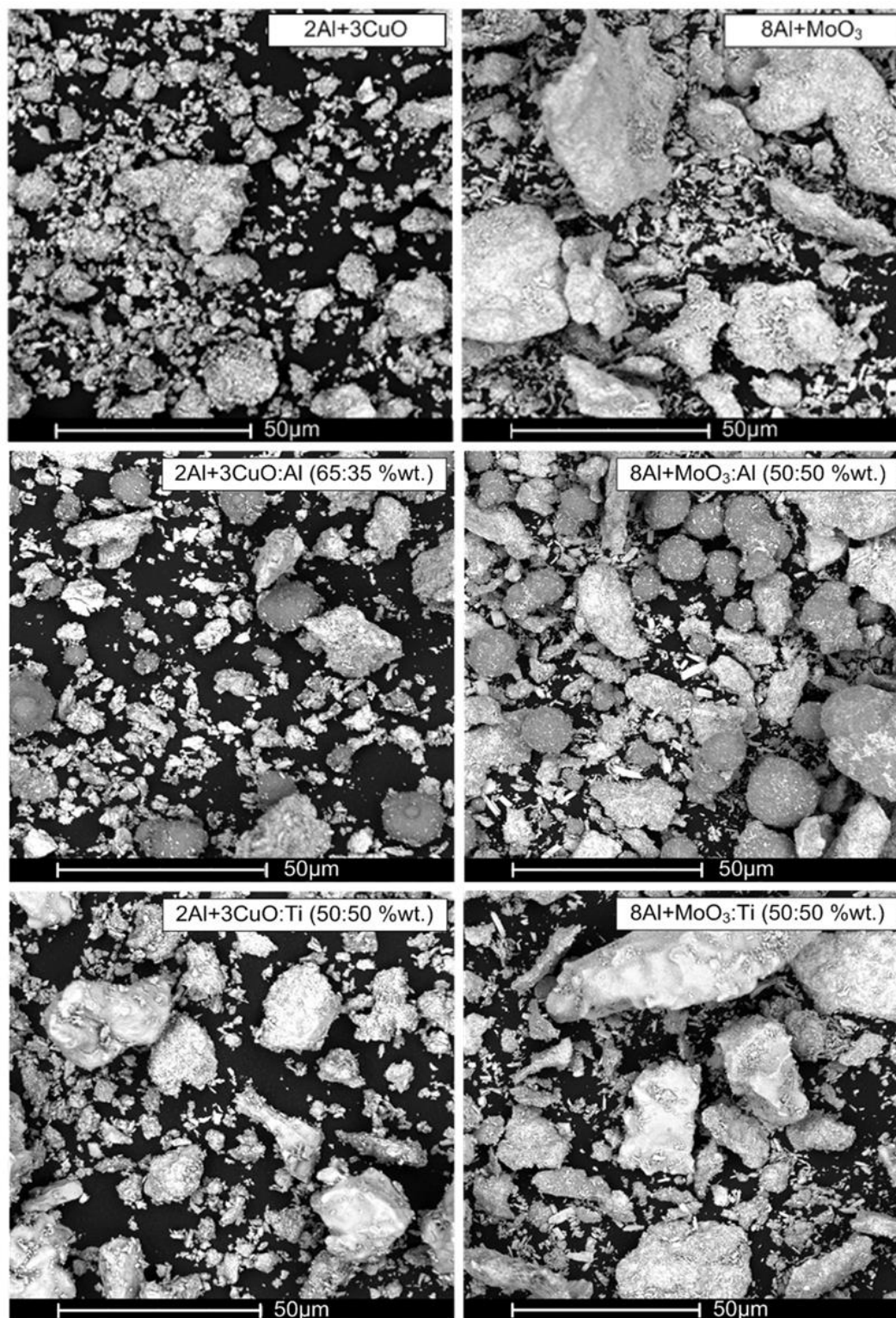


Figure 6.1 Typical SEM images showing the particle shapes and surface morphologies for the prepared nanocomposite powders and powder blends.

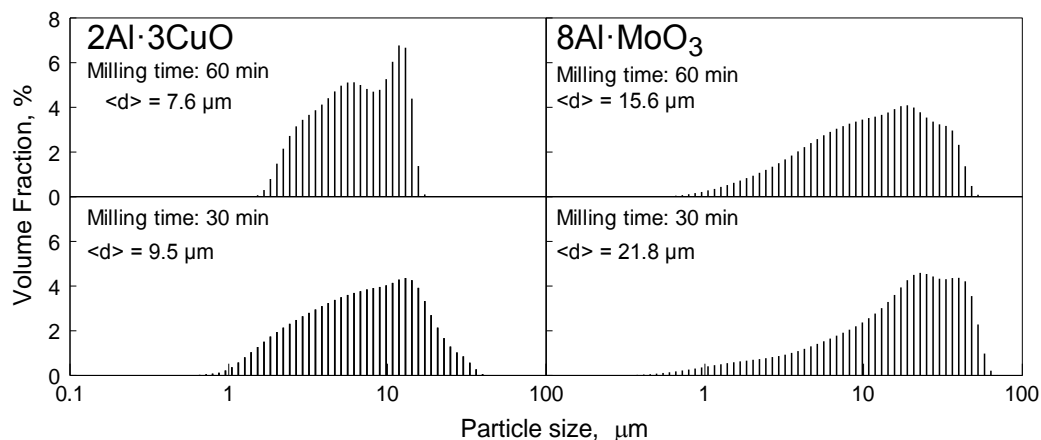


Figure 6.2 Particle size distributions for the prepared nanocomposite powders.

6.2.2 ESD Apparatus and Diagnostics

A detailed description of the experimental set up used for this work was previously given in References [94, 95]. Some modifications were made for the present measurements. Figure 6.3 shows the set up including the Model 931 Firing Test System (FTS) by Electro-Tech Systems Inc., used to generate spark discharges.

The powder is placed in a custom-made polished brass sample holder [91, 93-95]. The sample holder was grounded; a silver paste by Ted Pella, Inc., was applied to the bottom of the holder to ensure a good electrical contact. A needle-electrode is fixed approximately 0.2 mm above the powder surface, following a standard methodology [90]. A spark is triggered using FTS.

The electrodes were mounted inside a stainless steel chamber equipped with removable polycarbonate windows. The chamber was designed to be airtight with an outlet connected to a vacuum pump and fitted with pipes and valves with capabilities of

evacuating the chamber or filling it with any desired gas. The experiments were performed in surrounding air, in argon (at 1 atm), and in vacuum. The chamber volume is estimated as 564 ml based on its geometric dimensions. For experiments carried out under vacuum, the chamber was evacuated to a pressure of 3 kPa prior to the start of each experiment. To reduce contamination of the ultra-high purity argon (99.999% purity) used for experiments, the chamber was evacuated and refilled with argon at least three times. The estimated purity of argon in the chamber was ca. 98%, considering the residual air left in after purging.

Different techniques were used to prepare samples with three powder layer thicknesses. A nominal monolayer was produced by depositing a small amount of powder on a double-sided carbon tape adhered to an 18-mm-diam brass support. Excess powder was blown away, and the powder remaining on the tape formed a monolayer, as was confirmed by inspection of the prepared samples using an SEM. A sample with thickness of several mean particle diameters was made by depositing a powder suspension onto the surface of a 6-mm-diam brass sample holder and drying it out. The suspension was made by mixing 0.2 g of powder with 3 ml of hexane. The coating was allowed to dry for 5 min before ESD ignition testing. The 0.5-mm-thick samples were prepared by filling the powder into a brass sample holder with a 6-mm diameter, 0.5-mm deep cavity. Excess powder was scraped away to ensure an even layer.

The thickness of the powder sample prepared as a monolayer was assumed to be equal to the mean particle diameter obtained from the volume-based particle size distribution. For the samples prepared by drying out a powder suspension, the thickness was determined using an optical microscope. The coated surface was turned to observe the coating thickness; at least three images were taken for each coating thickness measurement. An image processing software, the University of Texas Health Science Center at San Antonio (UTHSCSA) Image Tool, version 3.0, was used. The powder layer thicknesses produced from the dried suspensions were approximately 192 ± 25 and 262 ± 22 μm for $2\text{Al} \cdot 3\text{CuO}$ and $8\text{Al} \cdot \text{MoO}_3$, respectively. The thickness of the samples prepared using a cavity in the sample holder was assumed to be equal to the depth of the cavity, $500 \pm 150 \mu\text{m}$.

In all present experiments, ESD's were produced using a 2000-pF capacitor in FTS. The capacitor was charged to a voltage varied from 1 to 8 kV to change the discharge energy. Typically, three to five experiments were performed for each voltage.

An inductance coil model 110 A with a 1 V/10 A ratio by Pearson Electronics was used to measure spark current. Current traces were visualized and recorded by a LeCroy WaveSurfer 64Xs Series oscilloscope.

As in the previous work [91, 93-95], the powder resistance, R_p , was determined based on the current traces recorded for the same ESD settings for the sample holders with and without powder. For each experiment, the current trace, showing a decaying

oscillatory pattern, was matched with that calculated for an R-C circuit connected in series (where the capacitance, C, is close to 2000 pF). The traces were matched to each other by adjusting the circuit impedance, so that the equivalent resistance for each experiment was obtained. The circuit impedance was assumed to remain constant during the discharge. The current traces were matched with a 95% confidence interval. The difference between resistances for the powder-loaded and empty sample holders was assumed to represent the powder resistance. Joule heating energy was obtained by numerical integration of:

$$\int I^2(t) R_p dt \quad (6.1)$$

Where I is the recorded ESD current and t is time.

Two types of ignition were observed. In some cases, a dust cloud flame was observed; in other cases only individual streaks of burning particles could be seen. The emission produced by the igniting powder was measured using two photomultiplier tubes (PMT) equipped with interference filters. Both PMT's were illuminated using a bifurcated fiber optics cable. The optical emission was filtered at the wave-lengths of 589 and 486 nm. The PMT outputs were also recorded using the LeCroy WaveSurfer 64Xs Series oscilloscope. It was observed that both emission signals consistently correlated with each other.

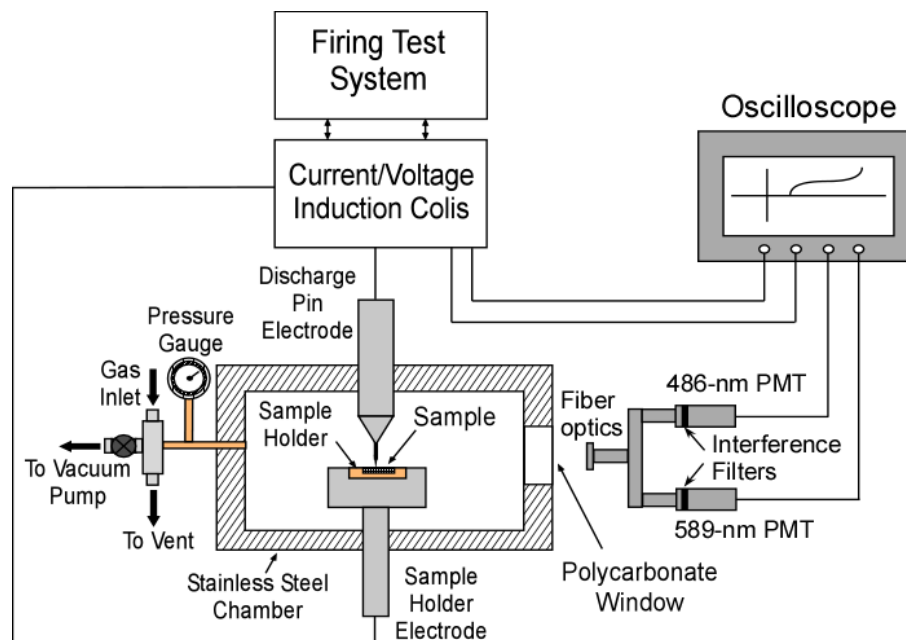


Figure 6.3 Schematic of the experimental set-up.

6.2.3 Heated Filament Experiment

This experiment was discussed in detail elsewhere recently [40, 41] and the methodology was not altered in the present project. Very briefly, about 1-cm length of a 5-cm long, 0.5 mm diameter Nickel-Chromium wire is coated with a thin powder layer. The wire is mounted in a small chamber, which is evacuated. The wire is heated electrically. Both optical emission and the pressure pulse produced in the chamber when the powder ignites are monitored using optical and pressure transducers.

6.3 Results

6.3.1 Minimum Ignition Energy

The MIE values identified based on visual detection of ignition are shown in Table 6.1. These data were obtained following the standardized testing methodology [90], using a standard sample holder and a spark gap of 0.2 mm. In these tests, whenever the powder ignited, a dust cloud flame rather than individual particle ignition was observed. Thus, ignition was readily identified by a bright flame observed for all discharge energies, down to MIE. The MIE value was taken in the case of no ignition for 5 consecutive runs.

It was not feasible to calculate the energy delivered directly to the powder at the MIE due to the extremely weak current and voltage signals obtained. Therefore, the MIE values reported in Table 6.1 were obtained following the conventional methodology and represent the energy of the charged capacitor. In addition, MIE values were assessed for nanocomposite thermite powders prepared with different layer thickness; for all cases, the visually detected ignition occurred at the same energies as shown in Table 6.1.

Low values for MIE in the range of single mJ were determined, which are consistent with those reported in the literature for similar, nanocomposite thermites. Values of 0.000125, 0.050 and 1.25 mJ were reported for Al+Bi₂O₃, Al+MoO₃ and Al+Fe₂O₃, respectively [98]. For Al+CuO, values of <0.14 mJ [99] and 4 mJ [100] have been reported while a value of less than 1 mJ was reported for nano-sized Al [101]. In a

previous study with aluminum-rich nanocomposite thermites prepared by ARM, MIE values of $8\text{Al}\cdot\text{MoO}_3$ and $8\text{Al}\cdot 3\text{CuO}$ were determined to be <0.8 mJ and 3.8 mJ, respectively [68]. It was also shown that ESD sensitivity could be reduced for $\text{Al}+\text{CuO}$ and $\text{Al}+\text{Bi}_2\text{O}_3$ by combining them with Viton A and guar gum, respectively [100, 101]. Similarly reduced ESD sensitivity resulted for the thermite/metal blends prepared in this work. For $8\text{Al}\cdot\text{MoO}_3$ and $2\text{Al}\cdot 3\text{CuO}$ blended with metal powders, MIE values were respectively in the ranges of 9.3-16.2 and 3.8-6.8 mJ.

Table 6.1 MIE Based on ESD for the Nanocomposite Thermites

Material	Milling Time (min)	MIE (mJ)
$8\text{Al}\cdot\text{MoO}_3$	30	3.81
$2\text{Al}\cdot 3\text{CuO}$	30	1.24
$8\text{Al}\cdot\text{MoO}_3$	60	1.24
$2\text{Al}\cdot 3\text{CuO}$	60	0.95

6.3.2 Modes of Ignition

Ignition experiments carried out for powder monolayers, always produced individual burning particles resulting in an emission signal similar to that shown in Figure 6.4, with no detectable ignition delay (note the time scale in μs). The overall duration of the recorded emission signal, corresponding to the time of combustion varied from ca. 70 to 100 μs . The corresponding image in Figure 6.4 shows individual burning particle streaks observed upon ignition of the monolayers of the nanocomposite thermites.

A qualitatively different mode of ignition and, respectively, different emission signals were observed for ignition of thicker powder layers. Instead of individual

particle streaks, a burning cloud was observed. It formed after a certain delay following the discharge. For example, for a 500- μm thick layer, typical emission signals are shown in Figure 6.5 for both prepared nanocomposite thermite powders. Powder ignition producing a dust cloud flame was observed in both cases; the optical signals produced by the ignited powder were noticeably delayed following the applied spark. Specifically, a small spike in the optical signal correlating with the spark current directly was observed, after which the optical signal returned to its zero level. After a while, the signal increased again. The ignition delays were taken as the time difference between the spike corresponding to the spark and the first inflection point in the optical signals increasing after the zero level observed following the spark. This processing was performed using a custom Matlab subroutine. The signal at a shorter wavelength, 486 nm, was always increasing faster than that at 589 nm, which may simply indicate that the initial emission was stronger at the shorter wavelength. It can be seen from Figure 6.4, that the ignition delay for $8\text{Al}\cdot\text{MoO}_3$ is significantly longer than for $2\text{Al}\cdot 3\text{CuO}$, which represents a consistent trend.

The ignition leading to a delayed dust cloud flame was consistently observed for the powders placed in layers with thickness varied from several particle diameters to 500 μm . Because such delays apparently indicate the development of an exothermic reaction in the reactive materials, they were investigated in more detail as discussed below.

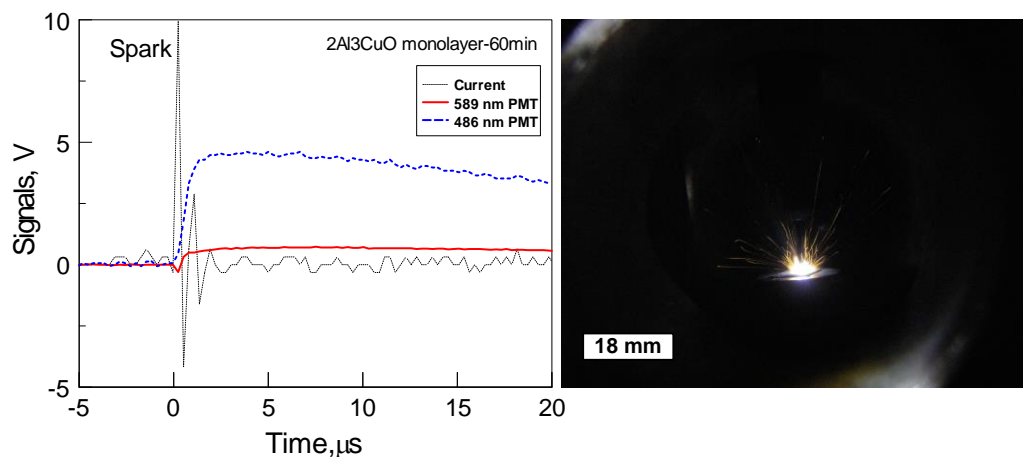


Figure 6.4 Optical emission and spark current traces with the corresponding image showing individual burning particles for a powder monolayer ignited by a 5 kV ESD.

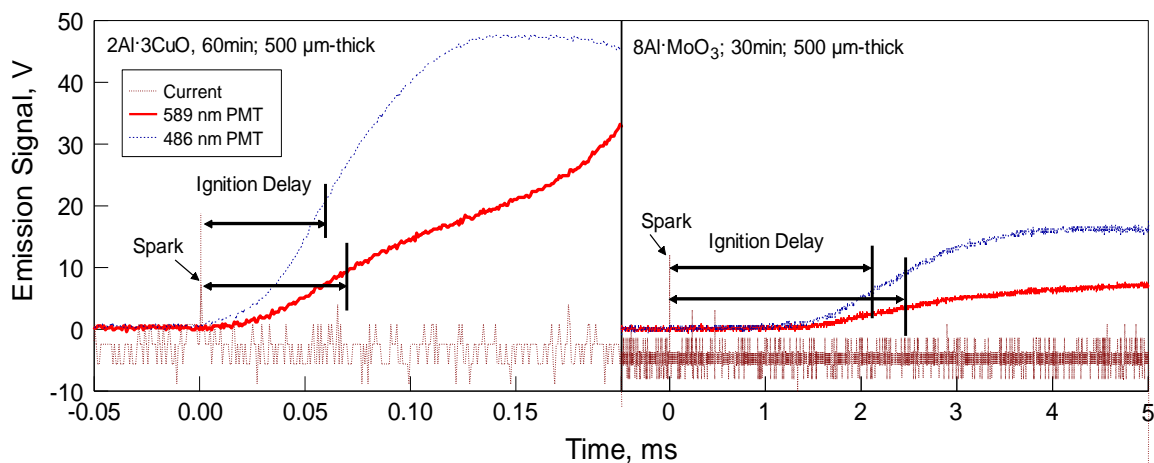


Figure 6.5 PMTs and current traces showing ignition delays for cloud ignition of the thermite powders caused by a 5 kV ESD.

6.3.3 Experiments at Reduced Pressure and in Argon

A limited set of experiments was carried out in vacuum and argon environments. ESD current traces were similar to each other for experiments in air and argon performed at the same voltage setting. In vacuum, the amplitude of the recorded current traces was reduced by 13-18 % compared to the traces recorded for identical conditions in air.

The observed ignition behavior in argon was remarkably similar to that observed in air. The burn durations in both air and argon were in the range of 5-10 ms. A delayed cloud ignition was registered for all samples except for those prepared as monolayers; the observed ignition delays were the same as in the experiments performed in air.

Images produced by monolayers of $2\text{Al}\cdot 3\text{CuO}$ powders milled for 60 min and ignited by 8-kV ESD in different environments are shown in Figure 6.6. As mentioned previously, single burning particles ejected from the region of the applied spark were observed. Images I, II and III in Figure 6.6 correspond to ignition in air, vacuum and argon, respectively. All images were taken at the same camera settings, but images II and III were taken with the polycarbonate window in place to seal the chamber. As a result, images II and III appear more blurred compared to image I. It is difficult to observe differences in ignition through comparison of images I and III carried out in air and argon, respectively. For the ignition in vacuum, unlike for any other case, the individual particle streaks were generated during an extended period of time following the spark. The overall duration of the recorded combustion event varied from 240 to about 280 μs ; i.e., it was about three times longer than in air or argon. The particles continued to be ejected from an area expanding in time, resulting in a wider bright area apparent in image II. In addition, a bluish corona discharge was observed at this reduced pressure.

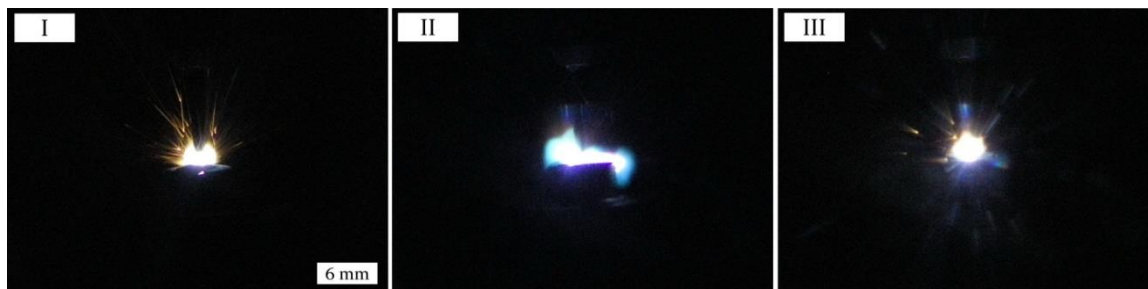


Figure 6.6 Images of ignited $2\text{Al}\cdot 3\text{CuO}$ powders milled for 60 min carried out as a monolayer in different environments: I) air, II) vacuum and III) argon.

Figure 6.7 shows two sets of consecutive images from high-speed videos recorded for a $192\text{-}\mu\text{m}$ thick layer of $2\text{Al}\cdot 3\text{CuO}$ powder milled for 30 min and ignited in both air and in vacuum. In both experiments, the capacitor was charged to 5 kV. A delayed combustion of a cloud of burning particles is observed in air (images A, B, and C). However, in vacuum, (images D, E, and F) multiple individual particle streaks are observed. The streaks begin immediately following the spark and the process continues for about 16 – 20 ms, with the area from which the ignited particles are ejected propagating from the spark location radially outward.

Qualitatively, the same ignition behavior was observed in vacuum for both materials. There was no ignition delay and multiple individual particle streaks were produced. The entire sample was consumed as was confirmed by examination of the sample holder following the experiment.

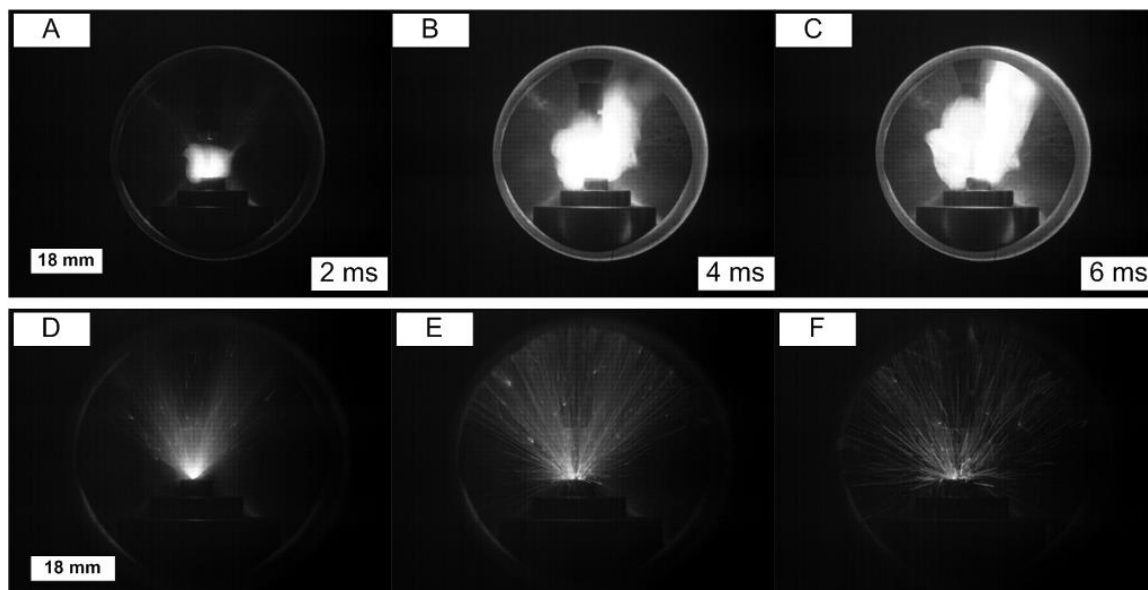


Figure 6.7 Consecutive images of the high speed video showing ignition of a 192- μm thick layer of nanocomposite powder of $2\text{Al}\cdot 3\text{CuO}$ milled for 30 min in air (images A-C) and vacuum (images D-E).

6.3.4 Ignition Delays for $2\text{Al}\cdot 3\text{CuO}$ in Air

Figure 6.8 describes ignition delay observed in air for two prepared $2\text{Al}\cdot 3\text{CuO}$ samples as a function of the measured ESD energy. The data are for powder layers with thicknesses of both 192 and 500 μm . Sets of experiments with both layer thicknesses yielding a delayed powder cloud combustion were combined in the same plot after noting that the ignition delays were effectively identical for these two sample preparations. The results are shown for both freshly milled (filled symbols) and 6-month old (open symbols) nanocomposite powders with identical compositions. Five runs were carried out for each powder and at each powder layer thickness, so a total of 10 runs for each powder are represented in Figure 6.8. Except for a few outliers, delays measured at 486

and 589 nm are well correlated with each other in individual experiments, which can be identified by identical Joule energies for both squared and round symbols. Some outliers were observed at both layer thicknesses.

The plot on the left corresponds to the sample milled for 30 min while the plot on right represents the 60-min milled sample. The results were obtained for the Joule energies ranging from approximately 9 to 21 mJ; the capacitor was always charged to 5 kV. Note that both somewhat higher and lower capacitor voltages were also tested in a limited number of experiments. The ignition delays were not affected by the variation in the voltage.

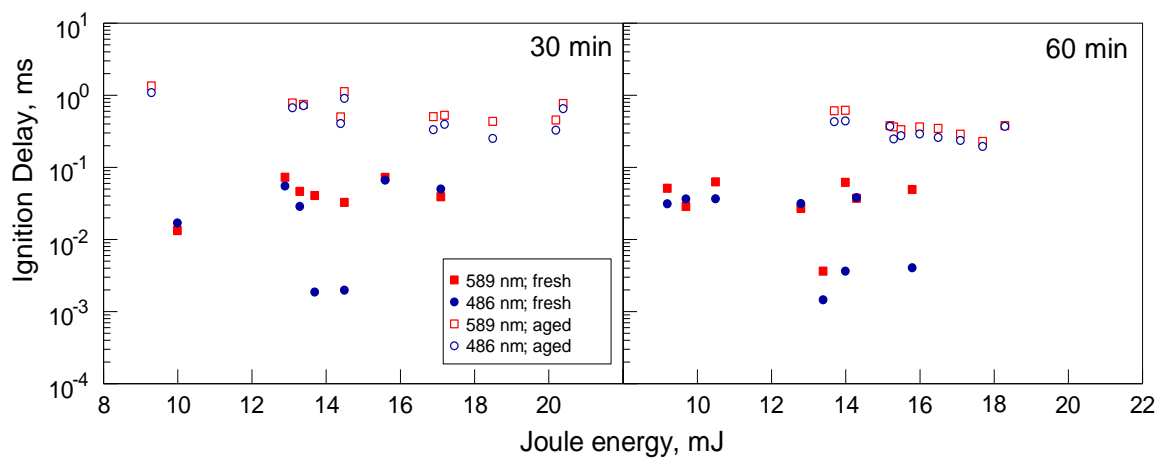


Figure 6.8 Ignition delay as a function of Joule energy in air for 2Al·3CuO samples prepared as coatings with thicknesses of 192 and 500 μm .

The aged samples for both milling times had longer ignition delays compared to the freshly milled sample. The delays shifted from 10-100 μs for the freshly milled samples to approximately 1 ms for the aged samples. This effect appears to be relevant to samples milled for both 30 and 60 min. No clear trend for the effect of other parameters

on the ignition delay was evident. As seen in Figure 6.8, Joule energy does not appear to affect the observed delay. Neither it is clear that the milling time makes a noticeable difference in the ignition delays for both fresh and 6-month aged samples. Both sets of points shown in the left and right sides of Figure 6.8 fall into the same range of ignition delays.

6.3.5 Ignition Delays for $8\text{Al}\cdot\text{MoO}_3$ in Air

Results on ignition delays for the freshly milled and aged $8\text{Al}\cdot\text{MoO}_3$ samples are summarized in Figure 6.9. All runs were carried out with the capacitor charged to 5 kV.

Three runs were made for each of the layer thicknesses of 252 and 500 μm .

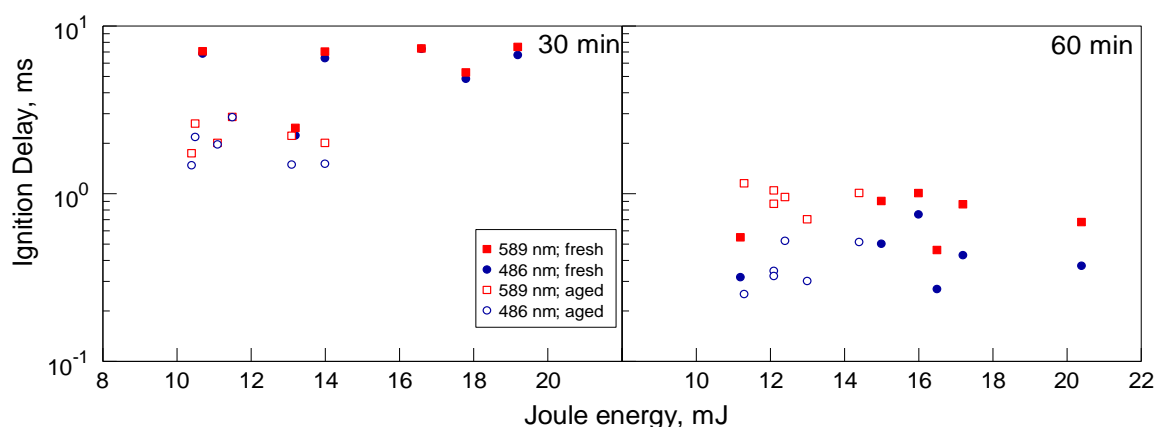


Figure 6.9 Ignition delay as a function of Joule energy in air for $8\text{Al}\cdot\text{MoO}_3$, samples prepared as coatings with thicknesses of 252 and 500 μm . Milling times are 30 and 60 min for the data shown respectively in the left and right side panels.

Note that the vertical scales in Figures 6.9 and 6.8 are different because of substantially longer ignition delays observed for $8\text{Al}\cdot\text{MoO}_3$ samples compared to $2\text{Al}\cdot 3\text{CuO}$. The effect of aging for $8\text{Al}\cdot\text{MoO}_3$ samples is remarkably different from that of $2\text{Al}\cdot 3\text{CuO}$. For samples milled for 30 min, the aged $8\text{Al}\cdot\text{MoO}_3$ had shorter ignition

delays (1 – 2 ms) compared to the fresh material (8 – 9 ms.) Also, unlike $2\text{Al}\cdot 3\text{CuO}$, no clear effect of aging was evident for the samples milled for 60 min. Finally, and again unlike $2\text{Al}\cdot 3\text{CuO}$, it is observed that for $8\text{Al}\cdot \text{MoO}_3$ longer milling results in shorter ignition delays.

Similar to the observation for $2\text{Al}\cdot 3\text{CuO}$, there was no clear effect of Joule energy or powder layer thickness on the ignition delay for $8\text{Al}\cdot \text{MoO}_3$. It is noted, however, that somewhat greater Joule energies were observed for the fresh samples, caused by altered sample impedance.

6.3.6 Blending Nanocomposite Thermites with Metal Powders

As in the other tests, these experiments were carried out with the capacitor charged to 5 kV. The powder layer thickness was consistently close to 500 μm . The ignition delay data are shown in Figure 6.10, using for clarity only the traces recorded at 589 nm.

Freshly prepared powders of both $2\text{Al}\cdot 3\text{CuO}$ and $8\text{Al}\cdot \text{MoO}_3$ milled for 30 min were initially blended 50/50% by weight with either spherical powder of Al, or with Ti sponge powders, see Figure 6.1.

Ignition delays observed for the blends using $8\text{Al}\cdot \text{MoO}_3$ are shown in the right side of Figure 6.10. The ignition delays increased from 1 – 2 ms for pure $8\text{Al}\cdot \text{MoO}_3$ to 4 – 10 ms for the 50:50 wt. % blends with both Al and Ti. The blend with Al appeared to have a slightly longer delay compared to that with Ti.

The ignition delays of the 2Al:3CuO blends were significantly longer than those observed for pure 2Al:3CuO. The delays for the 50/50 blend of 2Al:3CuO with Ti ranged from 20 to 50 ms. The 50/50 blend of 2Al:3CuO with Al did not ignite as a dust cloud. A new blend was then prepared with the thermite to metal mass ratio of 65/35. The latter blend ignited producing a burning cloud, and the ignition delays of the order of 7 – 10 ms were observed. These delays are substantially longer than about 1 ms delays observed for the pure thermite powder.

Limited experiments exploring blending higher fractions of thermites to pure metals or using blends with the thermite powders milled for 60 min yielded ignition delays similar to those for the pure thermite samples.

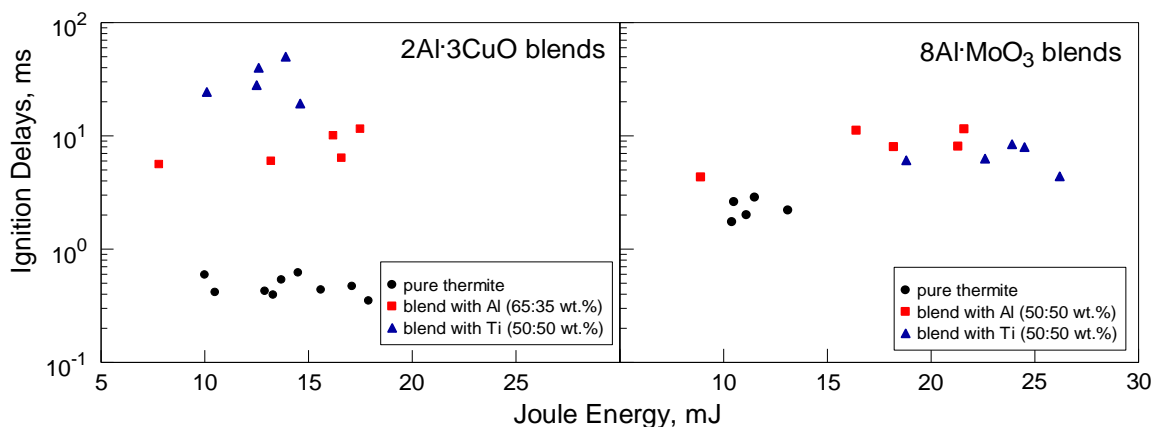


Figure 6.10 Ignition delays in air determined using emission traces recorded at 589 nm as a function of Joule energy for thermite powders prepared by 30-min milling and blended with Al and Ti powders. All powder samples are prepared as 500- μ m thick layers.

6.3.7 Heated Filament Ignition Experiments

ESD induced ignition experiments were supplemented by ignition of the same materials using an electrically heated filament. The filament was placed in a miniature chamber, and experiments were performed at a low pressure (5.8 kPa). Both optical emission and pressure signatures accompanying ignition were recorded, following earlier work [40, 41].

Ignition temperatures in the range of 800-950 K were consistent with those reported previously [40, 41]. As in the earlier measurements, the onset of optical emission signal was delayed compared to the onset of pressure pulse. Interestingly, these delays were of the same order of magnitude as ESD ignition delays observed in the present study (cf. Figures 6.8, 6.9). For more detailed comparison, the measured delays for the emission onset times compared to the pressure onset for the freshly prepared and aged nanocomposite powders are shown in Figure 6.11. Generally, delays for the optical emission onset following the pressure pulse are longer for $8\text{Al}\cdot\text{MoO}_3$ compared to $2\text{Al}\cdot 3\text{CuO}$, in qualitative agreement with data shown in Figures 6.8 and 6.9. Aging for $8\text{Al}\cdot\text{MoO}_3$ results in shorter delays, similar to the effect observed from Figure 6.9. No substantial effect of aging on the measured delays was observed for $2\text{Al}\cdot 3\text{CuO}$. The similarity between delays shown in Figures 6.8 and 6.9 and Figure 6.11 may be indicative of a similar rate-controlling process, such as heterogeneous reactions between solid fuel and oxidizer, affecting ignition in both ESD and filament ignition experiments.

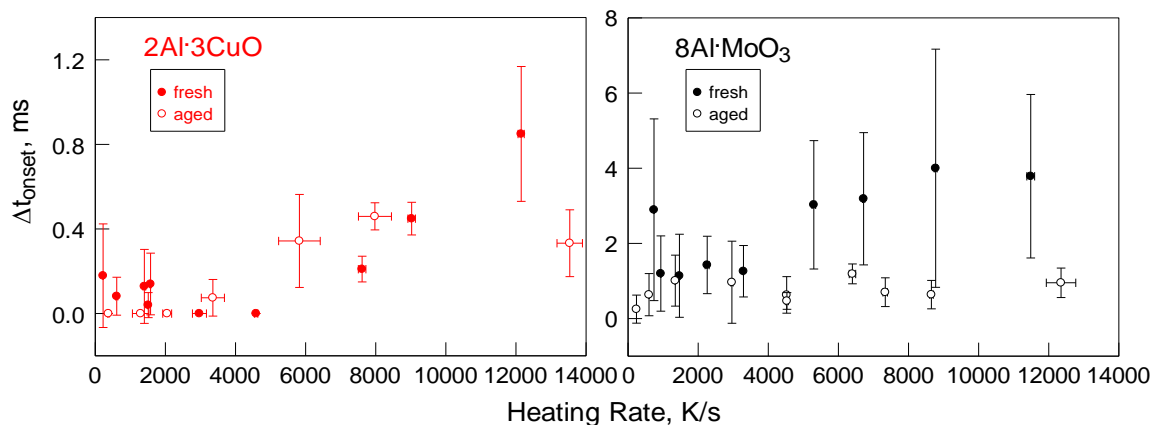


Figure 6.11 Shift between onsets of pressure and emission pulses in vacuum based on heated filament experiment at different heating rates for 2Al·3CuO milled for 60 min and 8Al·MoO₃ milled for 30 min.

To observe the effect of blending thermites with metal powder on their ignition, two samples containing 75 wt % of thermite, either 2Al·3CuO or 8Al·MoO₃, and 25 wt % of aluminum were prepared and ignited on a hot wire. The results are shown in Figure 6.12. The time shift between pressure and emission pulse increases noticeably for both blended samples compared to thermites alone.

Both 2Al·3CuO and 8Al·MoO₃ nanocomposite powders used in the tests illustrated in Figure 6.12 were milled for 60 min; note that powder blends containing nanocomposite thermites prepared by 30-min milling did not ignite in wire experiments. For the powders milled during 60 min, blends containing more than 25 wt % of aluminum did not ignite either.

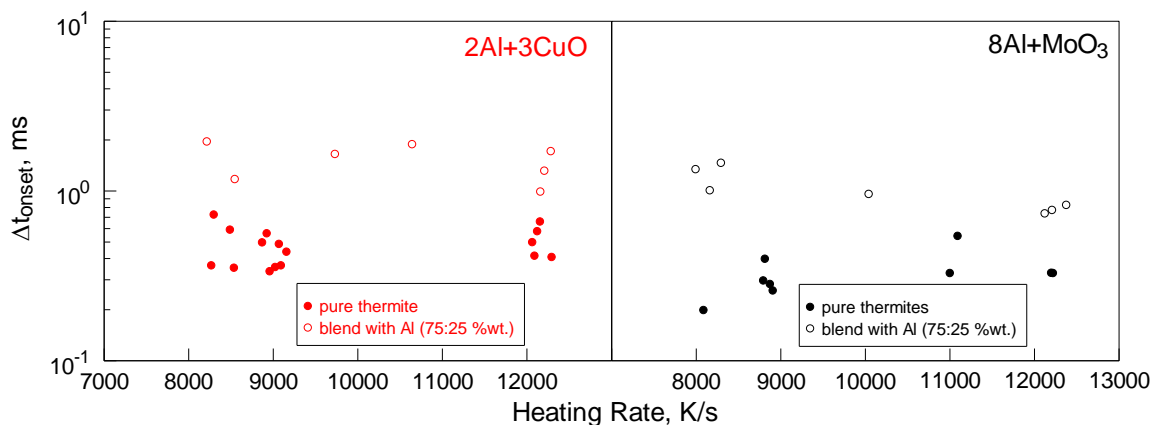


Figure 6.12 Comparison of time shift between onsets of pressure and emission pulses for as prepared $2\text{Al}\cdot 3\text{CuO}$ and $8\text{Al}\cdot \text{MoO}_3$ nanocomposite powders milled for 60 min and corresponding blends (75:25% wt.) with Al at different heating rates.

6.4 Discussion

6.4.1 Minimum Ignition Energy

Despite relatively coarse particle sizes of the prepared composite materials (Figures 6.1, 6.2), the values of MIE shown in Table 6.1, are much lower than those characterizing similarly sized metal powders [89, 93-95]. Instead, the MIE for the thermites prepared here are consistent with those reported for nano-materials comprising mixed nano-particles, e.g., see Reference [98].

The observed effect of reduced MIE at longer milling times (cf. Table 6.1) cannot be attributed to a change in the particle sizes, which is very small, as shown in Figure 6.2. It was also shown previously that the sizes of oxide inclusions remain nearly unchanged at different milling times [97]. Instead, longer milling times were shown to result in an enhanced mixing homogeneity within the nanocomposite particles and in a powder with

fewer particles with compositions heavily dominated by either fuel or oxidizer. Thus, reduced MIE is associated with an improved mixing homogeneity achieved at longer milling times.

The MIE is also affected by both composition of the prepared thermites and by the presence of additional blended powder. For the stoichiometric mixture of $2\text{Al}\cdot 3\text{CuO}$ (60-min milling time) prepared in this work MIE was 1.24 mJ, compared to 3.8 mJ reported for a similarly prepared but fuel rich $8\text{Al}\cdot 3\text{CuO}$ nanocomposite [68]. For nanocomposite powders blended with metal, MIE increased three-four times compared to the values shown in Table 6.1.

6.4.2 Modes of Ignition

Two observed modes of ignition resulting in formation of either individual burning particles ejected from the powder sample or burning powder cloud were similar to those observed for pure metal powders [91, 94, 95]. However, there were significant differences. For composite thermites, individual particle combustion was only observed for the powder monolayers and in experiments in vacuum. Conversely, for both pure aluminum and titanium powders, ignition of monolayers could generate a burning cloud, whereas ignition of thicker powder samples generated individual burning particles. Independently of material, the specific (per unit mass) energy transferred to the powder from the spark is substantially greater for the monolayers compared to thicker powder samples. Because of lower ESD sensitivity, the absolute energy required for ignition of

metal powders was much greater than that for the thermites. For pure metal powders, this high energy was suggested to cause particle fragmentation and ignition of a large number of fine particle fragments ejected from the sample.

For nano-composite thermites, ignition is observed at very low ESD energy, so that fragmentation of the particles in the spark is unlikely even for the monolayers. Instead, particles in a monolayer can be heated and ignited nearly instantaneously causing the observed individual particle streaks, unlike the case of thicker powder sample, where the energy is distributed in the powder layer so that the instantaneous heating of the powder by the spark is less significant.

For a thicker layer, after the ESD is over, a cloud ignition is observed after a noticeable delay. It can be interpreted assuming that the powder initially heated by ESD to a relatively low temperature undergoes self-heating due to an exothermic, heterogeneous redox reaction, which slowly raises its temperature and eventually leads to its ignition. In the present context, ignition signifies a transition to a rapid reaction generating substantially increased temperatures and gas-phase products, such as boiling Cu, suboxides of aluminum, e.g., AlO, Al₂O, and AlO₂, and other species. The slow self-heating must involve multiple particles heated to approximately the same temperature in order to explain the observed formation of a burning particle cloud. The cloud can form when multiple particles are ignited nearly simultaneously. Consistently with experiments, this cloud ignition mechanism involves a delay associated with the

finite rate of the heterogeneous reaction causing the particle self-heating. Kinetics of such reactions for the fully-dense nanocomposite thermites is investigated elsewhere based on detailed calorimetric studies coupled with the heated filament ignition experiments [31, 33, 40-42, 97]. A somewhat similar cloud ignition mechanism was proposed for the pure metal powders, for which the delay was attributed to a surface oxidation, which was rate-limited by the oxidizer availability in vicinity the powder layer [91]. In the latter case, the ignition delay was associated with a finite rate of gas phase diffusion of oxidizer to the powder layer.

Interestingly, the cloud ignition was observed in both air and argon environments, but not in vacuum. In vacuum, ignition resulted in multiple individual particles being ejected from the sample for tens of ms after the spark (cf. Figure 6.7). This qualitative difference in the ignition mode of powders in vacuum compared to other environments is unlikely to be explained by a relatively small change in the spark current; instead, it is proposed that the ignition mode is affected by the convective heat transfer, that is present in both air and argon but not in vacuum. Convection enables a relatively fast energy dissipation from the powder region struck by the spark directly, so that a larger portion of the powder is heated to a lower temperature compared to the case in vacuum, when a few particles struck by the spark directly may become very hot with the rest of the sample almost unaffected. Because of lack of convection, the most significant way of heat transfer in the powder bed in vacuum is through conduction. Therefore, large

temperature gradients develop in the powder. When a particle ignites, it heats its immediate neighbors rapidly, while the heat is not propagated over a large distance. On the other hand, in air or argon, convection helps to remove the heat from the hottest particles and distribute it over a larger sample area. Thus, the temperature gradients are reduced and the entire sample area may be heated due to slow exothermic reactions nearly simultaneously, resulting eventually in the observed cloud ignition mode.

6.4.3 Practical Implications

The ignition delays for the cases when cloud ignition was observed were nearly independent on the spark energy. This somewhat unexpected result can be interpreted, consistently with the discussion above, assuming that in all ignition cases, a certain threshold temperature was achieved by the energy transferred from ESD, after which the exothermic reaction became self-sustaining. The ignition delay is determined by the rate of the pre-ignition exothermic reaction. If that initial threshold temperature is substantially lower than the temperature at which the reaction accelerates to generate gas products, causing ejected particles, a small difference in the initial temperature will not result in an appreciable change in the observed cloud ignition delay.

The ignition delays depended on the type of material and on the material aging. Generally, effect of material on the observed ignition delay is not unexpected considering that the ignition delay is determined by low-temperature heterogeneous exothermic reactions. The rates of such reactions certainly are affected by the reaction chemistry

and heat transfer characteristics of the sample. The latter effect is well illustrated by longer ignition delays observed for the blends of nanocomposite thermites with metals (Figure 6.10).

The effect of aging observed for the nanocomposite thermites with CuO as an oxidizer is qualitatively consistent with the reaction model for this material [33]. For the aged powder, the thickness of the inert interface between Al and CuO increases, slowing down the exothermic reaction controlled by the transport of reacting species through that interface. For nanocomposite thermites using MoO₃ as an oxidizer, the aging results in shorter delays indicating that a different process is affecting ignition, which is not significant in the CuO-based materials. Recent thermo-analytical measurements that will be reported in detail elsewhere [97], suggest that 8Al·MoO₃ absorbs moisture forming a hydrated form of MoO₃; aged samples appear to absorb more moisture than freshly prepared powders. The absorbed moisture is released upon heating as evidenced by weight loss and a correlating endothermic feature observed in the measured heat flow curves. Release of the absorbed moisture could accelerate ignition explaining the observed aging effect for this material.

Finally a correlation between ignition delays in ESD experiments and delays between pressure and optical emission pulses in the heated filament ignition tests should be discussed. Both delays are close to each other in terms of absolute times; in both cases, the times are longer for 8Al·MoO₃; aging of 8Al·MoO₃ results in reduced delays

for both cases. The interpretation of the delay between pressure and emission signals in the filament ignition experiments proposed in References [40, 41] suggests that the initial decomposition of the oxide (CuO or MoO_3) results in gas release causing the onset of pressure pulse. The same initial decomposition of the oxides occurring in vicinity of the metal/oxide boundary can destabilize the remaining condensed oxide. The destabilization of the oxide effectively increases the concentration of mobile oxygen ions and thus accelerates the pre-ignition exothermic reaction. In other words, the delay between the pressure and optical emission in the heated filament ignition experiments can be assigned to the finite rate of one of several processes leading to ignition, namely, to pre-ignition exothermic reaction occurring when the oxidizer has been partially decomposed. It can, therefore, be suggested that the ESD also destabilizes the oxidizer, although the effect may be a combination of the Joule heating and electrical interaction of the spark with material. Once the oxidizer is destabilized, qualitatively similar exothermic reaction begins for both ESD and heated filament ignition experiments, resulting in similar ignition delays observed in both cases.

6.5 Conclusions

Minimum ignition energies for ESD initiation of the micron-sized nanocomposite thermite particles are in the single mJ range, comparable to the MIE for nano-sized powders and their mixtures, but much lower than that for reactive metal powders with

micron-size particles. Two ESD-induced ignition regimes were observed for nanocomposite thermites. Powder placed in monolayers ignited immediately; ignition resulted in individual burning particles ejected from the sample. Powders placed in thicker layers ignited after a delay and produced burning powder cloud. The same cloud ignition was observed in both air and argon at 1 atm. In vacuum, only individual particle streaks were observed for monolayers as well as for thicker powder samples. The streaks started forming during the spark, but particles continued to be ejected and burned long after the ESD was over. The area from which ejected particles were produced in vacuum expanded from the location struck by the spark throughout the entire sample.

The ignition delay for the powder cloud combustion did not depend on the ESD energy, but was affected by the composition of the nanocomposite thermite, its aging, and presence of a diluent metal powder. It was also observed that the ignition delays were close to respective delays between onsets of pressure and optical emission pulses registered during ignition of the nanocomposite powders coated on an electrically heated filament. It is suggested that the spark pre-heated particles in a thick powder layer to a threshold temperature, at which the heterogeneous pre-ignition reaction began. This reaction could be accelerated by combined Joule heat and electric current effects destabilizing the oxidizer, increasing the number of mobile oxygen ions available for

reaction. Eventually, the rate of reaction accelerates to cause formation of gaseous products and particle ejection, resulting in the observed cloud ignition.

Finally, it is noted that convection substantially affects the temperature profile in the powder sample prior to its ignition, causing nearly simultaneous heating of a group of particles eventually producing burning powder clouds.

Experimental data presented in this paper are expected to be useful for development and validation of detailed quantitative models describing ignition of nanocomposite thermites by different stimuli. In particular, the comprehensive models are expected to describe quantitatively the observed effects of powder composition, aging, and presence of inert diluent in the powder blends on the measured ignition delays.

CHAPTER 7
IGNITION OF NANOCOMPOSITE THERMITES
BY ELECTRIC SPARK AND SHOCK WAVE

7.1 Introduction

Composite materials containing components capable of highly exothermic reactions and mixed on the scale of 100 nm or finer have been developed for applications in explosives, propellants, and pyrotechnics [5]. A large surface area of the reactive interface associated with the nano-scale mixing between the fuel and oxidizer makes such materials sensitive to different ignition stimuli. Most of the quantitative measurements reported to date and characterizing reactions leading to ignition of reactive nano-materials have relied on thermal analysis [32, 65, 102-108]. Measurements associated with faster processes have also been reported, including time-resolved mass-spectrometry following ignition of nano-thermites [48, 109, 110], micro- [111] and nano-calorimetry [112, 113], and measurements of optical emission and pressure generated by the material coated on an electrically heated filament [40, 41]. In all of the above measurements, the heating rates were sufficiently low and the ignition delays were sufficiently long to ensure the temperature uniformity within the ignited nanocomposite structure. A model describing exothermic reactions for the thermally initiated, fully dense nano-thermite particles has been proposed quantifying individual reaction steps and predicting a thermal runaway to occur in vicinity of the experimental ignition temperature

[33]. However, additional processes, including the release of oxygen prior to ignition [40, 41, 66, 114, 115] and a burst of ions produced by the rapidly heated nano-thermites [116], possibly associated with the oxygen release, have been reported but have not been well understood. Such processes can affect ignition and ensuing combustion of reactive nano-materials; the effect may depend on the rate of heating and respective ignition delay.

Different ignition stimuli are expected to be important for different potential applications of the newly developed reactive nano-materials. In particular, rapid initiation processes, such as electric spark or shock wave may produce a situation when the igniting nano-material is not uniformly heated; in addition, shocks may cause both bulk and local deformations, and fractures. Some parts of the sample may be substantially hotter than others, fresh direct contacts between fuel and oxidizer may be generated at the mechanically affected locations generating hot spots and leading to localized ignition. Such localized ignition may not necessarily be well described by the earlier kinetic models, dealing with a homogeneously heated material. Furthermore, for the samples that are heated relatively slowly, the nanostructure may be lost when they burn and their temperature exceeds the melting points of the major components; conversely, the nanostructure may be preserved in very rapid reactions, occurring faster than the characteristic times required to change the material structure and morphology.

Thus, the heating rate and the method of initiation of the nano-composite reactive material may affect both its ignition kinetics and combustion dynamics.

In this paper, ignition of fully-dense, nanocomposite thermite particles prepared by Arrested Reactive Milling (ARM) [27] is studied experimentally using two methods leading to a very fast initiation. In one experiment, the particles placed on a conductive substrate are ignited using an electric spark (or an electro-static discharge, ESD). In the other experiment, the particles are struck by a supersonic flyer plate and are ignited as a result of the induced shock. In both cases, the observed ignition delays are of the order of 100 ns, which is insufficient for the temperature equilibration in the ignited particles. Results of both experiments are described and compared to each other. The implications of the present results are briefly discussed.

7.2 Materials

The nanocomposite powder used in this work, metal-rich thermite $8\text{Al}\cdot\text{MoO}_3$ produced by ARM, has been used in several recent studies focused on its ignition and combustion [36, 40, 64, 117]. It was prepared using an aluminum powder, -325 mesh, 99.5% purity by Atlantic Equipment Engineers and molybdenum oxide powder, -325 mesh, 99.95% purity by Alfa Aesar. The starting powders were blended together and milled in hexane under argon environment for 30 min using a Retsch PM 400MA planetary mill.

Additional details characterizing the milling procedure and parameters are similar to those reported elsewhere [56].

A scanning electron microscope (SEM) image of the prepared powder particles is shown in Figure 7.1. The metal and oxidizer appear to be well mixed with no visible formation of aluminum oxide or reduced metallic phase. The material consists of irregularly shaped, roughly equiaxial composite particles ranging from about 0.5 to 50 μm . The particle size distribution obtained using a Beckman-Coulter LS230 Enhanced Particle Analyzer is shown in Figure 7.2, indicating 21.8 μm as the specific volumetric mean particle size.

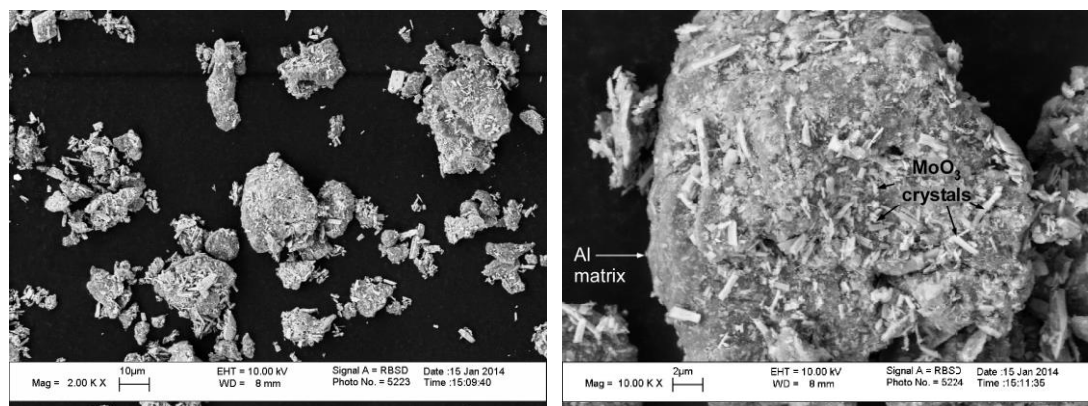


Figure 7.1 SEM images showing the particle shapes and surface morphology for the prepared 8Al•MoO₃ nanocomposite powder.

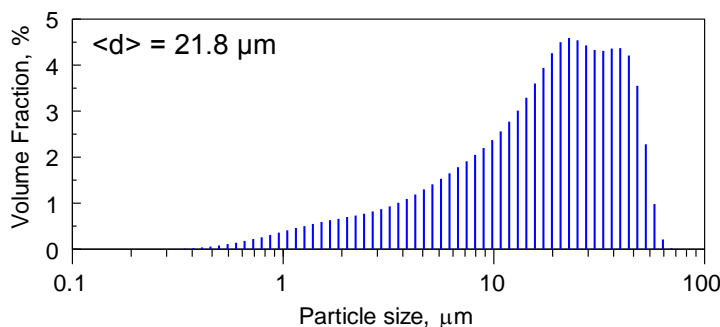


Figure 7.2 Particle size distribution for the prepared 8Al•MoO₃ nanocomposite powder.

7.3 Experimental

7.3.1 Spark Ignition

A detailed description of the experimental set up used for this work was given in References [93, 94]. Figure 7.3 shows the apparatus including the Model 931 Firing Test System (FTS) by Electro-Tech Systems Inc., used to generate spark discharges.

A monolayer of 8Al•MoO₃ powder was used in all present experiments. A small amount of powder was placed on a double-sided carbon tape attached to an 18-mm diameter custom-made polished brass support. Excess powder was blown away, and the powder remaining on the tape formed a monolayer, as was confirmed by inspection of the prepared samples using an SEM. The sample holder was grounded. A needle-electrode was fixed approximately 0.2 mm above the powder surface, following a standard methodology (MIL-STD-1751A). A spark was triggered using FTS. All experiments were performed in room air.

The discharges with different energies were produced using a 2000-pF capacitor charged to a voltage varied from 3 to 8 kV. Typically, five experiments were performed for each voltage.

An inductance coil model 110 A with a 1 V/10 A ratio by Pearson Electronics was used to measure the spark current. Current traces were recorded by a LeCroy WaveSurfer 64Xs Series oscilloscope. As in the previous work [93], the powder resistance, R_p , was determined based on the current traces recorded for the same ESD settings for the sample holders with and without powder. For each experiment, the current trace, showing a decaying oscillatory pattern, was matched with that calculated for an R-C circuit connected in series (where the capacitance, $C=2000$ pF). The traces were matched to each other by adjusting the circuit impedance, R , so that the equivalent resistance for each experiment was obtained. The circuit impedance was assumed to remain constant during the discharge. The current traces were matched with a 95% confidence interval. The difference between resistances for the powder-loaded and empty sample holders was assumed to represent R_p . Joule heating energy was obtained by numerical integration of $I^2(t)R_p\Delta t$, where I is the recorded ESD current, t is time, and Δt is the time step of the data acquisition.

In all present experiments, ignition was accompanied by multiple streaks of ejected and individually burning particles. The emission produced by the igniting powder was measured using a Hamamatsu, H3164-10 photomultiplier tube (PMT) with 0.8 ns

rise time equipped with a 486-nm interference filter. The PMT output was recorded using a LeCroy WaveSurfer 64Xs Series oscilloscope.

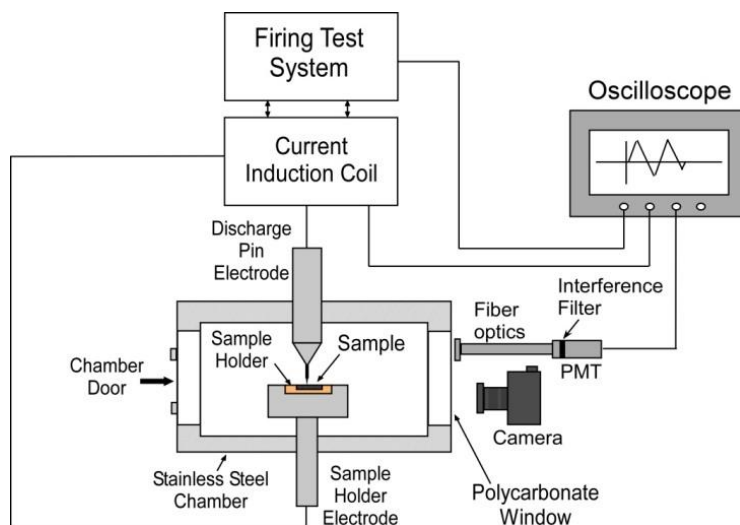


Figure 7.3 Schematic of the experimental set-up for ESD ignition.

7.3.2 Shock Experiment

7.3.2.1 Apparatus. Aluminum laser-driven flyer plates were used to shock individual 10-20 μm $8\text{Al}\cdot\text{MoO}_3$ thermite particles, and the resulting optical emission was time resolved. The apparatus for launching laser-driven flyer-plates shown schematically in Figure 7.4a has been described previously [118]. Using homogeneous flat top laser pulses with up to 2500 mJ energies, aluminum flyer plates having 50 μm thickness and 700 μm diameter were launched from a sheet of Al 1145 foil epoxied to a glass window [118]. The Al disks fly in vacuum across a 350 μm gap before colliding with the target. As they fly, the edges of the plates become distorted, but upon impact the flyers have an estimated 160 μm diameter planar region in the center, much larger than the target

particles. This type of impact process produces a planar shock in the thermite particles. The shock duration is dependent on the material being impacted, but with the flyers used here, the duration was ~ 10 ns.

A thin layer of cement was used to attach the targeted $8\text{Al}\cdot\text{MoO}_3$ thermite particles to a glass window. The targets were prepared by spin coating a $0.75\ \mu\text{m}$ thick layer of UV curable acrylic cement (Dymax 401) onto a $\frac{1}{4}$ inch thick BK7 glass window. The $8\text{Al}\cdot\text{MoO}_3$ thermite powder, suspended in hexane, was deposited onto a glass slide and the hexane was allowed to evaporate. The thermite was then tapped off the slide onto the cement layer. A UV lamp was used to cure the glue and fix the particles while the sample was attached to a spin coater. The quantity of thermite was chosen so that the thermite layer was mainly in the form of isolated individual particles. A microscope image of a typical target is shown in Figure 7.4b.

This apparatus (Figure 7.4a) allowed the targeting of an individual, size-selected thermite particle, launching of the flyer plate at a selected velocity, monitoring the velocity history of the flyer, and detection of the time-resolved emission from the shocked thermite. The velocity histories of the flyer plates were measured using a photonic Doppler velocimeter (PDV) [119, 120] operating at 1550 nm laser wavelength [118]. The PDV was detected by electronics, including a digital oscilloscope, with a combined bandwidth of 7.4 GHz, which is capable of monitoring speeds up to 5.4 km/s.

The PDV data were analyzed using a short-time Fourier transform analysis. There was an estimated 1 ns uncertainty in measuring the timing of flyer impact.

A 10x microscope objective and a dichroic beam splitter was used to observe the thermite particles, direct the PDV beam onto the flyer, collect the returned PDV signals and collect the thermite emission. The PDV beams were collimated and 60 μm in diameter, so enough of the PDV beam passed by the thermite particles (Figure 7.4a) to monitor the flyer plates.

In the apparatus, a mirror (not shown) could be insert that allowed the target to be observed with a homebuilt video microscope. The target was translated until a particle of suitable size was centered in the image, and an iris stopped down to it so that only the 50 μm diameter region immediately adjacent to the selected single thermite particle was visible. An image of a roughly 20 μm thermite particle within the iris aperture is shown in Figure 7.4c. The mirror was then removed and light directed from the thermite particle into a photomultiplier tube (Hamamatsu, H10720-20) with a 0.8 ns rise time. The PMT signals were digitized using the same oscilloscope that detected the PDV signals. The photomultiplier tube (PMT) and PDV time delays were determined using a method detailed previously [118]. This synchronization procedure involved simultaneous measurements of 10 ns laser pulses by both devices, and the synchronization error between flyer impact and emission rise time was estimated to be 5 ns.

Note that the size of the irregularly-shaped thermite particles cited, refers to the diameter of the minimum circle that could be circumscribed around the particle image. Thus particles with the same cited diameter may have significantly different masses and volumes.

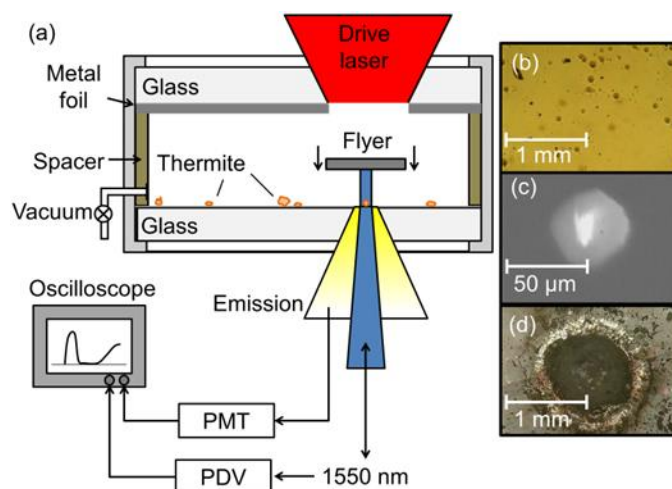


Figure 7.4 (a) Schematic of the laser-driven flyer plate system. (b) Image of a thermite target, consisting of many individual particles scattered on an optical window. A thin $0.75\ \mu\text{m}$ layer of cement was used to fix the particles. (c) Microscope image of a $20\ \mu\text{m}$ $8\text{Al}\cdot\text{MoO}_3$ thermite particle through a $50\ \mu\text{m}$ aperture. (d) Reacted thermite in the center of a crater created by impact with a $700\ \mu\text{m}$ diameter Al flyer plate.

7.3.2.2 Shock-Particle Interaction. When the laser-driven flyer-plate impacts a particle, the pressure, density, and temperature of the particle jump as the shock front passes through the sample. An accurate equation-of-state for these thermite particles is not known, or a truly accurate way to describe a shock in such a nanostructured medium. However, the shock properties can be illustrated by describing what would happen if the particles were pure Al and nonreactive, and the flyer speeds were either 1 km/s or 2 km/s.

Using the well-known Hugoniot-crossing method [121] and the principal Hugoniot of Al [122], it was determined that with a 1 km/s flyer, the shock transit time across a 20 μm thick particle would be 3.5 ns, the pressure would be 8.2 GPa and the compression would be 8.5%. Following a calculation previously presented [123], the peak temperature during the shock can also be estimate. With a 1 km/s flyer, a particle initially at 300K would be briefly heated to 366K. The corresponding values for a 2 km/s flyer would be 3.1 ns transit time, 17.8 GPa pressure, 15% compression and 493K. These conditions are crude estimates for the temperatures of shocked thermite particles on short times scales that precede the onset of exothermic reactivity. Given that it takes only 3.1 ns for the particle to be shocked, the heating rate is close to $6.3 \cdot 10^{10}$ K/s.

In the actual shocked thermite particles there may be multiple shock reverberations at the interfaces between grain boundaries. There may be defects or voids which the shock may collapse. There may be frictional heating at moving edge dislocations. There will be reflections from the thermite-glass interface. All these factors can create nanometric regions with transient temperatures that exceed the bulk temperature rises, i.e., the complicated nanostructure and microstructure of the thermite particles can promote the creation of hot spots.

Figure 7.4d shows an image of a target after the 20 μm particle shown in Figure 7.4c was impacted by the 700 μm diameter flyer plate at 1 km/s. Besides the Al crater left over from the flyer plate, one can see a smaller faint image in the central region, that

is about the same size as the original thermite particle. It is believed that this region denotes debris from the shock-reacted thermite particle.

7.4 Results

7.4.1 ESD Ignition of $8\text{Al}\cdot\text{MoO}_3$ Monolayers

Ignition experiments carried out for $8\text{Al}\cdot\text{MoO}_3$ powder monolayers always produced multiple burning particles resulting in an emission signal similar to that shown in Figure 7.5. An initial fast rise is followed by a slower increasing emission intensity. The slow rise segment becomes more apparent and extends to longer times at greater spark energies. The time axis is broken between 30 and 90 μs , while the signal continues to decrease. The overall duration of the recorded emission signal, corresponding to the time of combustion varied from ca. 120 to 200 μs and did not apparently depend on the spark energy. These times are determined from the emission traces, such as shown in Figure 7.5 while the signals exceeded three times the amplitude of fluctuations observed at the zero emission level (prior to the spark). Images in Figure 7.6 show a photograph of burning particle streaks observed in a typical experiment and partially burned particles captured on a Cu foil placed approximately 2 mm from the powder.

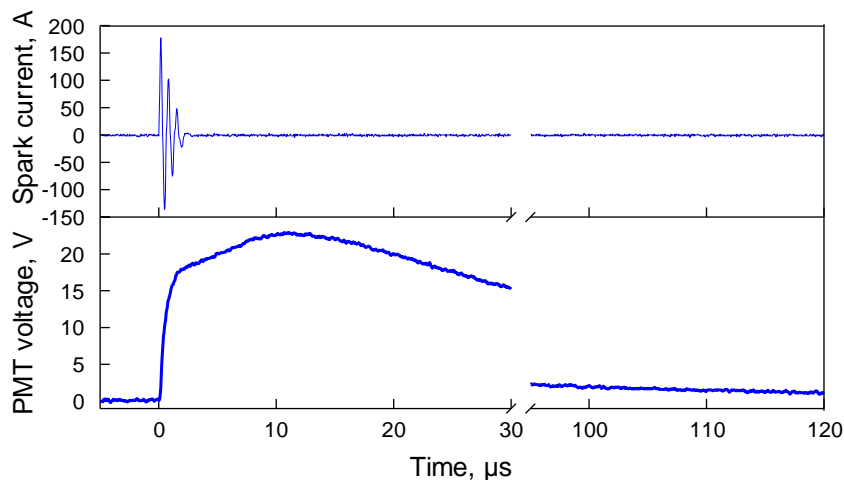


Figure 7.5 An ESD spark current trace and a PMT voltage corresponding to the emission of the burning sample recorded in an ignition test with a monolayer of nanocomposite $8\text{Al}\cdot\text{MoO}_3$ powder. The spark voltage is 8 kV.

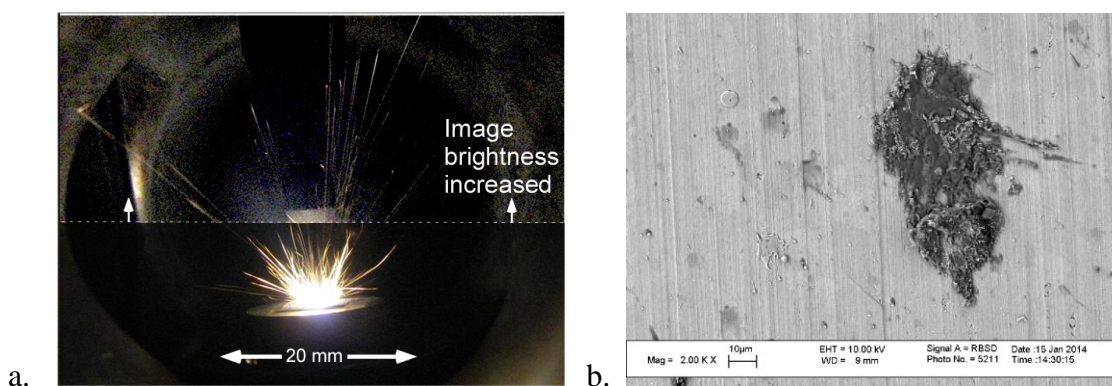


Figure 7.6 a. A photograph of the burning particle streaks recorded in an ESD ignition test with the spark voltage of 8 kV. b. An SEM image taken with backscattered electrons showing partially burned particles captured on a Cu foil placed 2 mm away from the spark-ignited powder.

In the photograph, the brightness and contrast for the top part are additionally enhanced to clarify the images of few particle streaks extending beyond the brightest area of the image. The maximum streak length is close to 50 mm. Considering the overall

emission time of about 150-200 μs , this suggests that the fastest burning particles move at a speed of about 300 m/s, approaching the speed of sound in air.

The partially burned particles captured on the Cu foil appear molten and form splattered imprints on the surface. The sizes of the captured particles change in a wide range, which appears to be similar to the original size distribution of the nanocomposite thermite (cf. Figure 7.2). A large particle with portions containing what appears to be a composite structure similar to the original nanocomposite material is seen on the right. Multiple smaller particles are seen on the left, for which almost no internal structure could be resolved.

A close inspection of the recorded spark current and emission traces showed that the onset of the emission signal is delayed compared to the spark current. These delays are clearly observed in Figure 7.7, showing the initial parts of the emission traces overlapped with the respective ESD current signals. These short delays were ignored in an earlier paper [124] where the focus was on much longer ignition delays observed when the powder was placed in a thick layer and ignited after an aerosolized cloud of the ejected particles was formed.

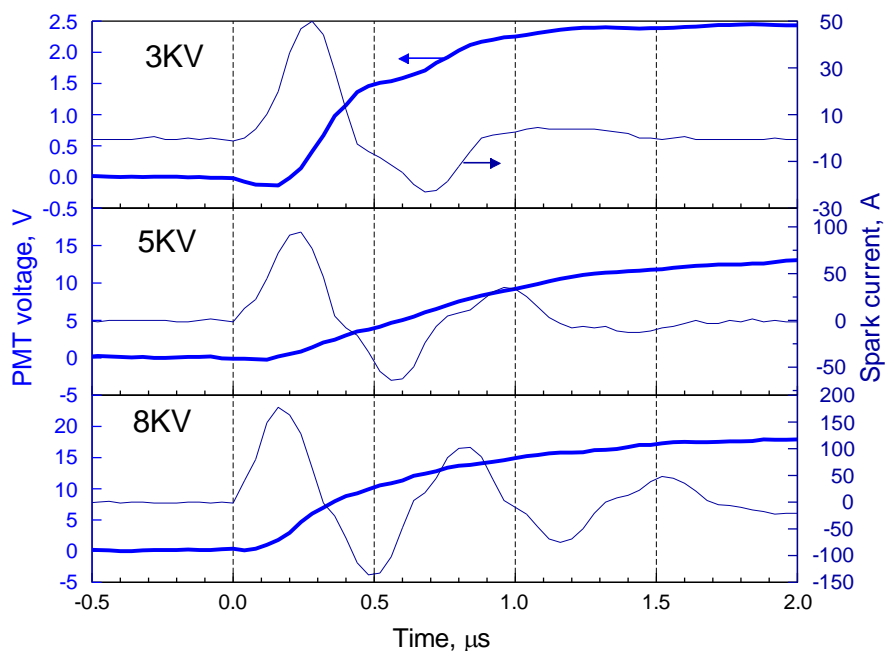


Figure 7.7 Optical emission and spark current traces showing onset differences for $8\text{Al}\cdot\text{MoO}_3$ powder monolayer ignited at different ESD energies.

The emission signals were further processed to obtain ignition delays defined as the difference between onset times for the spark current and PMT voltage, 90% of the fast rise time for the PMT signal, and integrated emission intensities determined using the PMT voltage traces. For consistency the onset instants for the current signals were defined when their values were at 10% of the maximum. The 10% and 90% values of the fast rise represents 10% and 90% of the time difference between the onset of the emission signal and the inflection point between its fast and slow rise segments, respectively. The results of the processing are shown in Figure 7.8 as a function of the spark's Joule energy. The Joule energy was consistently increased at greater spark voltages.

The ignition delay decreases from ca. 240 to 160 ns with the increase in the spark's energy. Similarly, a reduction in the 90% fast rise time was observed with the

increasing energy. Integrated emission intensities showed an opposite trend and were observed to increase at greater spark energies.

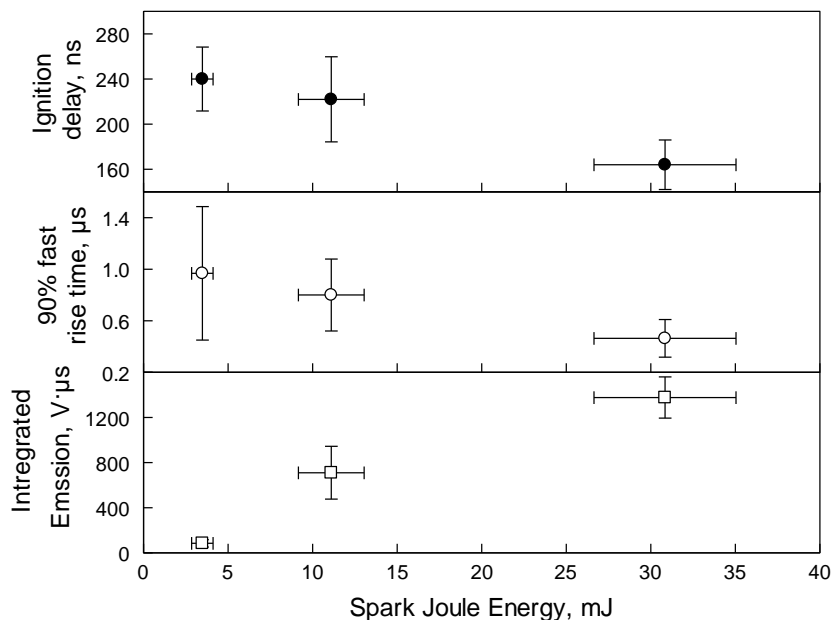


Figure 7.8 Ignition delay, 90% fast rise time and integrated emission as a function of Joule energy for $8\text{Al}\cdot\text{MoO}_3$ powder monolayer ignited by spark.

7.4.2 Shock Ignition of Individual $8\text{Al}\cdot\text{MoO}_3$ Particles

A time-resolved emission transient for the impact velocity of 1.34 km/s is plotted in Figure 7.9. Time zero is the moment of flyer impact measured by PDV with a 5 ns uncertainty. In addition, the flyer plate speed as measured by PDV is shown. Below flyer speeds of ~ 0.5 km/s, there were no obvious signs of thermite emission, but above 0.5 km/s the thermite particles produced intense emission bursts, so 0.5 km/s is taken as an impact velocity ignition threshold. This velocity threshold almost certainly depends on the shock duration as controlled by flyer thickness, and might be lower for thicker flyers.

Above this velocity threshold, the emission transients consist of two bursts, with the first burst lasting ~ 30 ns, followed by a delay of a few hundred ns and a second burst lasting a few μs . As the flyer plate impact velocity was increased, the intensity of both bursts increased. The first, short high amplitude burst and flyer speed are shown with an expanded time scale in the inset in Figure 7.9. The PDV data show the flyer at $t < 0$ moving at constant speed through the vacuum. Abruptly at $t = 0$ the flyer speed declines due to the impact. After this initial decline, there is a ~ 10 ns period of constant velocity when the shock is steady. Following this 10 ns shock, the flyer undergoes a more gradual deceleration over ~ 30 ns. Figure 7.9 shows that the rapid rise of the first emission burst is coincident with the flyer impact. The initial emission burst ends at about the time the flyer comes to rest, or perhaps slightly later and has been discussed in a previous publication [125].

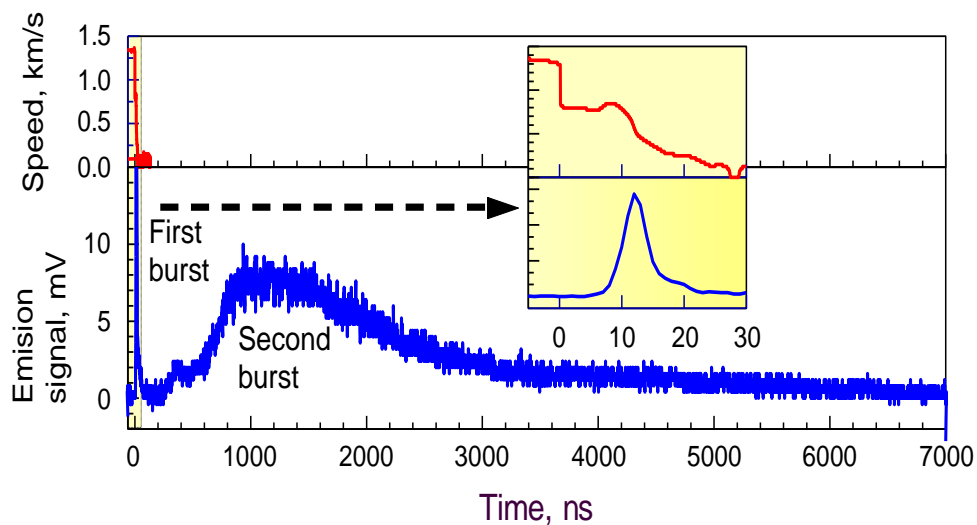


Figure 7.9 Characteristic shock induced emission trace and flyer speed as a function of time for a 10-20 μm 8Al-MoO₃ particle. The impact velocity is 1.34 km/s.

Figure 7.10 shows the emission intensities for three different impact velocities. As the flyer speeds increase, the onset of the second burst moves to shorter time and the rise of the second burst becomes faster. A number of experiments where flyers impacted only glass, or only glass and acrylic cement were conducted. Although there was a detectable amount of emission from these other materials, the emission intensities from impacted thermite particles vastly exceeded that of glass or acrylic cement. The signal from the cement and glass was undetectable during the time the first short burst was observed for the thermite particle. The signal rose and showed a detectable baseline during the time the second burst was observed. The amplitude of the baseline was about 15 times smaller than the signal produced by an ignited thermite particle.

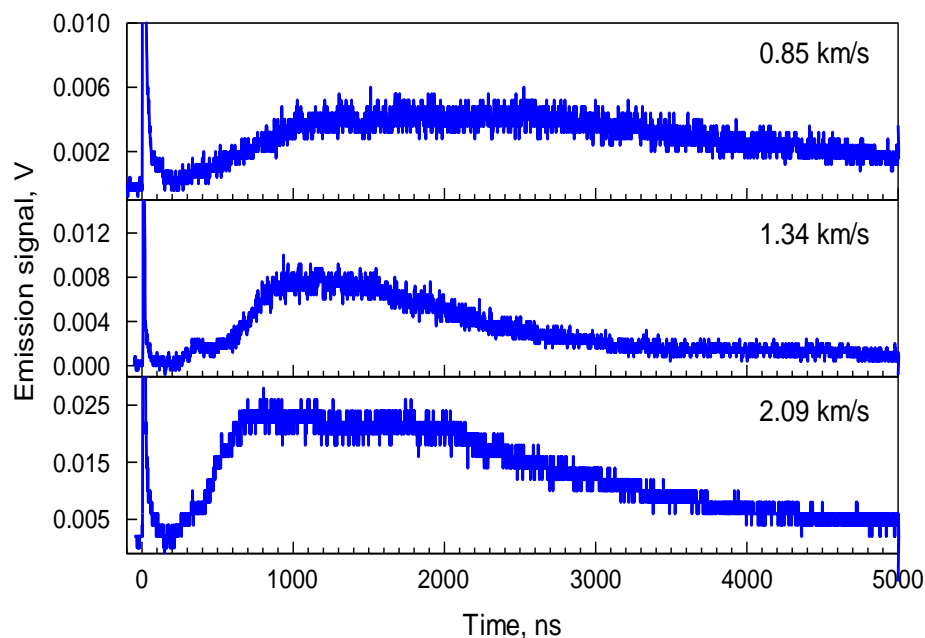


Figure 7.10 Emission traces for 8Al·MoO₃ particles ignited by impacts at different speeds.

In Figure 7.11, the flyer-speed dependence of three properties of the second emission bursts are shown. The time delays between impact and the second bursts (Figure 7.11a), the risetimes (10-90%) of the second bursts (Figure 7.11b), and the integrated areas of the second bursts (Figure 7.11c). The time delay is the time when the second emission burst reaches 10 % of its maximum. The risetime is the 10%-90% rise of the second emission burst.

The ignition delay stay in a narrow range of ca. 150-200 ns for all except the lowest impact energy, for which the delay is much longer. The risetime is consistently decreasing and the integrated signal increasing with the impact energy.

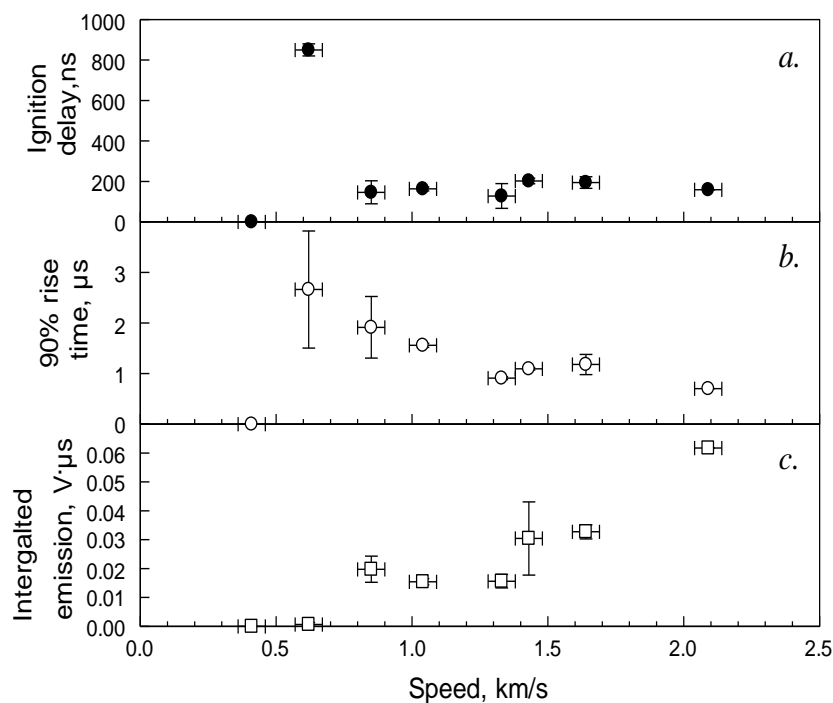


Figure 7.11 Properties of the second emission burst as a function of flyer impact speed. (a) Delay is the time between impact at $t = 0$ and the 10% point of the second burst rise. (b) Rise time is the time for 10%-90% rise of the emission burst. (c) Integral is proportional to the time-integrated emission burst intensity.

7.5 Discussion

7.5.1 Heating Times and Burn Rates

Both initiation techniques considered here result in very fast heating of the nanocomposite thermite particles. A simple estimate discussed above for the shock initiation indicates the heating rate on the order of 10^{10} - 10^{11} K/s. Although the temperature achieved as a result of shock compression is relatively low, as mentioned above, localized hot spots with substantially greater temperature are likely to be formed; for those even greater heating rates are expected. For the spark ignition experiment, the heating rate can be roughly estimated assuming that the emission signal becomes noticeable at 486 nm when at least portions of the material are heated to ca. 1000 K. Because this occurs after the delays varied around 150 – 250 ns (cf. Figure 7.8), the heating rates are estimated to be 0.5 - $1 \cdot 10^{10}$ K/s. For spark ignition, the heating occurs locally because most of the heat release occurs at the points of maximum resistance, i.e., at the contact between the conductive substrate and the particle. For the composite material, it is also possible that the Joule energy is partially released at heterogeneities and material boundaries within the particle. The time required for the temperature to equilibrate within a 10- μ m aluminum particle is estimated to be approximately 1 μ s, which is much longer than any of the ignition delays reported here. An even longer thermal equilibration time is anticipated for the composite particle. Thus, if local hot

spots are formed in the impact or spark initiated particles, it is likely that the ignition is also localized and combustion begins around those hot spots.

A very rapid initiation with the characteristic ignition (and thus local heating) times shorter than the time required for the temperature equilibration within the particle appears to be the principle difference between the present experiments and laser ignition measurements reported for the same material recently [117]. When the particle was heated while passing through a CO₂ laser beam, its heating time was close to 50-70 μs and the heating rates were on the order 10⁶-10⁷ K/s. Thus, the particle temperature was uniform before its ignition and, likely, during its combustion. Remarkably, the burn times reported in Reference [117] are of the order of several ms, much longer than the present data: few μs for the shock ignition and 120 – 200 μs for the spark ignition. Note that in spark ignition experiments multiple particles are ignited and the measured emission time characterizes combustion of the largest particles ignited after the longest delays. In other words, the actual particle combustion times in the spark ignition experiments were likely noticeably shorter than the entire duration of the measured emission signal.

The difference in burn times observed here and in laser ignition experiments is likely associated with the mode of combustion. When laser ignited particles are heated above the melting point of aluminum, it is likely that the nanostructure present in the starting material disappears and the particle burns as a molten drop of aluminum attached

to a solid or molten particle of MoO_3 . However, in present experiments the characteristic ignition times are so short that the nano-structure of the starting material may be preserved. In this case, the reaction will be driven by heterogeneous diffusion of components occurring over a very large surface area existing in the nanocomposite material. The rapid rise in temperature causes this reaction to accelerate dramatically before a finite product layer between Al and MoO_3 is grown, which could lead to the very short reaction times observed. Note also that in the shock ignition experiment, the flyer plate remains in contact with the particle, which could quench the reaction before its completion. Additional work is necessary to fully understand the present combustion mechanisms.

7.5.2 Ignition Delays and Emission Rise Times

In shock ignition, the observed ignition delay corresponds roughly to the timing of transverse decompression waves from the flyer plate [123]. These generate shear forces which might initiate a reaction in $8\text{Al}\cdot\text{MoO}_3$ nanocomposite material. It is intriguing that the ignition delays observed in both shock and spark ignition experiments (cf. Figures 7.8 and 7.11) are close to each other. Thus, these delays may represent an intrinsic time necessary for the heterogeneous reaction to accelerate in this material. This time must be a function of the chemical composition and structure. Experiments with different materials would be useful in clarifying the processes governing the observed ignition delays in both experiments.

Similarly, it is interesting to compare the rise times for the optical signals observed in both experiments. Because the spark cathode and anode spots are reported to be in the range of several μm [126, 127], it is likely that the spark directly heats one particle initially; after that particle ignites, the heating propagates to the rest of the sample. The rapid emission ramp is likely to be indicative of the ignition of the particle directly heated by the spark; the slower rising part of the emission signal characterizes the reaction propagation to the rest of the sample (cf. Figure 7.5). The rise times presented in Figure 7.8 and 7.11 are close to each other, however, they are somewhat shorter for the spark ignition tests. If these times represent ignition of an individual particle, the shorter times for the spark ignition tests can be readily interpreted recalling that the electrostatic discharge remains active during this time, while the shock loading of the particle has been completed. In addition, as noted above, the shock ignited particles remain in contact with the flyer plate, resulting in additional heat losses, although such losses are relatively small for the short times considered.

7.5.3 Ignition Temperatures

An ignition delay reported in Figure 7.8 can be used to estimate the initial particle temperature for the spark ignition tests. This estimate must assume the homogeneous particle heating; thus the temperatures achieved in the hot spots are expected to be higher. The temperature was estimated considering an adiabatic Joule heating of a particle with diameter equal to the mean volumetric particle size of $21.8 \mu\text{m}$ during the 150-240 ns

ignition delay. The real-time recorded spark current signal was used, and the powder impedance was assumed to remain constant. The results of this estimate are shown in Figure 7.12. Estimated temperatures compare well with the range of 800-900 K, for which ignition of the same $8\text{Al}\cdot\text{MoO}_3$ powder is observed when it is coated on an electrically heated wire [40, 41]. Based on this estimate, it is reasonable to expect that such heterogeneous reactions as considered in the multi-step ignition model for a similar nanocomposite thermite [33] are also active in the present experiments. However, because of the lack of pre-ignition reactions, Al and MoO_3 remain in nearly intimate contact, and the rate of these reactions can be substantially increased.

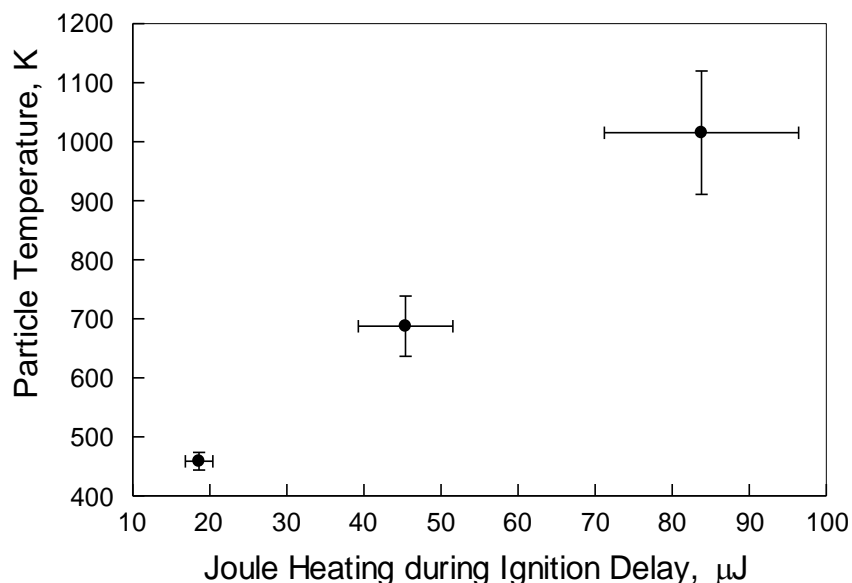


Figure 7.12 Estimated temperature to which the volumetric mean particle size is heated by the spark current during the delay time for $8\text{Al}\cdot\text{MoO}_3$ powder monolayer.

7.6 Conclusions

Micron-sized, nanocomposite $8\text{Al}\cdot\text{MoO}_3$ thermite particles were ignited using both shock compression and spark ignition techniques with very high heating rates on the order of 10^9 - 10^{11} K/s. These ignition methods result in a very fast combustion with characteristic burn times reduced by 1 – 3 orders of magnitude compared to the burn times measured previously for the same material ignited in the CO_2 laser beam [117], where it was heated at a much lower rate of about 10^6 - 10^7 K/s. It is proposed that the greater burn rates achieved after a very rapid ignition are associated with the preserved nano-structure and respectively very high heterogeneous reaction rate achieved at the high combustion temperatures.

Ignition delays observed in both shock and spark ignition experiments are close to each other and vary in the range of 120 – 200 ns. The times of characteristic rapid increase in the optical emission of the ignited particles are also close to each other for the two experiments; however, these times are somewhat shorter (less than one μs) for the spark ignition tests compared to few μs observed for the shock initiated particles. The spark-ignited nanocomposite thermite particles are observed to be ejected from the substrate at the speeds approaching the speed of sound in surrounding air. The mechanisms of processes responsible for the measured ignition delays, emission rise times, combustion duration, and particle ejection by the spark will be investigated in future experiments, in which the range of materials tested will be expanded.

CHAPTER 8

CONCLUSIONS

Nanocomposite thermites ignited in vacuum using an electrically heated filament generated both pressure and optical emission pulses. These measured pressure pulse started prior to the detected optical emission. The delay of optical pulse compared to the pressure pulse increased at higher heating rates. No pressure or optical emission was detected in similar experiments with reference inert nanocomposite samples, in which aluminum was replaced with copper. Pressure pulse and associated gas release detected in experiments with nanocomposite thermites heated in vacuum were assigned to oxygen generation by decomposing metal oxides for $2\text{Al}\cdot 3\text{CuO}$, $4\text{Al}\cdot \text{Fe}_2\text{O}_3$, and $8\text{Al}\cdot \text{MoO}_3$. However, this assignment could not be made unambiguously for $2.35\text{Al}\cdot \text{Bi}_2\text{O}_3$. The oxygen release prior to ignition was suggested to be caused by destabilization of the metal oxides partially reduced during a relatively slow, low-temperature redox reaction described by the Cabrera-Mott kinetics. This showed the importance of low-temperature redox reactions, despite their relatively small heat release. The partially reduced oxide phase decomposed upon heating with a corresponding gas release that altered the thermal properties of the powder coating on the heated filament. This, in turn, reduced the efficiency of the heat exchange between the powder and filament, enabling the powder's thermal runaway and ignition.

A recently developed multistep reaction model for the Al-CuO nanocomposite powders was shown to remain valid for powders prepared with different milling conditions and, therefore, characterized by different Al/CuO ratios within the composite material. The experiments showed that in the nanocomposite Al-CuO powders prepared by ARM, the CuO inclusion size remains nearly unchanged at different milling times. It was also observed that the mixing between Al and CuO in the nanocomposite particles improves as the milling time gets longer, approaching the nominal composition implied by the balance of the starting Al and CuO powders.

Low temperature, exothermic reactions in the Al/MoO₃ nanocomposite thermites prepared by arrested reactive milling were also successfully described by Cabrera-Mott formalism, similar to the reactions in nanocomposite Al/CuO nanocomposite powders considered in earlier work. To interpret the experiments, it was necessary to quantitatively account for a small weight loss observed during the sample heating and assigned to its dehydration. In addition, to describe the heat flow observed in DSC experiments to increase continuously from 400 to 600 K, it was necessary to assume that the activation energy employed by the Cabrera-Mott model experiences a stepwise increase at 400 K. Thirteen experimental curves were used to recover six unknown Cabrera-Mott model parameters for 8Al·MoO₃. The resulting model described satisfactorily thermo-analytical experiments with heating rates varied over three orders of

magnitude as well as a set of isothermal micro-calorimetry measurements at different temperatures.

Experimental data from ignition of n-thermites using electric spark and shock compression are expected to be useful for development and validation of detailed quantitative models describing ignition of nanocomposite thermites by different stimuli. In particular, the comprehensive models are expected to describe quantitatively the observed effects of powder composition, aging, and presence of inert diluent in the powder blends on the measured ignition delays.

For ESD-induced ignition, two regimes were observed for nanocomposite thermites. Powder placed in monolayers ignited immediately; ignition resulted in individual burning particles ejected from the sample. Powders placed in thicker layers ignited after a delay and produced burning powder cloud. The same cloud ignition was observed in both air and argon at 1 atm. In vacuum, only individual particle streaks were observed for monolayers as well as for thicker powder samples. Convection substantially affected the temperature profile in the powder sample prior to its ignition, causing nearly simultaneous heating of a group of particles eventually producing a burning powder cloud.

The ignition delay for the powder cloud combustion did not depend on the ESD energy, but was affected by the composition of the nanocomposite thermite, its aging, and presence of a diluent metal powder. It was also observed that the ignition delays were

close to respective delays between onsets of pressure and optical emission pulses registered during ignition of the nanocomposite powders coated on an electrically heated filament. It was suggested that the spark pre-heated particles in a thick powder layer to a threshold temperature, at which the heterogeneous pre-ignition reaction began. This reaction could be accelerated by combined Joule heat and electric current effects destabilizing the oxidizer, increasing the number of mobile oxygen ions available for reaction. Eventually, the rate of reaction accelerated to cause formation of gaseous products and particle ejection, resulting in the observed cloud ignition.

Micron-sized, nanocomposite $8\text{Al}\cdot\text{MoO}_3$ thermite particles were ignited using both shock compression and spark ignition techniques with very high heating rates on the order of 10^9 - 10^{11} K/s. These ignition methods result in a very fast combustion with characteristic burn times reduced by 1 – 3 orders of magnitude compared to the burn times measured previously for the same material ignited in the CO_2 laser beam [117], where it was heated at a much lower rate of about 10^6 - 10^7 K/s. It was proposed that the greater burn rates achieved after a very rapid ignition were associated with the preserved nano-structure and respectively very high heterogeneous reaction rate achieved at the high combustion temperatures. Ignition delays observed in both shock and spark ignition experiments were close to each other and varied in the range of 120 – 200 ns. The times of characteristic rapid increase in the optical emission of the ignited particles were also close to each other for the two experiments; however, these times were somewhat shorter

(less than one μs) for the spark ignition tests compared to few μs observed for the shock initiated particles.

APPENDIX A

Al-Bi₂O₃ NANOCOMPOSITES THERMITES PREPARED USING DIFFERENT MILLING TIMES

In this appendix, heated filament ignition and microcalorimetry results for 2.35Al-Bi₂O₃ n-thermite powders milled for 90, 150 and 180 minutes respectively, are presented.

Milling parameters are the same as used in Chapter 2.

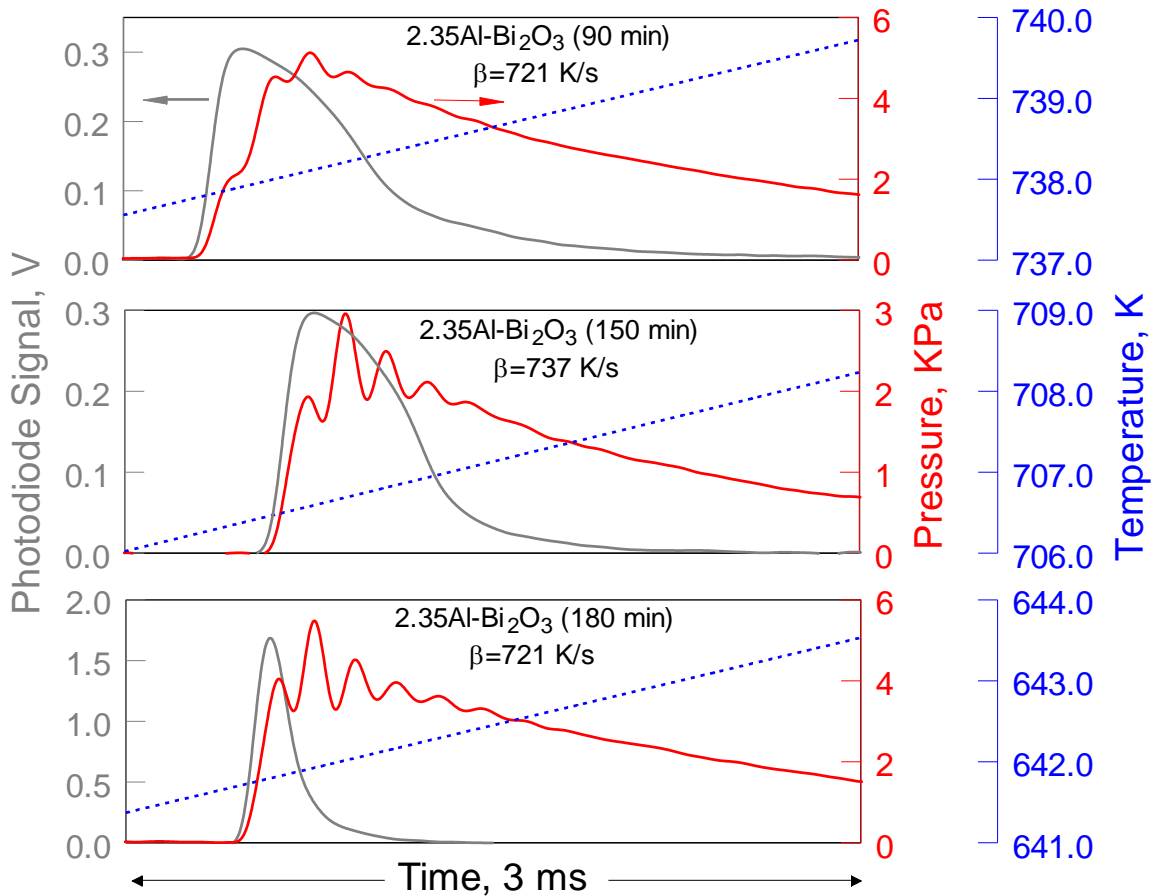


Figure A.1 Photodiode signal and pressure traces recorded at a low pre-set heating rate for 2.35Al-Bi₂O₃ prepared at different milling times. Temperature ramp is shown by a straight dotted line. Specific heating rate, β , is shown for each set of traces.

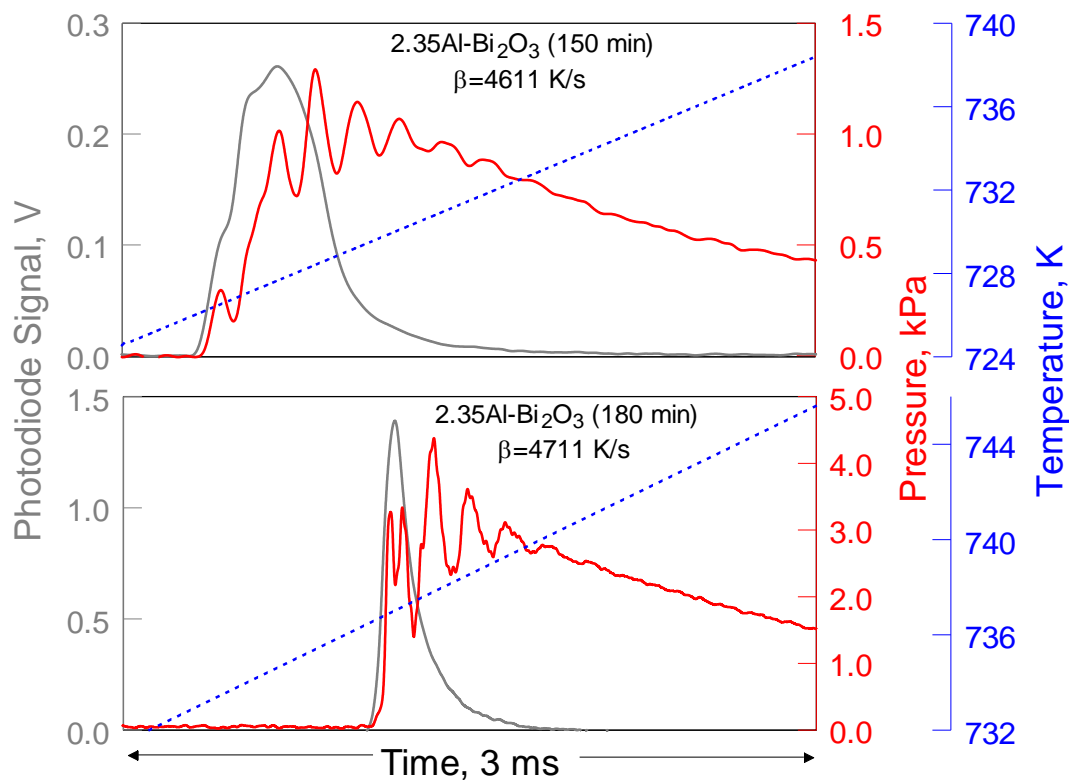


Figure A.2 Photodiode signal and pressure traces recorded at a high pre-set heating rate for 2.35Al-Bi₂O₃ prepared at different milling times. Temperature ramp is shown by a straight dotted line. Specific heating rate, β , is shown for each set of traces.

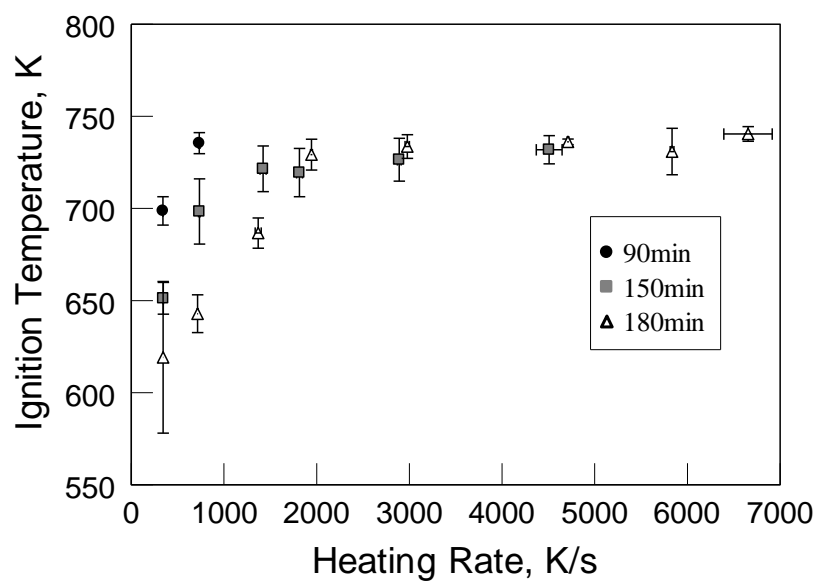


Figure A.3 Ignition temperature of 2.35Al-Bi₂O₃ n-thermite powders milled for different times as a function of the heating rate.

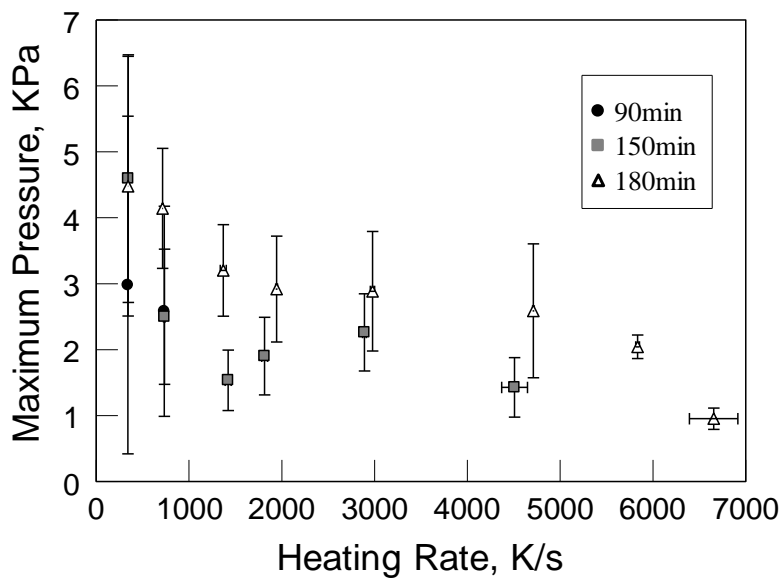


Figure A.4 Maximum pressure of 2.35Al-Bi₂O₃ n-thermite powders milled for different times as a function of the heating rate.

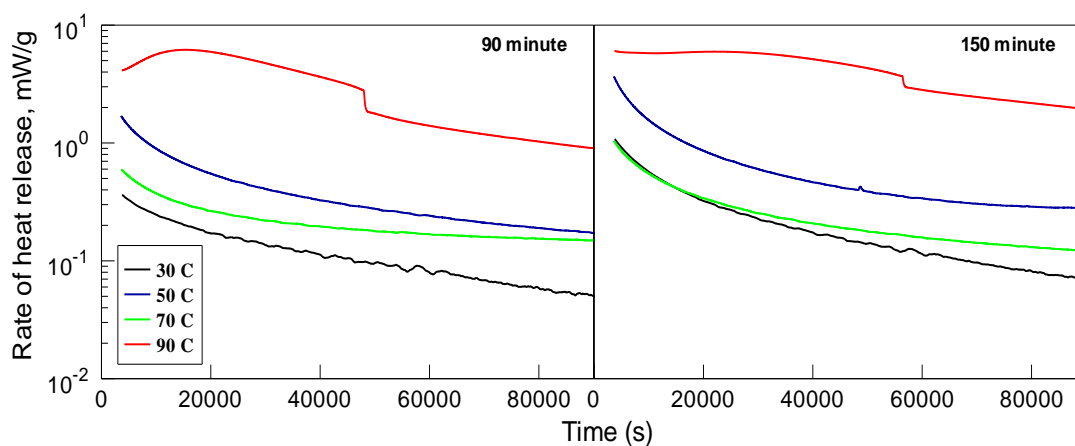


Figure A.5 Isothermal TAM III measurements for nanocomposite 2.35Al-Bi₂O₃ n-thermite powders milled for different times.

APPENDIX B

CHARACTERIZATION OF AGED 8Al-MoO₃ NANOCOMPOSITES THERMITES

In this appendix, the characterization results of 8Al-MoO₃ n-thermite powder aged for six months are presented. Milling parameters are the same as used in Chapter 2.

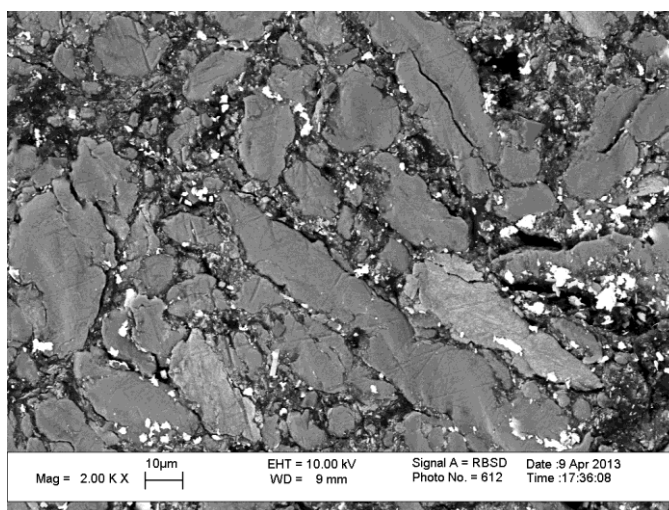


Figure B.1 SEM image of aged 8Al-MoO₃ used for EDX composition analysis based on randomly selected areas.

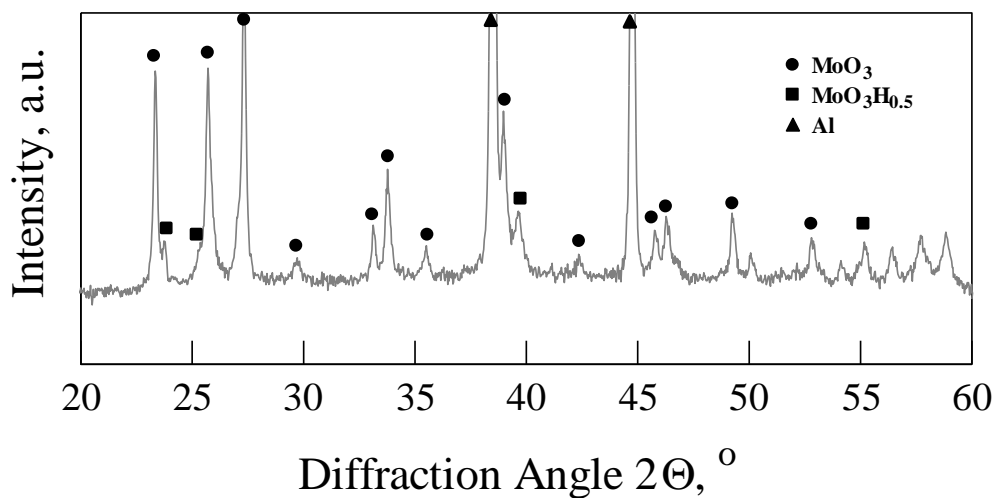


Figure B.2 XRD patterns of aged 8Al-MoO₃ nanocomposite powder.

Table A.1 Normalized Compositions of Random Areas in Figure B.1 in Atomic %, Determined by Standard-free EDX Analysis

Spectrum	Al	Mo
1	98.91	1.09
2	95.20	4.80
3	97.81	2.19
4	96.09	3.91
5	97.29	2.71
6	98.47	1.53
7	96.44	3.56
8	94.98	5.02
9	80.87	19.13
10	91.37	8.63

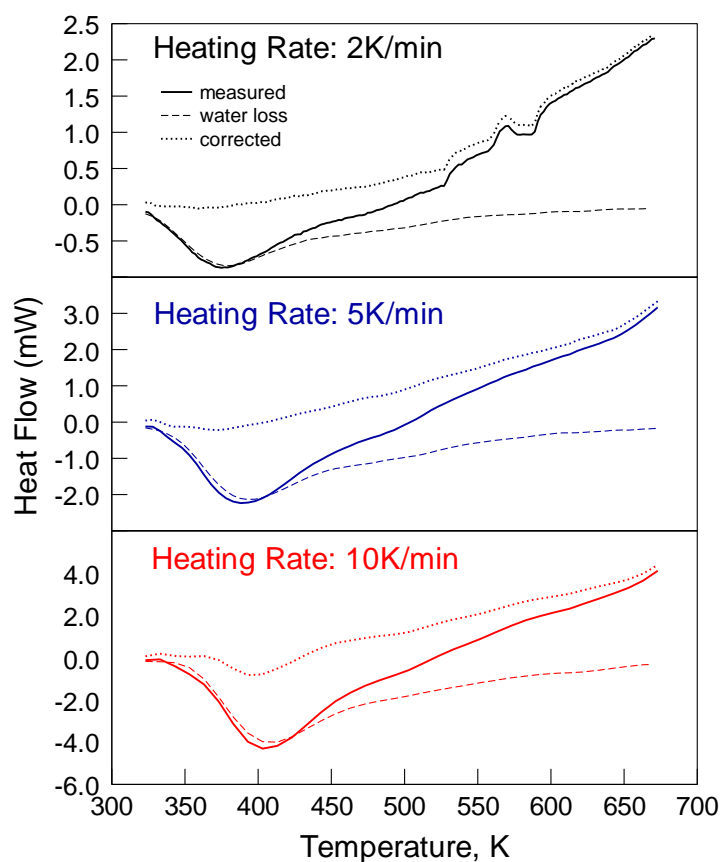


Figure B.3 Corrected and measured DSC heat flow data of aged 8Al-MoO₃ powder accounting for dehydration at different heating rates.

APPENDIX C

ADDITIONAL DATA FOR DETERMINATION OF 8Al-MoO₃ KINETIC MODEL PARAMETERS

Additional results are shown in this appendix for selection of model parameters derived for 8Al-MoO₃ in Chapter 5. Table 5.1 shows a summary of parameters for 8Al-MoO₃ that yielded the best agreement between experiment and simulation. Additional data presented here include root mean squared error (RMSE) analysis, parametric plots and summary of kinetic parameters for different assumed spherical inclusion sizes. Further details describing the methodology of fitting can be found elsewhere [31].

Table C.1 Values of Kinetic Constants or their Ranges Obtained from Processing TAM III and DSC Measurements for an Inclusion Size of 20 nm

	Average	Range	
k_0 , nm/s	6.5×10^{-5}	7.3×10^{-6}	5.5×10^{-4}
E_1 , J/mol	26,000	20,000	32,000
E_2 , 10^{-22} J-nm	$-39 + 0.14T$	$-18 + 0.07T$	$-60 + 0.21T$

Table C.2 Values of Kinetic Constants or their Ranges Obtained from Processing TAM III and DSC Measurements for an Inclusion Size of 100 nm

	Average	Range	
k_0 , nm/s	5.0×10^{-3}	4.3×10^{-5}	0.01
E_1 , J/mol	26,500	20,000	33,000
E_2 , 10^{-22} J-nm	$-205 + 0.77T$	$-317 + 1.14T$	$-93 + 0.40T$

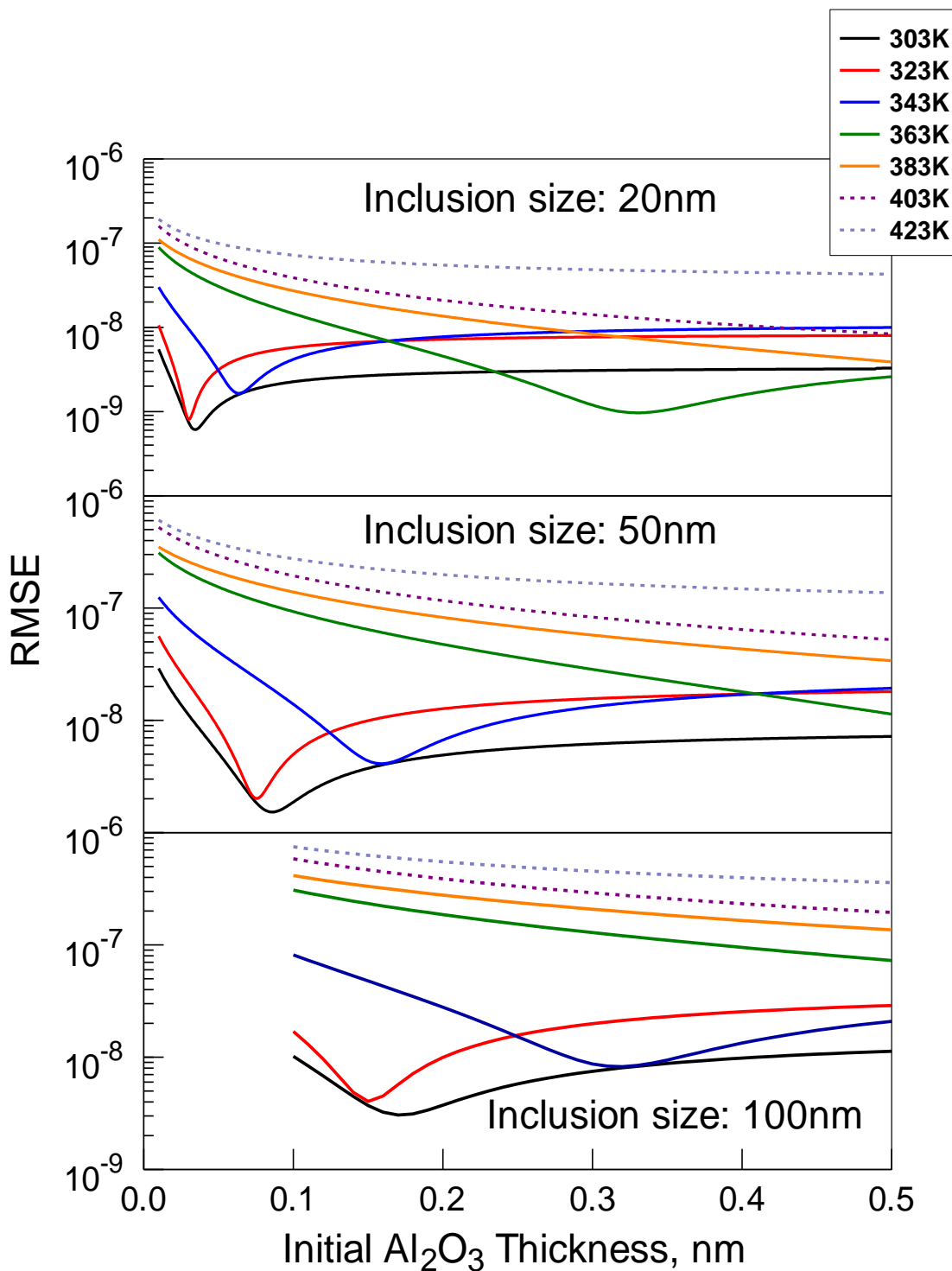


Figure C.1 Root mean squared error of fit as a function of aluminum oxide initial thickness for different inclusion sizes.

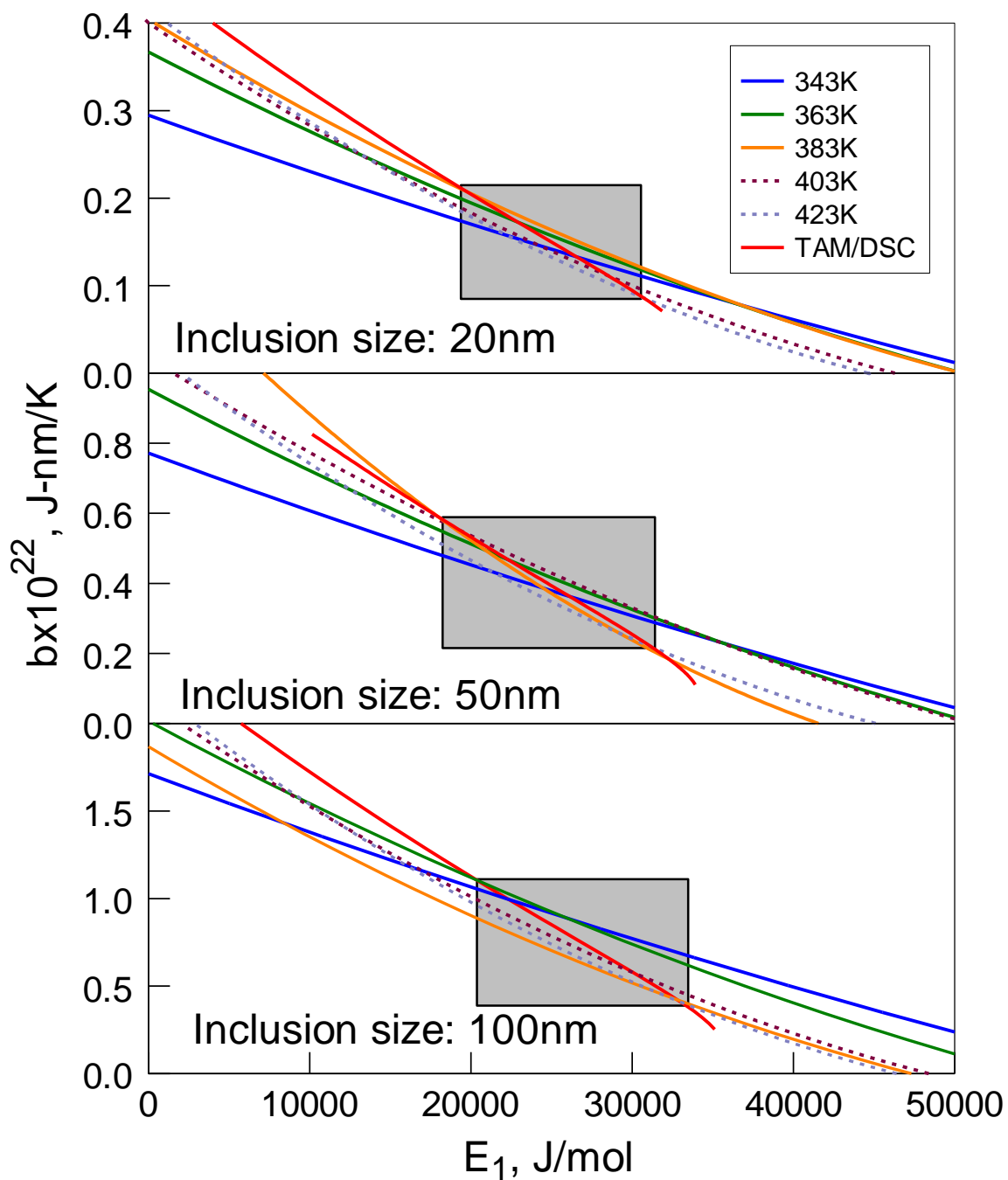


Figure C.2 Parametric plots obtained by fitting DSC and TAM experimental curves for different inclusion sizes.

An inclusion of 50 nm was selected as the most suitable inclusion size in Chapter 5, based on the minimum relative difference (RD) obtained using the highlighted regions of Figure C.2. This was calculated as $RD = \frac{Max.value - Min.value}{Average}$ and averaged over the entire highlighted region of Figure C.2. This is summarized in Figure C.3 for each inclusion size.

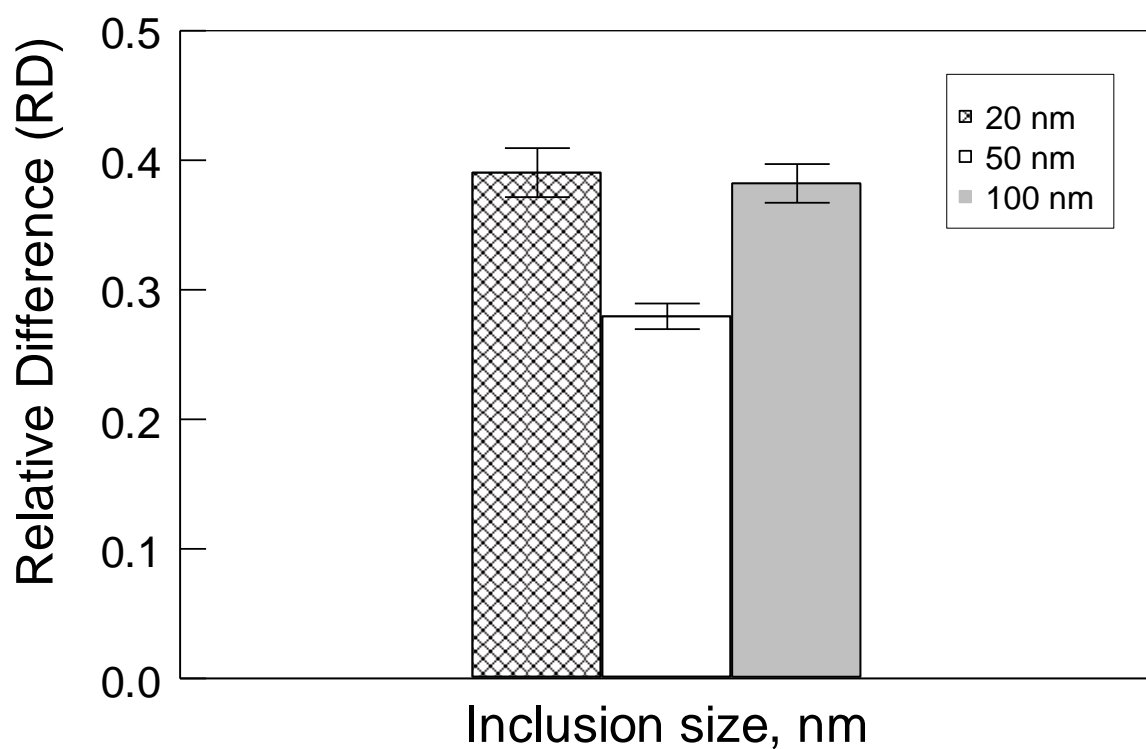


Figure C.3 Relative difference averaged over the highlighted region of Figure C.2 for different $8Al-MoO_3$ inclusion sizes.

APPENDIX D

IGNITION OF THIN LAYERS OF NANOCOMPOSITE THERMITE POWDERS BY AN ELECTRIC SPARK

Ignition by electric spark was studied experimentally for $2\text{Al}\cdot 3\text{CuO}$, $2.35\text{Al}\cdot \text{Bi}_2\text{O}_3$, $4\text{Al}\cdot \text{Fe}_2\text{O}_3$, and $2\text{Al}\cdot \text{MoO}_3$ nanocomposite thermite (n-thermite) powders prepared using arrested reactive milling (ARM). Specifically, monolayers of the prepared powder were placed on a conductive substrate and heated in air by a pulsed electro-static discharge at varying applied energy. The heating rates achieved were estimated to be in the range of 10^9 - 10^{10} K/s. Time-dependent optical emission produced by the ignited material was monitored and recorded. These traces were baseline-corrected by subtracting the signal recorded with no sample loaded and normalized by the peak of these blank signals.

Typical single particle images of ignited monolayers were shown in Chapters 6 and 7. Ignition delays, burn time and temperature of the ignited particles were determined based on optical emissions collected at three different wavelengths (700, 800 and 900 nm).

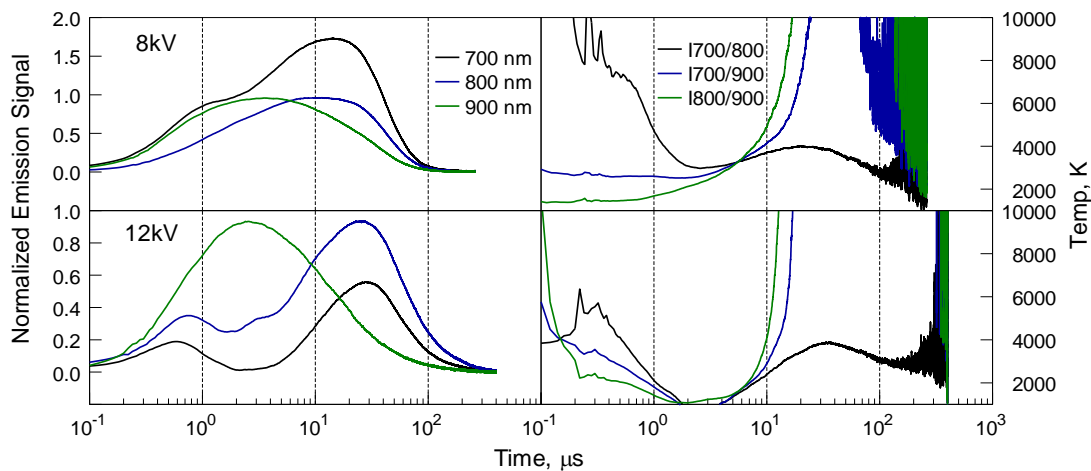


Figure D.1 Typical optical emission traces with the corresponding temperature estimates for burning particles of $2.35\text{Al}\cdot\text{Bi}_2\text{O}_3$ monolayers ignited by 8 kV and 12kV ESD.

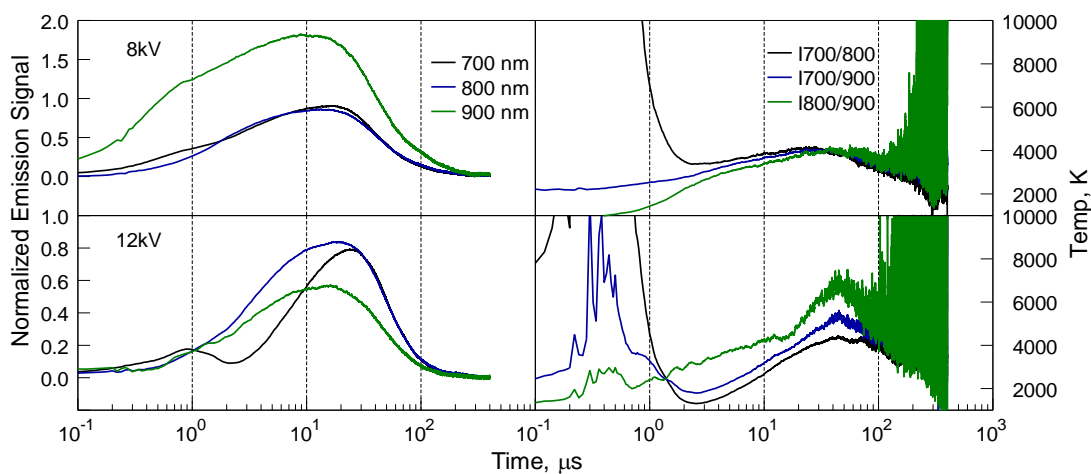


Figure D.2 Typical optical emission traces with the corresponding temperature estimates for burning particles of $2\text{Al}\cdot 3\text{CuO}$ monolayers ignited by 8 kV and 12kV ESD.

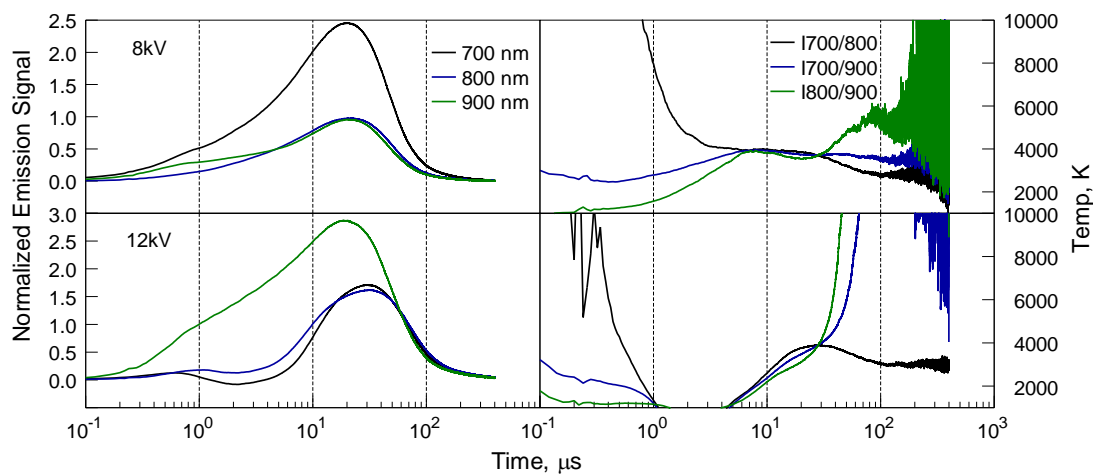


Figure D.3 Typical optical emission traces with the corresponding temperature estimates for burning particles of $2\text{Al}\cdot\text{Fe}_2\text{O}_3$ monolayers ignited by 8 kV and 12kV ESD.

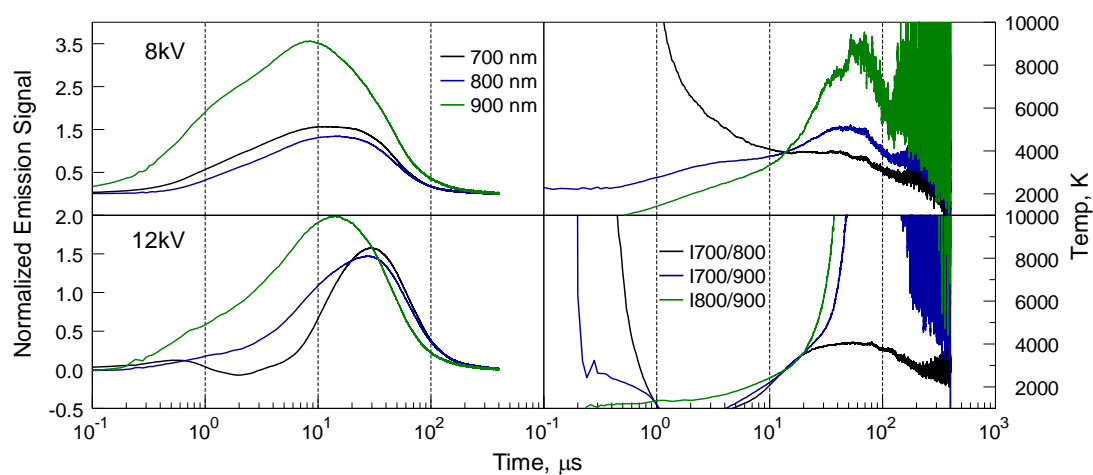


Figure D.4 Typical optical emission traces with the corresponding temperature estimates for burning particles of $2\text{Al}\cdot\text{MoO}_3$ monolayers ignited by 8 kV and 12kV ESD.

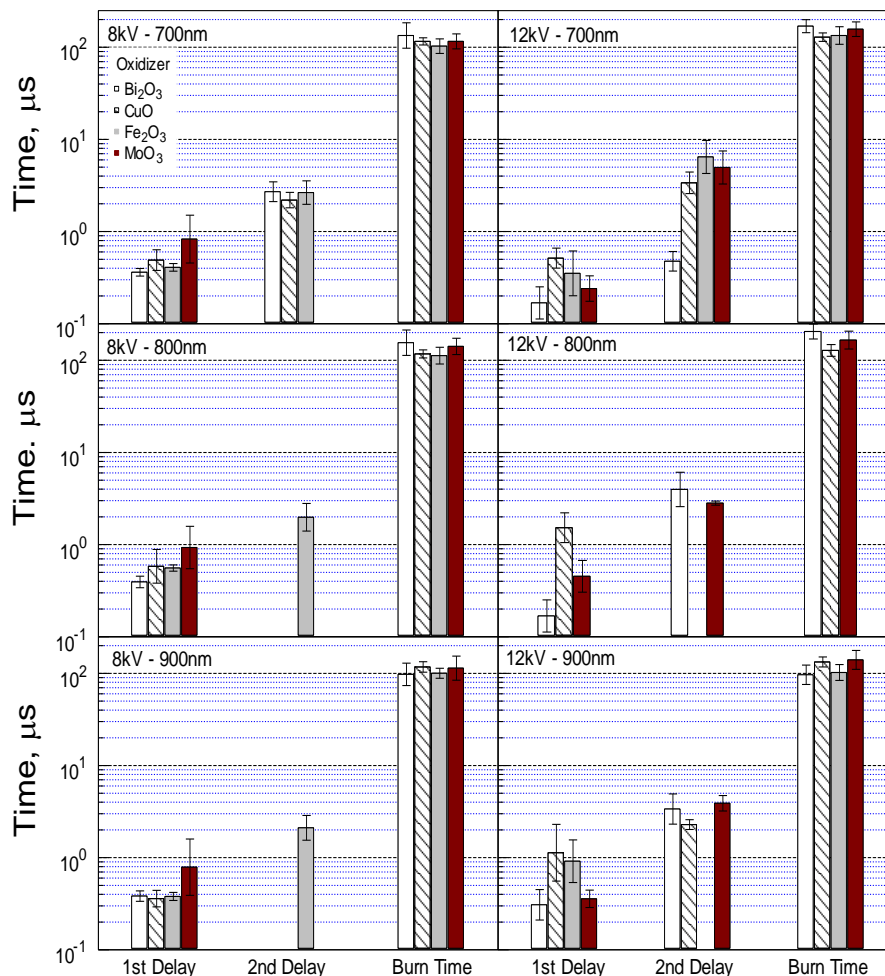


Figure D.5 Summary of ignition delays and burn time for all materials at different emission wavelengths and applied voltages.

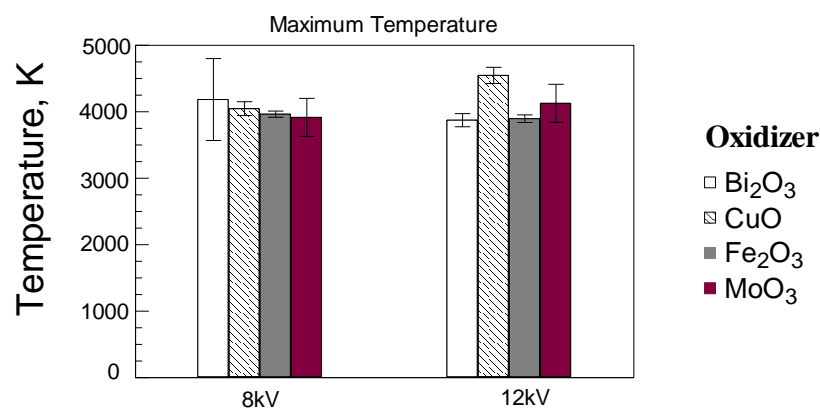


Figure D.6 Summary of maximum temperature for all materials at different applied voltages based on intensity ratio of 700nm/800nm wavelengths.

REFERENCES

- [1] X. Y. Yuan, C. B. Zhan, H. B. Jin, and K. X. Chen, "Novel Method of Thermite Welding," *Science and Technology of Welding and Joining*, vol. 15, pp. 54-58, 2010.
- [2] C. Meriç and T. Engez, "Understanding the Thermite Welding Process: The Metallurgical Specifications and Hardness Profile of Thermite Welds were Examined to Better Understand this Process Commonly Used in the Railroad Industry," *Welding Journal (Miami, Fla)*, vol. 78, pp. 33-36, 1999.
- [3] K. Gibran, "Furnace for Controllable Combustion of Thermite," *United States Patent 5086720 A*, 1992.
- [4] P. Dupiano, D. Stamatis, and E. L. Dreizin, "Hydrogen Production by Reacting Water with Mechanically Milled Composite Aluminum-metal Oxide Powders," *International Journal of Hydrogen Energy*, vol. 36, pp. 4781-4791, 2011.
- [5] E. L. Dreizin, "Metal-based Reactive Nanomaterials," *Progress in Energy and Combustion Science*, vol. 35, pp. 141-167, 2009.
- [6] S. F. Son, B. W. Asay, T. J. Foley, R. A. Yetter, M. H. Wu, and G. A. Risha, "Combustion of Nanoscale Al/MoO₃ Thermite in Microchannels," *Journal of Propulsion and Power*, vol. 23, pp. 715-721, 2007.
- [7] S. F. Son, R. Yetter, and V. Yang, "Introduction: Nanoscale Composite Energetic Materials," *Journal of Propulsion and Power*, vol. 23, pp. 643-644, 2007.
- [8] M. F. Gogulya, M. N. Makhov, M. A. Brazhnikov, A. Y. Dolgoborodov, V. I. Arkhipov, A. N. Zhigach, *et al.*, "Explosive Characteristics of Aluminized HMX-based Nanocomposites," *Combustion, Explosion, and Shock Waves*, vol. 44, pp. 198-212, 2008.
- [9] B. J. Henz, T. Hawa, and M. R. Zachariah, "Atomistic Simulation of the Aluminum Nanoparticle Oxidation Mechanism," in *48th AIAA Aerospace Sciences Meeting*, Orlando, FL, pp. 0336, 2010.
- [10] K. K. Kuo, G. A. Risha, B. J. Evans, and E. Boyer, "Potential Usage of Energetic Nano-sized Powders for Combustion and Rocket Propulsion," in *MRS Online Proceedings Library 800*, Boston, MA., pp. 3-14, 2003.

- [11] B. W. Asay, J. R. Busse, B. S. Jorgensen, B. Bockmon, M. Pantoya, and S. F. Son, Reaction Propagation Physics of Al/MoO₃ Nanocomposite Thermites, *Proceedings of the 28th International Pyrotechnics Society Pyrotechnics Seminar*, Adelaide, Australia, 2001.
- [12] M. L. Pantoya and J. J. Granier, "Combustion Behavior of Highly Energetic Thermites: Nano versus Micron Composites," *Propellants, Explosives, Pyrotechnics*, vol. 30, pp. 53-62, 2005.
- [13] B. S. Bockmon, M. L. Pantoya, S. F. Son, B. W. Asay, and J. T. Mang, "Combustion Velocities and Propagation Mechanisms of Metastable Interstitial Composites," *Journal of Applied Physics*, vol. 98, pp. 064903-064903-7, 2005.
- [14] V. I. Levitas, B. W. Asay, S. F. Son, and M. Pantoya, "Melt Dispersion Mechanism for Fast Reaction of Nanothermites," *Applied Physics Letters*, vol. 89, pp. 071909-3, 2006.
- [15] L. L. Wang, Z. A. Munir, and Y. M. Maximov, "Thermite Reactions: Their Utilization in the Synthesis and Processing of Materials," *Journal of Materials Science*, vol. 28, pp. 3693-3708, 1993.
- [16] R.-H. Fan, H.-L. Lü, K.-N. Sun, W.-X. Wang, and X.-B. Yi, "Kinetics of Thermite Reaction in Al-Fe₂O₃ system," *Thermochimica Acta*, vol. 440, pp. 129-131, 2006.
- [17] K. B. Plantier, M. L. Pantoya, and A. E. Gash, "Combustion Wave Speeds of Nanocomposite Al/Fe₂O₃: the Effects of Fe₂O₃ Particle Synthesis Technique," *Combustion and Flame*, vol. 140, pp. 299-309, 2005.
- [18] J. Sun, M. L. Pantoya, and S. L. Simon, "Dependence of Size and Size Distribution on Reactivity of Aluminum Nanoparticles in Reactions with Oxygen and MoO₃," *Thermochimica Acta*, vol. 444, pp. 117-127, 2006.
- [19] A. E. Gash, T. M. Tillotson, J. H. Satcher, J. F. Poco, L. W. Hrubesh, and R. L. Simpson, "Use of Epoxides in the Sol-gel Synthesis of Porous Iron(III) Oxide Monoliths from Fe(III) Salts," *Chemistry of Materials*, vol. 13, pp. 999-1007, 2001.
- [20] A. E. Gash, T. M. Tillotson, J. H. Satcher Jr, L. W. Hrubesh, and R. L. Simpson, "New Sol-gel Synthetic Route to Transition and Main-group Metal Oxide Aerogels Using Inorganic Salt Precursors," *Journal of Non-Crystalline Solids*, vol. 285, pp. 22-28, 2001.

- [21] T. M. Tillotson, A. E. Gash, R. L. Simpson, L. W. Hrubesh, J. H. Satcher Jr, and J. F. Poco, "Nanostructured Energetic Materials Using Sol-gel Methodologies," *Journal of Non-Crystalline Solids*, vol. 285, pp. 338-345, 2001.
- [22] S. Apperson, S. Bhattacharya, Y. Gao, S. Senthil, S. Hasan, M. Hossain, *et al.*, "On-Chip Initiation and Burn Rate Measurements of Thermitic Energetic Reactions," *MRS Online Proceedings Library*, vol. 896, 2005.
- [23] S. Apperson, R. V. Shende, S. Subramanian, D. Tappmeyer, S. Gangopadhyay, Z. Chen, *et al.*, "Generation of Fast Propagating Combustion and Shock Waves with Copper Oxide/Aluminum Nanothermite Composites," *Applied Physics Letters*, vol. 91, pp. 243109-3, 2007.
- [24] S. C. Gangopadhyay, R. Shende, S. Subramanian, K. Gangopadhyay, S. Hasan, "Ordered Nanoenergetic Composites and Synthesis Method," *United States Patent 7927437 B2*, 2007.
- [25] J. Barbee, Troy W. and T. Weihs, "Ignitable Heterogeneous Stratified Structure for the Propagation of an Internal Exothermic Chemical Reaction Along an Expanding Wavefront and Method of Making Same," *United States Patent 5538795A*, 1996.
- [26] A. Duckham, S. J. Spey, J. Wang, M. E. Reiss, T. P. Weihs, E. Besnoin, *et al.*, "Reactive Nanostructured Foil Used as a Heat Source for Joining Titanium," *Journal of Applied Physics*, vol. 96, pp. 2336-2342, 2004.
- [27] E. L. Dreizin and M. Schoenitz, "Nano-composite Energetic Powders Prepared by Arrested Reactive Milling," *United States Patent 7524355 B2*, 2009.
- [28] E. L. Dreizin, M. Schoenitz, Y. L. Shoshin, M. A. Trunov, S. Umbrajkar, T. S. Ward, *et al.*, "Highly-Energetic Nanocomposite Powders Produced by Arrested Reactive Milling," *Internationale Jahrestagung*, pp. P 138, 2005.
- [29] M. Schoenitz, T. Ward, and E. L. Dreizin, "Preparation of Energetic Metastable Nano-Composite Materials by Arrested Reactive Milling," *MRS Online Proceedings Library*, vol. 800, 2003.
- [30] M. Schoenitz, T. S. Ward, and E. L. Dreizin, "Fully Dense Nano-composite Energetic Powders Prepared by Arrested Reactive Milling," *Proceedings of the Combustion Institute*, vol. 30, pp. 2071-2078, 2005.

- [31] A. Ermoline, D. Stamatis, and E. L. Dreizin, "Low-temperature Exothermic Reactions in Fully Dense Al-CuO Nanocomposite Powders," *Thermochimica Acta*, vol. 527, pp. 52-58, 2012.
- [32] A. Ermoline, M. Schoenitz, and E. L. Dreizin, "Reactions Leading to Ignition in Fully Dense Nanocomposite Al-oxide Systems," *Combustion and Flame*, vol. 158, pp. 1076-1083, 2011.
- [33] D. Stamatis, A. Ermoline, and E. L. Dreizin, "A Multi-step Reaction Model for Ignition of Fully-dense Al-CuO Nanocomposite Powders," *Combustion Theory and Modelling*, vol. 16, pp. 1011-1028, 2012.
- [34] M. A. Trunov, M. Schoenitz, and E. L. Dreizin, "Effect of Polymorphic Phase Transformations in Alumina Layer on Ignition of Aluminium particles," *Combustion Theory and Modelling*, vol. 10, pp. 603-623, 2006.
- [35] M. Schoenitz, S. Umbrajkar, and E. L. Dreizin, "Kinetic Analysis of Thermite Reactions in Al-MoO₃ Nanocomposites," *Journal of Propulsion and Power*, vol. 23, pp. 683-687, 2007.
- [36] S. M. Umbrajkar, S. Seshadri, M. Schoenitz, V. K. Hoffmann, and E. L. Dreizin, "Aluminum-rich Al-MoO₃ Nanocomposite Powders Prepared by Arrested Reactive Milling," *Journal of Propulsion and Power*, vol. 24, pp. 192-198, 2008.
- [37] S. M. Umbrajkar, M. Schoenitz, and E. L. Dreizin, "Exothermic Reactions in Al-CuO Nanocomposites," *Thermochimica Acta*, vol. 451, pp. 34-43, 2006.
- [38] P. R. Santhanam and E. L. Dreizin, "Predicting Conditions for Scaled-up Manufacturing of Materials Prepared by Ball Milling," *Powder Technology*, vol. 221, pp. 403-411, 2012.
- [39] A. Ermoline and E. L. Dreizin, "Equations for the Cabrera–Mott Kinetics of Oxidation for Spherical Nanoparticles," *Chemical Physics Letters*, vol. 505, pp. 47-50, 2011.
- [40] R. A. Williams, J. V. Patel, A. Ermoline, M. Schoenitz, and E. L. Dreizin, "Correlation of Optical Emission and Pressure Generated Upon Ignition of Fully-dense Nanocomposite Thermite Powders," *Combustion and Flame*, vol. 160, pp. 734-741, 2013.
- [41] R. A. Williams, M. Schoenitz, A. Ermoline, and E. L. Dreizin, "On Gas Release By Thermally-Initiated Fully-Dense 2Al-3CuO Nanocomposite Powder,"

International Journal of Energetic Materials and Chemical Propulsion, vol. 11, pp. 275-292, 2013.

- [42] R. A. Williams, M. Schoenitz, and E. L. Dreizin, "Validation of the Thermal Oxidation Model for Al/CuO Nanocomposite Powder," *Combustion Science and Technology*, vol. 186, pp. 47-67, 2014.
- [43] R. A. Yetter, G. A. Risha, and S. F. Son, "Metal Particle Combustion and Nanotechnology," in *Proceedings of the Combustion Institute*, Montreal, QC, pp. 1819-1838, 2009.
- [44] P. E. Specht, N. N. Thadhani, A. K. Stover, and T. P. Weihs, "Meso-scale Computational Study of the Shock-compression of Cold-rolled Ni-Al Laminates," in *Proceedings of the American Physical Society Topical Group on Shock Compression of Condensed Matter*, Nashville, TN, pp. 57-60, 2009.
- [45] E. Besnoin, S. Cerutti, O. M. Knio, and T. P. Weihs, "Effect of Reactant and Product Melting on Self-propagating Reactions in Multilayer Foils," *Journal of Applied Physics*, vol. 92, pp. 5474, 2002.
- [46] A. B. Mann, A. J. Gavens, M. E. Reiss, D. Van Heerden, G. Bao, and T. P. Weihs, "Modeling and Characterizing the Propagation Velocity of Exothermic Reactions in Multilayer Foils," *Journal of Applied Physics*, vol. 82, pp. 1178-1188, 1997.
- [47] J. Mei, R. D. Halldearn, and P. Xiao, "Mechanisms of the Aluminium-iron Oxide Thermite Reaction," *Scripta Materialia*, vol. 41, pp. 541-548, 1999.
- [48] L. Zhou, N. Piekielek, S. Chowdhury, and M. R. Zachariah, "Time-resolved Mass Spectrometry of the Exothermic Reaction between Nanoaluminum and Metal Oxides: The Role of Oxygen Release," *Journal of Physical Chemistry C*, vol. 114, pp. 14269-14275, 2010.
- [49] E. L. Dreizin, M. Schoenitz, A. Ermoline, R. Clawson, M. Harrigan, "Solid Propellant Burn Rate Modifiers Based on Reactive Nanocomposite Materials Prepared by Arrested Reactive Milling," in *36th Propellant and Explosives Development and Characterization*, Orlando FL, 2010.
- [50] C. Badiola, M. Schoenitz, X. Zhu, and E. L. Dreizin, "Aluminum Rich Al-CuO Nanocomposite Materials Prepared by Arrested Reactive Milling at Cryogenic and Room Temperatures," in *47th AIAA Aerospace Sciences Meeting*, Orlando, FL, 2009.

- [51] S. M. Umbrajkar, M. Schoenitz, and E. L. Dreizin, "Fuel-rich Al-MoO₃ Nanocomposite Powders Prepared by Arrested Reactive Milling," in *45th AIAA Aerospace Sciences Meeting and Exhibit*, Reno, NV, 2007.
- [52] S. Umbrajkar, M. A. Trunov, M. Schoenitz, E. L. Dreizin, and R. Broad, "Arrested Reactive Milling Synthesis and Characterization of Sodium-nitrate Based Reactive Composites," *Propellants, Explosives, Pyrotechnics*, vol. 32, pp. 32-41, 2007.
- [53] T. S. Ward, W. Chen, M. Schoenitz, E. L. Dreizin, and R. Dave, "Nano-composite Energetic Powders Prepared by Arrested Reactive Milling," in *43rd AIAA Aerospace Sciences Meeting and Exhibit*, Reno, NV, 2005.
- [54] T. Mohan S., M.A., Dreizin, E.L., "Characterization of Aluminum Powder Ignition," in *the 2003 Technical Meeting of the Eastern States Section of the Combustion Institute*, University Park, PA, pp. 329-332, 2003.
- [55] Y. L. Shoshin, M. A. Trunov, X. Zhu, M. Schoenitz, and E. L. Dreizin, "Ignition of Aluminum-rich Al-Ti Mechanical Alloys in Air," *Combustion and Flame*, vol. 144, pp. 688-697, 2006.
- [56] D. Stamatis, Z. Jiang, V. K. Hoffmann, M. Schoenitz, and E. L. Dreizin, "Fully Dense, Aluminum-rich Al-CuO Nanocomposite Powders for Energetic Formulations," *Combustion Science and Technology*, vol. 181, pp. 97-116, 2009.
- [57] F. Yang, Y. Choi, P. Liu, J. Hrbek, and J. A. Rodriguez, "Autocatalytic Reduction of a Cu₂O/Cu(111) Surface by CO: STM, XPS, and DFT Studies," *Journal of Physical Chemistry C*, vol. 114, pp. 17042-17050, 2010.
- [58] E. M. Levin and R. S. Roth, "Polymorphism of Bismuth Sesquioxide. 1. Pure Bi₂O₃," *Journal of Research of the National Bureau of Standards-A. Physics and Chemistry*, vol. 68A, pp. 189-195, 1964.
- [59] L. A. Klinkova, V. I. Nikolaichik, N. V. Barkovskii, and V. K. Fedotov, "Thermal Stability of Bi₂O₃," *Russian Journal of Inorganic Chemistry*, vol. 52, pp. 1822-1829, 2007.
- [60] P. F. Carcia and E. M. McCarron Iii, "Synthesis and Properties of Thin Film Polymorphs of Molybdenum Trioxide," *Thin Solid Films*, vol. 155, pp. 53-63, 1987.

- [61] T. S. Ward, M. A. Trunov, M. Schoenitz, and E. L. Dreizin, "Experimental Methodology and Heat Transfer Model for Identification of Ignition Kinetics of Powdered Fuels," *International Journal of Heat and Mass Transfer*, vol. 49, pp. 4943-4954, 2006.
- [62] S. Chowdhury, K. Sullivan, N. Piekiet, L. Zhou, and M. R. Zachariah, "Diffusive vs Explosive Reaction at the Nanoscale," *Journal of Physical Chemistry C*, vol. 114, pp. 9191-9195, 2010.
- [63] B. Dikici, M. L. Pantoya, and V. Levitas, "The Effect of Pre-heating on Flame Propagation in Nanocomposite Thermites," *Combustion and Flame*, vol. 157, pp. 1581-1585, 2010.
- [64] D. Stamatis, E. L. Dreizin, and K. Higa, "Thermal Initiation of Al-MoO₃ Nanocomposite Materials Prepared by Different Methods," *Journal of Propulsion and Power*, vol. 27, pp. 1079-1087, 2011.
- [65] D. Stamatis and E. L. Dreizin, "Thermal Initiation of Consolidated Nanocomposite Thermites," *Combustion and Flame*, vol. 158, pp. 1631-1637, 2011.
- [66] K. Sullivan and M. R. Zachariah, "Simultaneous Pressure and Optical Measurements of Nanoaluminum Thermites: Investigating the Reaction Mechanism," *Journal of Propulsion and Power*, vol. 26, pp. 467-472, 2010.
- [67] K. T. Sullivan, W. A. Chiou, R. Fiore, and M. R. Zachariah, "In Situ Microscopy of Rapidly Heated Nano-Al and Nano-Al/WO₃ Thermites," *Applied Physics Letters*, vol. 97, 2010.
- [68] D. Stamatis, X. Jiang, E. Beloni, and E. L. Dreizin, "Aluminum Burn Rate Modifiers Based on Reactive Nanocomposite Powders," *Propellants, Explosives, Pyrotechnics*, vol. 35, pp. 260-267, 2010.
- [69] M. Schoenitz, B. Patel, O. Agboh, and E. L. Dreizin, "Oxidation of Aluminum Powders at High Heating Rates," *Thermochimica Acta*, vol. 507-508, pp. 115-122, 2010.
- [70] M. J. Starink, "The Determination of Activation Energy From Linear Heating Rate Experiments: A Comparison of the Accuracy of Isoconversion Methods," *Thermochimica Acta*, vol. 404, pp. 163-176, 2003.

- [71] M. W. Chase and National Institute of Standards and Technology (U.S.), *NIST-JANAF Thermochemical Tables*. [Washington, D.C.]; Woodbury, N.Y.: American Chemical Society; American Institute of Physics for the National Institute of Standards and Technology, 1998.
- [72] B. J. Henz, T. Hawa, and M. R. Zachariah, "On the Role of Built-in Electric Fields on the Ignition of Oxide Coated Nanoaluminum: Ion Mobility Versus Fickian Diffusion," *Journal of Applied Physics*, vol. 107, 2010.
- [73] V.E. Sanders, B. W. Asay, T.J. Foley, B.C. Tappan, A.N. Pacheco and S.F. Son, "Reaction Propagation of Four Nanoscale Energetic Composites," *Journal of Propulsion and Power*, vol. 23, pp. 707-714, 2007.
- [74] J. J. Birtill and P. G. Dickens, "Phase Relationships in the System H_xMoO_3 ($0 < x \leq 2.0$)," *Materials Research Bulletin*, vol. 13, pp. 311-316, 1978.
- [75] S. Takai, N. Hoshimi, and T. Esaka, "Synthesis of Tungsten, Molybdenum and Vanadium Bronzes by Mechanochemical Method Milling with Liquid Hydrocarbon," *Electrochemistry*, vol. 72, pp. 876-879, 2004.
- [76] W. G. Mallard and P. J. Linstrom, eds., *NIST Chemistry Web Book, NIST Standard Reference Database Number 69*, National Institute of Standards and Technology, Gaithersburg MD (1998) (<http://webbook.nist.gov>).
- [77] R. Feistel and W. Wagner, "A New Equation of State for H_2O Ice Ih," *Journal of Physical and Chemical Reference Data*, vol. 35, pp. 1021-1047, 2006.
- [78] C. Zhang, M. C. Gao, Y. Yang, and F. Zhang, "Thermodynamic Modeling and First-principles Calculations of the Mo–O System," *Calphad*, vol. 45, pp. 178-187, 2014.
- [79] R. Liu, W. Shi, Y. Cheng, and C. Huang, "Crystal Structures and Peculiar Magnetic Properties of α - and γ - Al_2O_3 Powders," *Modern Physics Letters B*, vol. 11, pp. 1169-1174, 1997.
- [80] M. Glor, "Hazards Due to Electrostatic Charging of Powders," *Journal of Electrostatics*, vol. 16, pp. 175-191, 1985.
- [81] M. Glor, "Electrostatic Ignition Hazards in the Process Industry," *Journal of Electrostatics*, vol. 63, pp. 447-453, 2005.

- [82] M. Glor, "Ignition Hazard Due to Static Electricity in Particulate Processes," *Powder Technology*, vol. 135–136, pp. 223-233, 2003.
- [83] C. D. Walther, Schacke, H. , "Danger of Electrostatic Ignition in the Handling of Solvent Containing Bulk Materials +IBM- Explosion in a Facility that Manufactures Coating Materials," *VDI Berichte*, vol. 2024, pp. 79–96, 2008.
- [84] U. von Pidoll, "An Overview of Standards Concerning Unwanted Electrostatic Discharges," *Journal of Electrostatics*, vol. 67, pp. 445-452, 2009.
- [85] J. Smallwood, "Standardisation of Electrostatic Test Methods and Electrostatic Discharge Prevention Measures for the World Market," *Journal of Electrostatics*, vol. 63, pp. 501-508, 2005.
- [86] C. J. Dahn and A. G. Dastidar, "Requirements for a Minimum Ignition Energy Standard," *Process Safety Progress*, vol. 22, pp. 43-47, 2003.
- [87] L. Perrin, A. Laurent, V. Falk, O. Dufaud, and M. Traore, "Dust and Electrostatic Hazards, Could we Improve the Current Standards?," *Journal of Loss Prevention in the Process Industries*, vol. 20, pp. 207-217, 2007.
- [88] S. Zeman, Kočí, J., "Electric Spark Sensitivity of Polynitro Compounds. Part IV. A Relation to Thermal Decomposition Parameters," *Hanneng Cailiao*, vol. 8, pp. 18–21, 2000.
- [89] D. Skinner, D. Olson, and A. Block-Bolten, "Electrostatic Discharge Ignition of Energetic Materials," *Propellants, Explosives, Pyrotechnics*, vol. 23, pp. 34-42, 1998.
- [90] MIL-STD-1751A, "Manual of Data Requirements and Tests for the Qualification of Explosive Materials for Military Use," *AOP-7*, 2003.
- [91] R. A. Williams, E. L. Dreizin, and E. Beloni, "Ignition of Metal Powder Layers of Different Thickness by Electrostatic Discharge," *Journal of Propulsion and Power*, vol. 28, pp. 132-139, 2012.
- [92] E. Beloni, P. R. Santhanam, and E. L. Dreizin, "Electrical Conductivity of a Metal Powder Struck by a Spark," *Journal of Electrostatics*, vol. 70, pp. 157-165, 2012.
- [93] E. Beloni and E. L. Dreizin, "Experimental Study of Ignition of Magnesium Powder by Electrostatic Discharge," *Combustion and Flame*, vol. 156, pp. 1386-1395, 2009.

- [94] E. Beloni and E. L. Dreizin, "Ignition of Aluminum Powders by Electro-static Discharge," *Combustion and Flame*, vol. 157, pp. 1346-1355, 2010.
- [95] E. Beloni and E. L. Dreizin, "Ignition of Titanium Powder Layers by Electrostatic Discharge," *Combustion Science and Technology*, vol. 183, pp. 823-845, 2011.
- [96] E. Beloni and E. L. Dreizin, "Model of Heating and Ignition of Conductive Polydisperse Powder in Electrostatic Discharge," *Combustion Theory and Modelling*, vol. 16, pp. 976-993, 2012.
- [97] R. A. Williams, Schoenitz, M., Ermoline, A., Dreizin, E.L., , "Multistep Reaction Model for Ignition of Nanocomposite Thermites with Different Compositions," *Thermochimica Acta*, Article Submitted.
- [98] J. A. Puszynski, C. J. Bulian, and J. J. Swiatkiewicz, "Ignition Characteristics of Nanothermite Systems," *International Journal of Energetic Materials and Chemical Propulsion* , vol. 7, pp. 73-86, 2008.
- [99] T. Foley, A. Pacheco, J. Malchi, R. Yetter, and K. Higa, "Development of Nanothermite Composites with Variable Electrostatic Discharge Ignition Thresholds," *Propellants, Explosives, Pyrotechnics*, vol. 32, pp. 431-434, 2007.
- [100] C. Weir, M. L. Pantoya, G. Ramachandran, T. Dallas, D. Prentice, and M. Daniels, "Electrostatic Discharge Sensitivity and Electrical Conductivity of Composite Energetic Materials," *Journal of Electrostatics*, vol. 71, pp. 77-83, 2013.
- [101] M. Steinkrauss, et al., "Fire and Explosion Properties of Synthetic Nanomaterials. Initial Investigations for Major Accident Prevention.," *Environmental studies no. 1011*, pp. Federal Office for the Environment, Bern. 39, 2010.
- [102] C. Farley and M. Pantoya, "Reaction Kinetics of Nanometric Aluminum and Iodine Pentoxide," *Journal of Thermal Analysis and Calorimetry*, vol. 102, pp. 609-613, 2010.
- [103] B. R. Clark and M. L. Pantoya, "The Aluminium and Iodine Pentoxide Reaction for the Destruction of Spore Forming Bacteria," *Physical Chemistry Chemical Physics*, vol. 12, pp. 12653-12657, 2010.
- [104] Y. Wang, C. Yang, X. L. Song, W. Jiang, G. D. Deng, and F. S. Li, "Reactive Materials Synthesis and Aluminothermy Reaction of Aluminum/Cobalt-lead Oxide," *Applied Mechanics and Materials*, vol. 320, ed, pp. 383-388, 2013.

- [105] Y. Yang, D. Xu, and K. Zhang, "Effect of Nanostructures on the Exothermic Reaction and Ignition of Al/CuO_x Based Energetic Materials," *Journal of Materials Science*, vol. 47, pp. 1296-1305, 2012.
- [106] Y. Wang, X. Song, W. Jiang, G. Deng, X. Guo, H. Liu, *et al.*, "Synthesis of Nano-nickel-coated Micro-aluminum and Thermal Reactivity of Aluminum/nickels Tannic-oxide Thermite," *International Journal of Energetic Materials and Chemical Propulsion*, vol. 10, pp. 231-243, 2011.
- [107] J. Wang, A. Hu, J. Persic, J. Z. Wen, and Y. Norman Zhou, "Thermal Stability and Reaction Properties of Passivated Al/CuO Nano-thermite," *Journal of Physics and Chemistry of Solids*, vol. 72, pp. 620-625, 2011.
- [108] M. Petrantoni, C. Rossi, L. Salvagnac, V. Conédéra, A. Estève, C. Tenailleau, *et al.*, "Multilayered Al/CuO Thermite Formation by Reactive Magnetron Sputtering: Nano Versus Micro," *Journal of Applied Physics*, vol. 108, 2010.
- [109] K. T. Sullivan, C. Wu, N. W. Piekielek, K. Gaskell, and M. R. Zachariah, "Synthesis and Reactivity of Nano-Ag₂O as an Oxidizer for Energetic Systems Yielding Antimicrobial Products," *Combustion and Flame*, vol. 160, pp. 438-446, 2013.
- [110] G. Jian, N. W. Piekielek, and M. R. Zachariah, "Time-resolved Mass Spectrometry of Nano-Al and Nano-Al/CuO Thermite Under Rapid Heating: A Mechanistic Study," *Journal of Physical Chemistry C*, vol. 116, pp. 26881-26887, 2012.
- [111] N. W. Piekielek, R. E. Cavicchi, and M. R. Zachariah, "Rapid-heating of Energetic Materials Using a Micro-differential Scanning Calorimeter," *Thermochimica Acta*, vol. 521, pp. 125-129, 2011.
- [112] P. Swaminathan, M. D. Grapes, K. Woll, S. C. Barron, D. A. Lavan, and T. P. Weihs, "Studying exothermic reactions in the Ni-Al system at rapid heating rates using a nanocalorimeter," *Journal of Applied Physics*, vol. 113, 2013.
- [113] M. Vohra, M. Grapes, P. Swaminathan, T. P. Weihs, and O. M. Knio, "Modeling and Quantitative Nanocalorimetric Analysis to Assess Interdiffusion in a NiAl bilayer," *Journal of Applied Physics*, vol. 110, 2011.
- [114] K. T. Sullivan, N. W. Piekielek, S. Chowdhury, C. Wu, M. R. Zachariah, and C. E. Johnson, "Ignition and Combustion Characteristics of Nanoscale Al/AgIO₃: A Potential Energetic Biocidal System," *Combustion Science and Technology*, vol. 183, pp. 285-302, 2011.

- [115] G. Jian, S. Chowdhury, K. Sullivan, and M. R. Zachariah, "Nanothermite Reactions: Is Gas Phase Oxygen Generation from the Oxygen Carrier an Essential Prerequisite to Ignition?," *Combustion and Flame*, vol. 160, pp. 432-437, 2013.
- [116] L. Zhou, N. Piekiet, S. Chowdhury, D. Lee, and M. R. Zachariah, "Transient Ion Ejection During Nanocomposite Thermite Reactions," *Journal of Applied Physics*, vol. 106, 2009.
- [117] E. L. Dreizin, C. Badiola, S. Zhang, and Y. Aly, "Particle Combustion Dynamics of Metal-based Reactive Materials " *International Journal of Energetic Materials and Chemical Propulsion*, vol. 10, pp. 297-319, 2011.
- [118] K. E. Brown, W. L. Shaw, X. X. Zheng, and D. D. Dlott, "Simplified Laser-driven Flyer Plates for Shock Compression Science," *Review of Scientific Instruments*, vol. 83, 2012.
- [119] M. D. Bowden and M. P. Maisey, "The Development of a Heterodyne Velocimeter System for Use in Sub-microsecond Time Regimes," *Optical Technologies for Arming, Safing, Fuzing, and Firing Iii*, vol. 6662, 2007.
- [120] J. D. Weng, X. Wang, Y. Ma, H. Tan, L. C. Cai, J. F. Li, *et al.*, "A Compact All-fiber Displacement Interferometer for Measuring the Foil Velocity Driven by Laser," *Review of Scientific Instruments*, vol. 79, 2008.
- [121] J. W. Forbes, *Shock Wave Compression of Condensed Matter: a Primer*. New York, NY: Springer, 2012.
- [122] S. P. Marsh, *LASL Shock Hugoniot Data*. Berkeley, CA: University of California Press, 1980.
- [123] X. X. Zheng, A. D. Curtis, W. L. Shaw, and D. D. Dlott, "Shock Initiation of Nano-Al Plus Teflon: Time-Resolved Emission Studies," *Journal of Physical Chemistry C*, vol. 117, pp. 4866-4875, 2013.
- [124] R. A. Williams, J. V. Patel, and E. L. Dreizin, "Ignition of Fully Dense Nanocomposite Thermite Powders by an Electric Spark," *Journal of Propulsion and Power*, vol. 30, pp. 765-777, 2014.
- [125] W. L. Shaw, R. A. Williams, E. L. Dreizin, and D. D. Dlott, "Using Laser-driven Flyer Plates to Study the Shock Initiation of Nanoenergetic materials," in *18th Biennial Intl. Conference of the APS Topical Group on Shock Compression of Condensed Matter*, Seattle, WA, 2013.

- [126] J. W. Spears, H. Krompholz, and L. L. Hatfield, "Sub-nanosecond Point-plane Gas Breakdown in a Conical-shaped Spark Gap," in *Pulsed Power Conference*, Dallas, TX, 2003.
- [127] H. Yamashita, K. Yamazawa, and Y. S. Wang, "The Effect of Tip Curvature on the Prebreakdown Streamer Structure in Cyclohexane," *IEEE Transactions on Dielectrics and Electrical Insulation*, vol. 5, pp. 396-401, 1998.